

THESIS FOR THE DEGREE OF DOCTOR OF PHILOSOPHY IN THERMO AND  
FLUID DYNAMICS

# Dynamics of bubbles across scales

NIKLAS HIDMAN

Department of Mechanics and Maritime Sciences

Division of Fluid Dynamics

CHALMERS UNIVERSITY OF TECHNOLOGY

Göteborg, Sweden 2023

Dynamics of bubbles across scales

NIKLAS HIDMAN

ISBN 978-91-7905-774-9

© NIKLAS HIDMAN, 2023

Doktorsavhandlingar vid Chalmers tekniska högskola

Ny serie nr. 5240

ISSN 0346-718X

Department of Mechanics and Maritime Sciences

Division of Fluid Dynamics

Chalmers University of Technology

SE-412 96 Göteborg

Sweden

Telephone: +46 (0)31-772 1000

Cover:

Contours of the total scalar field in a turbulent bubbly flow with an imposed mean gradient in the vertical direction.

Chalmers digitaltryck

Göteborg, Sweden 2023

NIKLAS HIDMAN

Department of Mechanics and Maritime Sciences

Division of Fluid Dynamics

Chalmers University of Technology

## ABSTRACT

This thesis presents numerical investigations of bubbly flow phenomena across a wide range of relevant spatial and temporal scales. The aim is to increase our understanding of a great variety of underlying phenomena and to facilitate improved predictions of bubbly flows at all relevant scales. The investigations start at small spatial scales (size of individual bubbles and below). We focus on the evolution of vapour bubbles by formulating a multiphase Direct Numerical Simulation (DNS) framework and a computationally inexpensive 1D framework, which both consider phase change- and thermal effects. These frameworks are used to study laser-induced thermocavitation bubbles that are a part of a promising technology to achieve good control of the properties of the formed crystals in the crystallisation process. Our findings identify plausible mechanisms that induce crystallisation and give guidelines for selecting suitable system parameters to maintain and control the crystallisation process. We continue to larger scales by focusing on the dynamics of individual rising bubbles. An efficient multiscale methodology is developed in an Eulerian-Lagrangian framework that predicts the liquid-phase fluctuations experienced by a bubble rising in a turbulent flow field. The dynamics and deformation of the bubble due to the liquid-phase fluctuations are resolved using a multiphase DNS framework together with a formulated Moving Reference Frame (MRF) technique. This multiscale approach is useful for studying numerous small-scale processes where bubbles are smaller than the Kolmogorov scales and can be used for bubbles, droplets or particles in both laminar and turbulent flows. We use the developed DNS framework with the MRF to study the lift force acting on deformable bubbles in steady shear flows. We formulate a theoretical framework and support it with DNS to provide a comprehensive explanation for the several identified mechanisms behind the lift force. The findings also elucidate the influence of the shear rate and governing parameters on the lift force. Finally, we study, using DNS, the dynamics and mixing properties of bubbly flows at large spatial scales (size of the entire system). We extract and analyse the dynamics and statistics of passive scalars involving  $O(10 - 100)$  bubbles in periodic domains. The results show a significant influence of the bubble-induced turbulence on the scalar spectra and elucidate the influence of the governing parameters on the scalar dynamics and mixing properties.

Keywords: Bubbly flows, DNS, multiphase, multiscale, lift force, scalar mixing



*To my family*



## ACKNOWLEDGEMENTS

I would like to begin by thanking my supervisor Gaetano Sardina and my examiner and co-supervisor Srdjan Sasic for granting me the possibility to pursue my PhD in this complex and fascinating subject. Without their excellent supervision and support this thesis would not be possible. I would also like to thank my co-supervisors Henrik Ström and Dario Maggiolo for their valuable input and assistance throughout the different turns in the project. I have learnt so much from you all and hope we can continue to collaborate in the future.

I would also like to thank my wonderful co-workers at the division. You make the time we spend here enjoyable. A special thank to all the members of the multi-phase group, Adam, Ananda, Kosta, Patricia, Johannes, Sudharsan, Magnus and many more that always ensure interesting and entertaining lunches and are always there for discussions and support when simulations crash or mistakes are made.

Finally, I would like to give my gratitude to Malin, Sixten and the rest of my family for your invaluable support and for patiently enduring me through this project.

The thesis work was funded by the Swedish Research Council (Vetenskapsrådet), grant VR 2017-05031. The computations were enabled by resources provided by the Swedish National Infrastructure for Computing (SNIC) at C3SE partially funded by the Swedish Research Council through grant agreement no. 2018-05973. We gratefully acknowledge the HPC RIVR consortium ([www.hpc-rivr.si](http://www.hpc-rivr.si)) and EuroHPC JU ([eurohpc-ju.europa.eu](http://eurohpc-ju.europa.eu)) for providing computing resources of the HPC system Vega at the Institute of Information Science ([www.izum.si](http://www.izum.si)).



# NOMENCLATURE

## Abbreviations

DNS	Direct Numerical Simulations
EE	Eulerian-Eulerian
EL	Eulerian-Lagrangian
MRF	Moving Reference Frame
PDF	Probability Density Function
PID	Proportional-Integral-Derivative
PLIC	Piecewise Linear Interface Construction
VOF	Volume Of Fluid

## Dimensionless numbers

$Eu = \frac{\rho_l g D^2}{\sigma}$	Eötvös number. Ratio of buoyancy and surface tension.	—
$Ga = \frac{\rho_l \sqrt{g D} D}{\mu_l}$	Galilei number. Ratio of buoyancy and viscosity.	—
$Sc = \nu / D_{mol}$	Schmidt number. Ratio of momentum diffusivity (kinematic viscosity) and mass diffusivity.	—
$Sr = \frac{\omega D}{\sqrt{g D}}$	Dimensionless shear rate.	—

## Greek Letters

$\beta$	Maximum density reduction ratio	—
$\chi$	Accommodation coefficient / Bubble aspect ratio	—
$\Delta r$	Computational grid spacing radial direction	m
$\Delta t$	Computational time step	s
$\Delta x$	Computational cell size	m
$\delta_S$	Dirac distribution function	—
$\epsilon$	Cell cost function	—
$\varepsilon$	Energy dissipation rate	$\text{m}^2 \text{s}^{-3}$
$\kappa$	Interface curvature	$\text{m}^{-1}$
$\lambda$	Thermal conductivity	$\text{W m}^{-1} \text{K}^{-1}$
$\mu$	Dynamic viscosity	$\text{kg m}^{-1} \text{s}^{-1}$
$\nu$	Kinematic viscosity	$\text{m}^2 \text{s}^{-1}$

$\Omega$	Computational domain	$\text{m}^3$
$\boldsymbol{\omega}$	Vorticity field	$\text{s}^{-1}$
$\omega$	Shear rate	$\text{s}^{-1}$
$\phi$	Bubble orientation angle / gas volume fraction	$^\circ/-$
$\psi$	Weighting factor	$-$
$\rho$	Density	$\text{kg m}^{-3}$
$\sigma$	Surface tension	$\text{N m}^{-1}$
$\tau$	Time scale	$\text{s}$
$\theta$	Angular coordinate	$\text{rad}$
$\xi$	Average angular quantity	$\text{rad}$
$\zeta$	Average angular quantity	$\text{rad}$
<b>Roman Letters</b>		
$\boldsymbol{a}$	Acceleration vector	$\text{m s}^{-2}$
$A_B$	Bubble interface area	$\text{m}^2$
$b$	Arbitrary positive value	$-$
$Co$	Courant number	$-$
$c$	Scalar field	$-$
$c_p$	Specific heat capacity	$\text{J kg}^{-1} \text{K}^{-1}$
$C_{AM}$	Added mass coefficient	$-$
$C_D$	Drag force coefficient	$-$
$C_L$	Lift force coefficient	$-$
$\boldsymbol{D}$	Force vector	$\text{N}$
$D$	Spherical equivalent bubble diameter	$\text{m}$
$D_{mol}$	Molecular diffusivity	$\text{m}^2 \text{s}^{-1}$
$d_b$	Spherical equivalent bubble diameter	$\text{m}$
$\boldsymbol{e}$	Deviation of initial position vector	$\text{m}$
$E$	Spectrum	$-$
$\boldsymbol{F_L}$	Lift force vector	$\text{N}$
$f$	Volume fraction field	$-$
$g$	Gravitational acceleration	$\text{m s}^{-2}$
$j$	Phase change mass flux	$\text{kg m}^{-2} \text{s}^{-1}$
$k$	Wavenumber	$\text{m}^{-1}$
$\mathcal{L}$	Latent heat	$\text{J kg}^{-1}$
$L$	Computational domain length	$\text{m}$

$\mathbf{n}$	Normal vector	—
$\mathcal{P}$	Bubble proximity field	—
$p$	Pressure	Pa
$q$	Bubble integer tag number	—
$\mathbf{r}$	Position vector	m
$R$	Bubble Radius	m
$r$	Radial coordinate	m
$S^q$	Sphere around bubble q	m <sup>3</sup>
$S_\sigma$	Supersaturation level	—
$S_C$	Mass source term	kg m <sup>-3</sup> s <sup>-1</sup>
$S_h$	Energy source term	J m <sup>-3</sup> s <sup>-1</sup>
$\mathcal{T}$	Bubble tag field	—
$T$	Temperature	K
$t$	Time	s
$\mathbf{U}$	Undisturbed fluid velocity vector	m s <sup>-1</sup>
$\mathbf{u}$	Fluid velocity vector	m s <sup>-1</sup>
$u$	Fluid velocity	m s <sup>-1</sup>
$\mathbf{V}$	Bubble velocity vector	m s <sup>-1</sup>
$\mathbf{x}$	Spatial coordinate vector	m

### Superscripts and Subscripts

'	Fluctuation
^	Coordinate system in a moving reference frame
~	Disturbance field
$\eta$	Kolmogorov scale
$\infty$	Surrounding
$BC$	Boundary Condition
$mrf$	Moving reference frame
$rel$	Relative
$rep$	Repulsive
$sat$	Saturation conditions
$std$	Standard deviation
$B$	Bubble
$l$	Liquid
$r$	Ratio
$s$	Suspension
$v$	Vapour



## LIST OF PUBLICATIONS

This thesis consists of an extended summary and the following appended papers:

- Paper A** N. Hidman, G. Sardina, D. Maggiolo, H. Ström, and S. Sasic. Laser-induced vapour bubble as a means for crystal nucleation in supersaturated solutions - Formulation of a numerical framework. *Experimental and Computational Multiphase Flow* **1.4** (2019), 242–254. DOI: 10.1007/s42757-019-0024-z.
- Paper B** N. Hidman, G. Sardina, D. Maggiolo, H. Ström, and S. Sasic. Numerical Frameworks for Laser-Induced Cavitation: Is Interface Supersaturation a Plausible Primary Nucleation Mechanism? *Crystal Growth & Design* **20.11** (2020), 7276–7290. DOI: 10.1021/acs.cgd.0c00942.
- Paper C** N. Hidman, H. Ström, S. Sasic, and G. Sardina. A multiscale methodology for small-scale bubble dynamics in turbulence. *International Journal of Multiphase Flow* **150** (2022), 103976. DOI: 10.1016/j.ijmultiphaseflow.2022.103976.
- Paper D** N. Hidman, H. Ström, S. Sasic, and G. Sardina. The lift force on deformable and freely moving bubbles in linear shear flows. *Journal of Fluid Mechanics* **952** (2022), A34. DOI: 10.1017/jfm.2022.917.
- Paper E** N. Hidman, H. Ström, S. Sasic, and G. Sardina. “Assessing passive scalar dynamics in bubble-induced turbulence using DNS”. Submitted to a scientific journal.



## ADDITIONAL RELEVANT PUBLICATIONS

### Paper 1

N. Hidman, G. Sardina, D. Maggiolo, H. Ström, and S. Sasic. “Numerical simulation of a laser-induced vapour bubble for crystal nucleation at low supersaturation levels”. *Proceedings of the 10th International Conference on Multiphase Flow*, (ICMF19). Rio de Janeiro, Brazil, 2019.

### Paper 2

N. Hidman, H. Ström, S. Sasic, and G. Sardina. “Resolving sub-kolmogorov bubble dynamics in turbulent flows: Formulation of a multi-scale numerical framework”. *Proceedings of the 18th International Conference on Fluid Flow Technologies*. Conference on Modelling Fluid Flow (CMFF22). Budapest, Hungary, 2022, pp. 318–325.

### Paper 3

N. Hidman, H. Ström, S. Sasic, and G. Sardina. “The shear-induced lift force on freely moving and deformable bubbles”. *Proceedings of the 11th International Conference on Multiphase Flow*, (ICMF23). Kobe, Japan, 2023.

### Paper 4

N. Hidman, H. Ström, S. Sasic, and G. Sardina. “The passive scalar spectrum of bubble-induced turbulence”. *Proceedings of the 11th International Conference on Multiphase Flow*, (ICMF23). Kobe, Japan, 2023.



# Contents

<b>Abstract</b>	<b>i</b>
<b>Acknowledgements</b>	<b>v</b>
<b>Nomenclature</b>	<b>vii</b>
<b>List of publications</b>	<b>xi</b>
<b>Additional relevant publications</b>	<b>xiii</b>
 <b>I Extended Summary</b>	 <b>1</b>
<b>1 Introduction</b>	<b>3</b>
<b>2 Background</b>	<b>7</b>
2.1 Scales in bubbly flows as considered in this thesis . . . . .	7
2.2 Formation and evolution of small-scale vapour bubbles . . . . .	7
2.3 Dynamics of small-scale rising bubbles . . . . .	10
2.4 Dynamics of intermediate and large-scale bubbly flows . . . . .	12
2.5 Multi-scale modelling strategies . . . . .	13
2.6 Objectives of the research work . . . . .	14
<b>3 Numerical frameworks for bubble dynamics from small to large scales</b>	<b>19</b>
3.1 Numerical frameworks for the evolution of small-scale vapour bubbles . .	19
3.1.1 Multiphase DNS framework for vapour bubble evolution . . . . .	20
3.1.2 1D Numerical framework for vapour bubble evolution . . . . .	22
3.2 Numerical frameworks for small-scale rising bubbles . . . . .	27
3.2.1 Multiphase DNS with non-inertial moving reference frame . . . . .	28
3.2.2 Coupled Eulerian-Lagrangian and multiphase DNS frameworks for small-scale bubble dynamics in turbulence . . . . .	30
3.3 Numerical frameworks for large-scale scalar dynamics in bubbly flows . .	33
3.3.1 Multiphase DNS framework for passive scalar transport in bubbly flows . . . . .	34
<b>4 Selected results and discussion</b>	<b>39</b>

4.1	Numerical investigations of laser-induced thermocavitation . . . . .	39
4.2	Small-scale rising bubble dynamics . . . . .	43
4.2.1	Dynamics of individual bubbles in turbulent flows . . . . .	44
4.2.2	Shear-induced lift force acting on deformable bubbles . . . . .	49
4.3	Passive scalar transport in large-scale bubbly flows . . . . .	54
<b>5</b>	<b>Conclusions and recommendations for future work</b>	<b>59</b>
5.1	Evolution of small-scale vapour bubbles . . . . .	59
5.2	Small-scale rising bubble dynamics . . . . .	60
5.2.1	Shear-induced lift force acting on individual bubbles . . . . .	61
5.3	Large-scale scalar dynamics in bubbly flows . . . . .	62
<b>6</b>	<b>Summaries of appended papers and division of work</b>	<b>63</b>
	<b>References</b>	<b>64</b>
<b>II</b>	<b>Appended Papers A–E</b>	<b>71</b>

Part I

# Extended Summary



# 1 Introduction

Bubbly flow is a multiphase fluid flow regime characterised by a dispersed gaseous phase in a liquid phase continuum. The gaseous phase is distributed as individual bubbles within the heavier liquid phase, and due to gravity, a buoyant force acts on the bubbles in the opposite gravitational direction. Bubbly flows are important in a wide range of industrial and natural processes, among others in pipe flows, bubble columns, froth flotation tanks, nuclear reactors, heat exchangers, bubble drag reduction on marine vessels, oil and gas transport, atmosphere-ocean exchanges and cavitation [1]. To understand and design such systems, it is essential to be able to accurately predict the bubbly flow dynamics. However, there are numerous phenomena that are not yet fully understood and, hence, we are still not in a position to have fully reliable models that cover a comprehensive range of features and behaviours encountered in bubbly flows [2]. One of the main challenges in developing such models is the large range of spatial and temporal scales [3]. Bubbles may form at the scale of nanometers and, through complex interactions with other bubbles and the liquid phase, induce two-phase flow structures in the order of tens of meters [4].

This thesis studies numerically the bubble dynamics in a wide range of spatiotemporal scales with the aim of increasing our physical understanding about bubbly flow phenomena and to improve bubbly flow predictions. In this thesis, we define and work with three length scales relevant to bubbly flow phenomena: small, intermediate and large scales. The small length scales refer to scales of individual bubbles or below. The intermediate scales are the length scales of bubble swarms where the bubbles exhibit a collective behaviour, and the large scales refer to flow features at the scales of the entire bubbly flow system. These scales are all above the molecular length scales that are not considered in this work. Nonetheless, molecular processes such as the nucleation of vapour bubbles are important and are briefly discussed in Section 2.2.

To appreciate the multi-scale nature of bubbly flows, consider a case of saturated nucleate boiling, as illustrated in Figure 1.1. At the molecular scales, the vapour bubbles are nucleated at the heating surface due to superheating of the adjacent liquid. The vapour bubbles grow across the small length scales by evaporation of the superheated liquid at the bubble interface. After reaching a critical size, the bubbles detach from the surface and rise due to buoyancy. At the small scales, the bubbles may coalesce with other bubbles, or, breakup into smaller ones. These processes occur continuously within the system and result in a poly-disperse bubbly flow with a large variation of bubble dynamics. The rising bubbles induce small-scale liquid velocity fluctuations that, at certain conditions, generate bubble-induced (or pseudo-) turbulence [5]. In addition, small-scale viscous boundary layers are formed at the rising bubble interface and in the case of chemical reactions or phase change, also thermal, and mass transfer boundary layers are induced in the adjacent liquid. At intermediate scales, the hydrodynamic interaction of rising bubbles can lead to the formation of bubble swarms with a seemingly collective behaviour. At the largest scales, the rising bubble swarms can produce system-size re-circulation zones and even turbulent large-scale flows. Such dynamics at the large scales influence

the processes at smaller scales resulting in a system that is coupled across the scales.

Because of this multiscale coupling, a fundamental understanding of the processes involved at one scale, and how these processes influence other scales, is essential to predict the complex dynamics of the entire system. This thesis comprises the appended Papers A-E that investigate the physical phenomena behind several specific bubbly flow processes (illustrated in Figure 1.1) and presents numerical frameworks for investigating bubbly flows across a wide range of relevant length scales. Our results increase our understanding of these processes and facilitate the development of improved sub-grid models that are used to predict the dynamics of complex bubbly flows up to industrial scales.

This thesis is composed of six themed chapters. We begin with a brief overview of relevant phenomena and numerical challenges characteristic of the different length scales in Section 2. To model this range of phenomena and length scales, we outline a commonly used multi-scale modelling approach for bubbly flows in Section 2.5. Based on this overview, we state in Section 2.6 the topics we have chosen to focus on in this thesis. We outline the developed numerical frameworks in Section 3 and expand on certain details not included in the appended papers. In Section 4 we show selected results from our numerical studies and discuss our findings. We summarise our main contributions and results in Section 5 where we also provide recommendations for future work. Summaries of the appended Papers A-E are presented in Section 6.

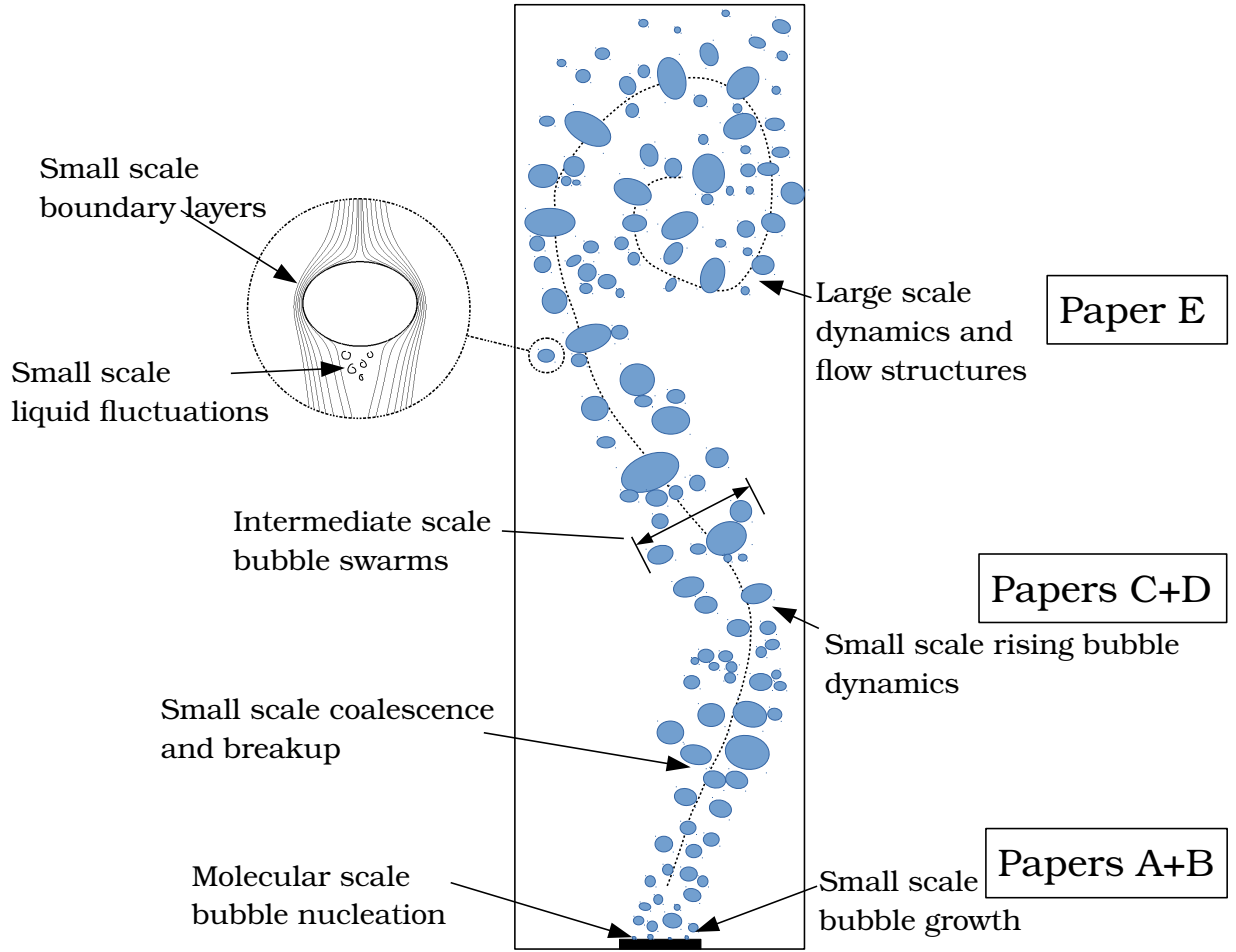


Figure 1.1: *Illustration of bubbly flow processes occurring at various length scales during saturated nucleate pool boiling. Vapour bubbles nucleate at  $O(10^{-9} \text{ m})$  and, through complex interactions with other bubbles and the liquid, form two-phase flow structures of the sizes of  $O(10 \text{ m})$ . Papers A-E indicate the types of scales and processes addressed in the respective papers.*



## 2 Background

In this section, we present a brief overview of important bubbly flow phenomena across the considered length scales. This overview is intended to provide a context to the specific processes we focus on in this thesis and to illustrate the relevance of the performed studies. We find it useful to first remind the reader of our definitions of the scales in bubbly flows that we work with in this thesis. Then, we discuss important phenomena at the range from small to large scales and identify numerical challenges and current limitations in understanding and modelling. Finally, we present an overview of a commonly used multi-scale modelling strategy for bubbly flows that exemplifies numerical challenges and highlights the importance of having trustworthy models at all scales. This strategy also illustrates how the results of this thesis can facilitate the formulation of improved models.

### 2.1 Scales in bubbly flows as considered in this thesis

In this thesis, we distinguish three different length scales that are all above molecular scales. The small scales are characteristic length scales of physical processes occurring at the scale of a single bubble or below. Intermediate scales refer to the characteristic length scales of several rising bubbles that interact and form bubble swarms with a seemingly collective behaviour. Finally, the large scales refer to length scales of phenomena that influence the dynamics of the entire bubbly flow system, such as inhomogeneous bubble distributions and re-circulation zones but also statistical properties of the bubbly flow such as turbulent characteristics, mixing and transport properties.

### 2.2 Formation and evolution of small-scale vapour bubbles

The smallest scales we consider in this thesis comprise the formation and evolution of a vapour bubble. This process can be divided into two phases, the nucleation of the bubble itself and the evolution of that bubble. We begin with an overview of the nucleation process and then focus on the small-scale bubble evolution process.

Vapour bubble nucleation is a stochastic, molecular process governed by the liquid's departure from saturation conditions and the surface tension between the phases. Because of the stochastic nature and the small scales of the problem, the nucleation process itself is not entirely understood [6]. We will not analyse this process in detail but instead give some general concepts and explain the terminology.

The nucleation process can be divided into two main types, homogeneous and heteroge-

neous. In the homogeneous case, the nucleation occurs within the pure liquid phase due to thermal motion. The stochastic thermal motion generates temporary voids that may grow to bubbles if the voids are sufficiently large. In the heterogeneous case, nucleation occurs at solid walls or particles in the liquid. The presence of foreign particles or walls significantly increases the probability of nucleation; therefore heterogeneous nucleation is the most common type in engineering applications [7].

Regardless of the type of nucleation, the vapour bubble formation process is commonly separated into two categories, cavitation and boiling. Cavitation is the nucleation process that occurs when the liquid pressure falls below the saturation pressure, and boiling is the nucleation process that occurs when the liquid temperature is raised above the saturation temperature.

The two bubble formation processes are similar, but the dynamics of the resulting vapour bubble may differ considerably. In cavitation, the liquid pressure around the bubble governs the bubble evolution process. The liquid pressure can change both rapidly and uniformly around the bubble due to local flow phenomena or changes of the system pressure. The rapid change of liquid pressure leads to fast growth and collapse dynamics in many practical cavitation events. Conversely, in boiling, it is the phase change and heat transport of the surrounding liquid that govern the bubble evolution process. Compared to the possible rapid change of the liquid pressure, the liquid temperature around the bubble usually varies much more slowly. Because of this difference, the bubble evolution dynamics are usually slower in boiling situations than in the cavitation cases.

Nonetheless, there are processes for which also the temperature is rapidly varying, and the difference between cavitation and boiling dynamics is less clear. One such process is termed laser-induced thermocavitation, where a short (often nano-second) laser pulse superheats a region of the liquid. Within this region, a vapour bubble is nucleated and starts to grow due to rapid evaporation of the superheated liquid at the bubble interface. The evaporation causes the pressure in the bubble to increase and, thus, the bubble to grow. When the superheated liquid is evaporated or cooled, the vapour starts to condense due to heat loss to the surrounding liquid, and the bubble begins to collapse. In a typical laser-induced thermocavitation event, the entire bubble lifetime is of the order of 10 – 100 microseconds, and the maximum bubble radius is of the order of 100 micrometers.

Small bubbles are usually spherical due to the surface tension that results in a net force per unit area in the radially inward direction. The net force increases inversely with the radius of the bubble as  $2\sigma/R$ , where  $\sigma$  is the surface tension and  $R$  is the bubble interface radius. Since the radius of the nucleated bubble is small, the surface tension force is relatively large compared to inertial or viscous forces. These force ratios result in a spherical bubble with a minimum of surface energy.

The pressure of the gas,  $p_B$ , inside a static spherical bubble, is at equilibrium conditions, and for pure vapour, this corresponds to the saturation pressure,  $p_{sat}(T_B)$ , where  $T_B$  is the vapour temperature. The pressure in the surrounding liquid,  $p_\infty$ , and the surface tension force compress the gas inside the bubble. At equilibrium conditions, the forces

acting at the bubble interface balance according to the Young-Laplace equation [8, 9]

$$p_B = p_\infty + 2\sigma/R. \quad (2.1)$$

However, at non-equilibrium conditions, the forces may not balance, and the bubble interface either grows or shrinks according to the generalised Rayleigh-Plesset equation [10–12]

$$\frac{p_B(t) - p_\infty(t)}{\rho_l} = R \frac{d^2 R}{dt^2} + \frac{3}{2} \left( \frac{dR}{dt} \right)^2 + \frac{4\nu_l}{R} \frac{dR}{dt} + \frac{2\sigma}{\rho_l R}. \quad (2.2)$$

Here,  $\rho_l$  and  $\nu_l$  are the liquid density and kinematic viscosity, respectively and the effects of phase change are not included. What differentiates the bubble growth processes in cavitation and boiling situations are the phenomena that govern the pressure difference on the left-hand side of Equation 2.2. In cavitation cases, the surrounding liquid pressure  $p_\infty(t)$  is reduced, whereas, in boiling situations, the liquid is evaporated into the bubble causing the bubble pressure  $p_B(t)$  to increase. Both phenomena result in bubble growth, but since the physical processes are different, the resulting bubble dynamics differ as well.

For most cavitation bubbles, the effects of phase change are relatively small, and the growth rate of the bubble is controlled by the inertial effects of the surrounding liquid, described by the two first terms on the right-hand side of Equation 2.2 [7]. With rapid changes in the surrounding liquid pressure, the cavitation bubble can display fast growth and collapse dynamics. When the liquid pressure falls, the bubble rapidly expands, and if the bubble moves into a high-pressure liquid region, the bubble may collapse implisively. During such collapse phases, the liquid inertia and the surface tension force can compress the bubble and produce maximum gas temperatures of over 15000  $K$  and the emission of shock waves as fast as 4000  $m/s$  [4, 13]. These gas temperatures are sufficient to produce visible light, a phenomenon called cavitation luminescence, and, if the collapse occurs in the proximity of a wall, the emitted shock waves and possible formation of liquid jets can cause significant erosion of the solid material.

In boiling cases, the growth rate is mainly governed by the evaporation rate of the interfacial liquid. Because of the latent heat of evaporation, the liquid at the interface is cooled towards the saturation temperature, at which point the evaporation rate becomes controlled by the ability of the phases to transport heat to the interface. Since the thermal conductivity is usually much higher in the liquid phase, the growth rate is thus governed by the heat transport in the liquid surrounding the bubble. The cooling of the interfacial liquid produces a thermal boundary layer around the bubble with a thickness that can be of the order of nanometers. Such small scales significantly complicate simulations of the growing bubble since a well-resolved thermal boundary layer is necessary to accurately capture the liquid heat transport that governs the evaporation rate.

To predict the evolution of boiling or cavitation vapour bubbles, the model must take into account both fluid- and thermodynamic effects and include the effects of surface tension and phase change at the interface. Because of the fast dynamics, compressibility effects can be significant, and at the moving bubble interface, large transient gradients of the

fluid conditions need to be accurately estimated. The number of physical phenomena and their complex interactions constitute a major modelling challenge. Indeed, research on this topic has been conducted for over a century and is still ongoing. Rayleigh (1917) [10] developed an equation for the growth of an inertia-controlled spherical vapour bubble. This formulation was further developed by, among others, Plesset and Zwick (1954) [11], Scriven (1959) [14], Mikic et al. (1970) [15], Dalle Donne and Ferranti (1975) [16], Prosperetti and Plesset (1978) [17] and Lee (1993) [18] to consider growth regimes governed by thermal and surface tension effects. Although the mathematical models provide great insight into the governing physical mechanisms, they typically rely on assumptions and simplifications that are only valid under certain conditions and growth regimes.

## 2.3 Dynamics of small-scale rising bubbles

The rising motion of gas bubbles in a liquid has intrigued researchers for a long time. In a quiescent liquid, the bubble trajectory can be rectilinear, zigzagging, spiralling or even chaotic depending on the governing parameters of the two-phase flow [19]. Interestingly, already Leonardo da Vinci documented in the 1500s that the dynamics are indeed three-dimensional, and Prosperetti (2004) termed the path instability phenomenon as Leonardo’s Paradox since it was not known why an axisymmetric bubble would move in a zigzagging, spiralling or chaotic path [20]. More recent numerical investigations of this phenomenon have shown that the shape and path of a rising bubble are closely associated and depend upon specific force ratios of the two-phase flow [21, 22].

For a single bubble rising in a quiescent liquid, the problem is completely described by the following four dimensionless governing parameters [23]; the Galilei number  $Ga = \frac{\rho_l \sqrt{gD} D}{\mu_l}$  that relates buoyancy to viscous forces, the Eötvös number  $Eu = \frac{\rho_l g D^2}{\sigma}$  that relates buoyancy to surface tension forces, the density ratio  $\rho_r = \frac{\rho_l}{\rho_g}$  and the dynamic viscosity ratio  $\mu_r = \frac{\mu_l}{\mu_g}$ . Here,  $g$  is the gravitational acceleration,  $D$  is the spherical equivalent bubble diameter,  $\sigma$  is the surface tension and  $l$  and  $g$  denote the liquid and the gaseous phases. If the bubble is rising in a shear liquid flow, also the dimensionless shear rate is introduced  $Sr = \frac{\omega D}{\sqrt{gD}}$  where  $\omega$  is the shear rate of the undisturbed liquid flow.

The interfacial forces acting on the bubble govern the rising path dynamics. In a quiescent liquid, the driving force on a bubble is buoyancy which is steady and only acts in the vertical direction. Therefore, it is somewhat surprising that an axisymmetric bubble may rise with a zigzagging, spiralling or chaotic trajectory. Consequently, other interfacial forces acting on the bubble oscillate or, in the chaotic regime, vary without any regularity. Developing models that can predict the correct interfacial forces for all governing parameters is thus a formidable task. As a result, most interfacial force models focus on predicting the forces for a given range of governing parameters and often with a quasi-steady approach to avoid describing the complex transient behaviours.

Currently, the most common method for modelling the interfacial forces and the resulting bubble motion is to use an equation of motion such as

$$\rho_g \frac{d\mathbf{V}}{dt} = \rho_l \frac{D\mathbf{U}}{Dt} - \rho_l C_{AM} \frac{d}{dt}(\mathbf{V}_{rel}) - \frac{3\rho_l}{4D} C_D |\mathbf{V}_{rel}| \mathbf{V}_{rel} - \rho_l C_L \mathbf{V}_{rel} \times \boldsymbol{\omega}_U + (\rho_g - \rho_l) \mathbf{g} \quad (2.3)$$

where the terms represent the inertia, added mass, drag, lift and buoyancy forces [24]. The  $\mathbf{V}$  is the bubble velocity vector,  $\mathbf{V}_{rel}$  is the relative velocity between the bubble and the undisturbed liquid at the bubble position,  $\boldsymbol{\omega}_U$  is the vorticity of the undisturbed liquid, and  $C_{AM}$ ,  $C_D$  and  $C_L$  are the added mass, drag and lift force coefficients, respectively. Note that additional forces such as the Basset (history) force and the pressure gradient force should also be considered in general but are here neglected for brevity.

Although the functional form of Equation 2.3 is relatively simple, it is generally difficult to determine the correct values for the force coefficients. The added mass force takes into account the inertia of the liquid that moves with the bubble and the force coefficient  $C_{AM}$  represents the ratio of the bubble volume to the moving liquid volume.  $C_{AM}$  depends on the orientation of the bubble relative to the flow and is, in general, a second-order tensor with components according to complex functions of all the governing parameters. For a spherical bubble, the isotropic value  $C_{AM} = 0.5$  holds [25] and, for simplicity, this value is often assumed also for non-spherical bubbles in viscous flows. There exist numerous correlations for  $C_{AM}$  but still none that is universally applicable for all types of bubble-liquid systems.

At a steady rising motion in a quiescent liquid, the only forces acting on the bubble are the drag and buoyancy forces that balance exactly. To predict the correct rising velocity, it is therefore important to use an accurate value for the drag force coefficient  $C_D$ .  $C_D$  is, however, also a complex function of all the governing parameters, and except for near-spherical bubbles in the low- and high- $Ga$ -number regimes, there is no satisfactory explanation describing the drag force acting on a bubble [26]. Because of its importance, the drag force has been extensively studied and now there exist many correlations for  $C_D$ , each valid in certain ranges of the governing parameters [27].

When bubbles rise in a shear flow ( $\boldsymbol{\omega}_U$  is non-zero), a shear-induced lift force acts on the bubble in a direction perpendicular to its relative motion. This lift force influences the spatial distribution of bubbles in important bubbly flow systems such as bubbly pipe flows [28] and affects the flow stability in bubble columns [29]. The lift force coefficient  $C_L$  is also a complex function of the governing parameters and may even change sign at increasing bubble deformations. The  $C_L$ -value varies significantly and highly non-linearly with the governing parameters because of the interaction of four different lift force mechanisms, some of which we only recently have begun to understand [30]. Theoretical predictions for  $C_L$  are thus limited to, for example, spherical bubbles in the low [31], and high- $Ga$ -limits [32], but for deformed bubbles at finite  $Ga$ -numbers, we still rely on incomplete correlations.

Bubbles that come into contact may coalesce and form larger bubbles with different governing parameters that consequently display entirely different dynamics [33]. Conversely,

if the surface tension force is not sufficient to keep the integrity of the bubble interface, external flow forces may cause the bubble to breakup into smaller bubbles [34]. In certain bubbly flow systems, these two processes govern the global bubble size distribution and can therefore alter the dynamics and characteristics of the entire system. However, rigorous models for the breakup and coalescence dynamics are not yet available.

To accurately predict the behaviour of large-scale bubbly flows, models are needed to predict all the above-mentioned small-scale dynamics. Without such models, the simulations of large-scale systems need to resolve all small-scale dynamics leading to unfeasible computational costs. To develop improved closures that are more universally applicable, we generally require a better physical understanding of the phenomena behind the small-scale dynamics. Such knowledge can then facilitate the design of robust theoretical or empirical models to describe the physics in the entire range of relevant governing parameters.

Next, we outline bubble dynamic processes at intermediate and large scales and discuss how they are coupled with the small-scale dynamics.

## 2.4 Dynamics of intermediate and large-scale bubbly flows

The rising of a single bubble disturbs the surrounding liquid and, consequently, influences the dynamics of other bubbles nearby. Therefore, the interfacial forces that govern single bubble dynamics are altered by the presence of nearby bubbles [35]. In certain flows, this hydrodynamic interactions between the individual bubbles cause bubble clustering and the formation of bubble swarms with a seemingly collective bubble behaviour [36]. To capture this phenomenon, models for the interfacial forces acting on a single bubble thus need to be modified to predict the motion of the bubbles when the latter are in bubble swarms.

Individual bubbles rise due to buoyancy induced by the gravitational force. At large scales, spatially nonuniform bubble distributions produce an inhomogeneous gravitational force distribution. These inhomogeneous forces induce large-scale flows that may enhance the inhomogeneity of the bubble distribution and can even produce large-scale turbulent flows [1]. At intermediate scales, the liquid turbulence may induce bubble dispersion that acts as to increase the spatial homogeneity of the spatial bubble distribution [37]. At small scales, bubbles can both induce and dampen the turbulent fluctuations of the liquid phase [5]. These complex multiscale processes cause different statistical properties of the liquid fluctuations compared to single-phase flows. The turbulent kinetic energy spectrum of the bubble-induced turbulence is found to have a  $-3$  power law scaling [38–44] at length scales comparable to or below the bubble size. This is in contrast with the classical  $-5/3$  scaling at inertial scales found in isotropic single-phase turbulence. In addition, the Probability Density Functions (PDFs) of the liquid velocity fluctuations are

found to be non-Gaussian and anisotropic due to the preferential motion of the bubbles in the direction of the buoyancy force [39, 40].

The turbulent characteristics in bubbly flows have implications also for the transport of scalar fields such as heat or chemical species. Recently, numerical and experimental studies have examined the great potential of bubbly flows as a relatively simple means for efficient scalar mixing due to the liquid agitation induced by the rising bubbles [42, 45–48]. Still, it is not entirely clear how the characteristics of the bubble-induced turbulence influence the dynamics and statistics of the passive scalar.

In certain bubbly flow applications, such as bubble columns and heat exchangers, the mixing and turbulence are fundamental flow properties to control for efficiently designed processes. However, these properties have a complex dependency on a number of governing parameters and are thus challenging to predict. Consequently, existing bubble-induced turbulence models and models for passive scalar transport in large-scale bubbly flows are still incomplete.

As illustrated in Figure 1.1 and in this section, the bubble dynamic processes occurring at all scales are generally coupled. Therefore, we generally need to solve a coupled multi-scale problem to model the dynamics of complex bubbly flow systems such as bubble columns or saturated nucleate pool boiling. In multi-scale problems, the accuracy of all models is important to predict the correct dynamics of the entire system. Therefore, we need a clear understanding of all the relevant processes and to develop robust and accurate models for them. In the next section, we give a brief overview of a simulation strategy to solve the multi-scale problem using such models.

## 2.5 Multi-scale modelling strategies

To handle a wide range of spatial and temporal scales, it is common to use a bottom-up multi-scale simulation strategy [49] as illustrated in Figure 2.1. In this approach, certain numerical techniques are used to investigate phenomena at one scale and to derive closures that can be used in numerical methods for bubbly flows at larger scales.

The smallest scales in the flow can be resolved by multiphase Direct Numerical Simulations (DNS). The DNS approach fully resolves the bubble shape and the flow field in the gas and liquid phases. The DNS typically provides all relevant information about the two-phase flow and thus constitutes an indispensable tool to study and understand the underlying physical phenomena behind complex bubble dynamics. The method, therefore, facilitates the development of improved closures for the bubble dynamic processes. However, multiphase DNS is currently only practical for studying up to  $O(10) - O(100)$  bubbles due to the excessive computational cost of resolving all scales.

At intermediate scales, the Eulerian-Lagrangian (EL) approach is practical to study systems with up to about  $O(10^6)$  bubbles. Here, the flow field around the bubbles and

the bubble shapes are not resolved, and the motion of the bubbles is determined using an equation of motion with interfacial force closures (as in Equation 2.3). By including additional closures for the coalescence and breakup processes, it is also possible to obtain the bubble size distribution from EL simulations.

To model industrial-scale systems, the Eulerian-Eulerian (EE) continuum approach is typically used where both the gas and liquid phases are treated as interpenetrating continua. Here, interfacial force closures and bubble coalescence and breakup models are generally needed and supplemented with bubble population balance models. Also hydrodynamic interaction of bubbles and bubble-induced turbulence effects requires consideration. Since the EE simulation technique depends on a high number of closures, the accuracy is determined by the quality of those closures. This limitation highlights the importance of performing further studies related to the bubble dynamics in order to achieve robust closures and improved predictions of industrial bubbly flows.

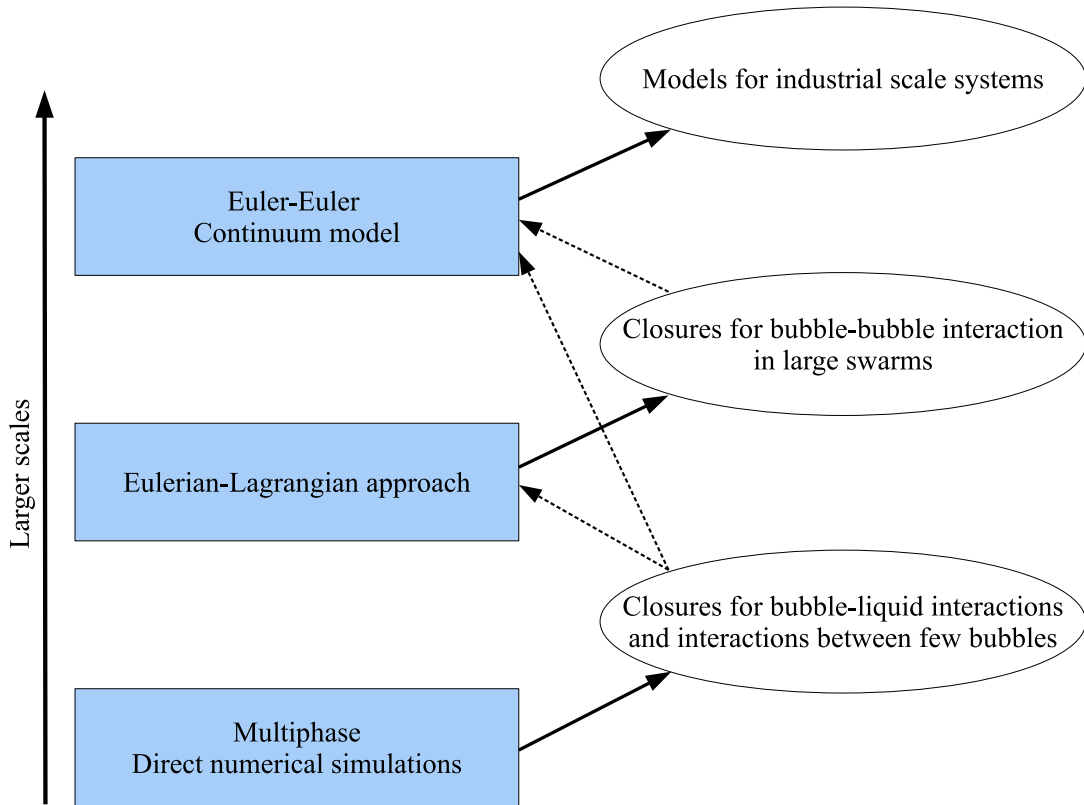


Figure 2.1: *Illustration of the bottom-up multi-scale modelling approach in bubbly flows.*

## 2.6 Objectives of the research work

Based on the background given above, there are many open questions and model uncertainties that require further investigations in an attempt to improve our physical

understanding and the ability to model bubbly flows in general. In this thesis we have chosen to focus on the following set of topics and objectives that span from small to large scales of bubbly flows.

## **Evolution of small-scale vapour bubbles**

The first topic concerns the evolution process of vapour bubbles and the fluid conditions in the vicinity of such bubbles. We focus on the laser-induced thermocavitation method that exemplifies challenges from both boiling and cavitation events. Because of the complex physics and extreme fluid conditions, theoretical models for the bubble evolution and fluid conditions are not yet complete. To facilitate the study of the bubble evolution process and the detailed flow conditions, our main objectives are:

- to develop a numerical framework for small-scale bubble evolution processes taking all relevant physics, such as interfacial phase-change into account and
- to determine the flow conditions in the gas and liquid phases of specific laser-induced thermocavitation events and examine the influence of relevant governing parameters on those conditions.

These objectives are addressed in Section 3.1 and Papers A and B. We develop two numerical frameworks; a multiphase DNS framework with phase change modelling outlined in Section 3.1.1 and described in detail in Paper A, and a corresponding 1D numerical framework presented in Section 3.1.2 and Paper B. In these papers, we numerically investigate the fast and complex dynamics of laser-induced thermocavitation events that are currently studied as a promising tool for controlling the process of crystallisation. Selected results from these studies are also presented in Section 4.1.

## **Small-scale rising bubble dynamics**

We shift the focus to small-scale rising bubble dynamics in both laminar and turbulent flows. We identify two key issues in conventional simulation techniques that prevent straightforward and efficient numerical studies of such problems. First, the studied bubble dynamic process may develop over a large range of spatiotemporal scales or occur at a location and time that are not known a priori. This issue makes it difficult to select an appropriate domain size and can lead to computationally unfeasible DNS costs. Second, the turbulent flow often includes length scales much larger than the bubble size. The latter issue makes it computationally very costly to resolve all relevant scales in the same numerical framework. To facilitate efficient numerical studies of this problem, we, therefore, formulate the following objectives:

- to develop a numerical framework for the rising bubble dynamics without a need for a priori knowledge about the spatiotemporal scales over which the dynamics develop, and
- to develop a general methodology for studying the small-scale rising bubble dynamics in response to a realistic turbulent flow with length scales larger than the bubble size.

These objectives are the focus of Paper C. Here, we focus on a bubble rising in a turbulent flow with a size comparable to or smaller than the Kolmogorov scales of the turbulent flow. We couple two fluid dynamic solvers into a general multiscale numerical framework that constitutes an efficient numerical tool for studying the small-scale bubble dynamics in response to turbulent fluctuations or laminar flows. The first solver is a multiphase DNS framework with a Moving Reference Frame (MRF) technique that resolves the detailed flow around the bubble (outlined in Section 3.2.1). The other solver is an EL-solver that simulates the turbulent flow at scales larger than the bubble size (Section 3.2.2). Example results from the first solver are presented in Section 4.2 and from the coupled framework in Section 4.2.1.

## Shear-induced lift force acting on individual bubbles

Here, we focus on the physical mechanisms behind the lift force acting on bubbles rising in shear flows. As discussed in Section 2.3, the lift force is dependent on four distinct lift force mechanisms. The complex interactions of these mechanisms induce a lift force that is a complex function of all governing parameters and, consequently, not yet fully understood. To increase our understanding of the lift force and facilitate improved closures, we define the following objectives:

- to provide a general description for the four lift force mechanisms based on the same flow features,
- to qualitatively explain how the different mechanisms cause the complex lift force behaviour under a wide range of the governing parameters, and
- elucidate the role of the shear rate on the four lift force mechanisms.

We address these objectives in Paper D, where we provide a theoretical framework that relates the bubble-induced vorticity to the lift force. Theoretical considerations are supported with the multiphase DNS framework developed in Paper C and outlined in Section 3.2.1. This framework is also used to investigate the role of the shear rate on the lift force in Paper D.

## Large-scale scalar dynamics in bubbly flows

Our last topic concerns the dynamics and statistics of passive scalar transport in bubbly flows at large scales. Although the statistical properties of bubble-induced turbulence are well established, it is still not clear how those properties influence the dynamics and statistics of the passive scalar. To investigate and quantify the scalar transport properties in bubbly flows, we define these objectives:

- to develop a numerical framework to study passive scalar transport in monodisperse turbulent bubbly flows and
- to determine how the bubble-induced turbulence influences the passive scalar dynamics and assess the effects of relevant governing parameters on the dynamics.

The first objective is addressed in Section 3.3 and Paper E where we develop and use a multiphase DNS framework with a repulsive force model to avoid coalescence. In Paper E, we focus on the second objective by using DNS simulations to show how the scalar dynamics differ in bubbly flows compared to isotropic single-phase turbulence. We also investigate the effects of several relevant governing parameters on the dynamics and statistics of the scalar transport.

In the next section, we present an overview of the developed numerical frameworks and expand on some details not covered in the appended papers. Selected results from the numerical frameworks are presented in Section 4.



# 3 Numerical frameworks for bubble dynamics from small to large scales

In this section, we present the numerical frameworks developed in relation to the objectives of this thesis. The frameworks are described in detail in the appended papers, but here we provide an overview and expand on additional details not covered in the papers. First, we present our numerical frameworks developed for studying the evolution of small vapour bubbles (Paper A and Paper B). Then, we outline our multiscale methodology for investigating small-scale rising bubble dynamics in both laminar and turbulent flows (Paper C). The multiscale methodology comprises the coupling of an EL and a multiphase DNS fluid solver with a moving reference frame technique. The latter solver is also used in Paper D to study the shear-induced lift force. Finally, we outline the numerical framework used for studying passive scalar dynamics in bubble-induced turbulence (Paper E).

## 3.1 Numerical frameworks for the evolution of small-scale vapour bubbles

To capture a general bubble evolution process, a numerical framework needs to take into account a great number of relevant phenomena such as fluid- and thermodynamics effects, phase change and surface tension effects. As discussed in Section 2.2, several mathematical models are developed for this kind of bubble dynamics, but those models are derived for bubble evolution under specific conditions and evolution regimes.

We aim to investigate the evolution of the fluid conditions in the vicinity of a laser-induced thermocavitation bubble. The laser-induced thermocavitation method exemplifies challenges and complexities of both the boiling and cavitation processes. Here, the bubble exhibits the fast dynamics characteristic for cavitation bubbles, but the bubble growth rate is governed by rapid phase change and thermal effects. These types of bubbles constitute a major modelling challenge and are, therefore, useful cases to study in an attempt to formulate a general numerical framework.

We avoid the typically used modelling assumptions such as homogeneous vapour conditions, constant physical properties and negligible viscous- inertia- or thermal effects during specific bubble evolution periods. Instead, we consider all relevant effects during the entire evolution process and resolve the fluid conditions in both space and time for both phases taking into account the variation of the physical properties. This approach adds complexity and requires a higher computational cost compared to when using simplified models but provides a more general methodology for predicting many vapour bubble evolution processes.

By resolving the two-phase fluid conditions, we also obtain detailed information about the spatiotemporal variations of those conditions, which is essential in certain applications such as laser-induced thermocavitation bubbles used for crystallisation. This application is further discussed in Section 4.1.

In the following section, we outline our multiphase DNS framework with phase-change modelling, and in Section 3.1.2, we describe our 1D numerical framework suitable for extensive parameter investigations due to its almost negligible computational cost compared to that of the DNS framework.

### 3.1.1 Multiphase DNS framework for vapour bubble evolution

To investigate the laser-induced thermocavitation bubbles numerically, we use a multiphase DNS fluid solver that accounts for thermal effects in both phases, surface tension, and includes the effects of the interfacial phase change. Because of the rapid dynamics, also compressibility effects are considered. This framework is described in detail in Paper A and extended in Paper B. Here, we present an outline of the framework and provide additional discussion regarding numerical challenges and limitations.

A major numerical challenge in multiphase DNS of bubbly flows is the presence of the interface between the fluid phases. The interface is a 2D phenomenon (it does not have a thickness) in the fluid continuum assumption. It is thus not possible to resolve the interface with the standard finite volume method. Therefore, special numerical methods have been developed to handle the discontinuity between the phases and the position of the interface within the finite volume approach.

We use in this work the Volume Of Fluid (VOF) method to handle the two-phase flow [50]. Here, the volume fraction field of the phases is tracked, and the interface between the phases is identified as the position where the volume fraction field is between 1 and 0. With this approach, the interface can be treated in the same finite volume approach as the other governing equations, which significantly reduces the complexity of the numerical method.

In the volume fraction field, the transition from one fluid phase to the other occurs over the length scale of at least one computational cell. It is therefore not trivial to define rigorously the exact location and orientation of the interface at the scale of individual cells. At a curved interface, the surface tension induces a net force in the interface normal direction, and if the surface tension varies along the interface, also a tangential force is induced at the interface (a phenomenon called the Marangoni effect). Since these forces act on the 2D interface, it is not trivial to include them in the finite volume method either.

In the case of a laser-induced thermocavitation bubble, the bubble is small, and the interface is highly curved. This lead to high forces in the interface normal direction. These

forces are implemented as volume forces in the computational cells containing the interface. For the highly curved, deformable and rapidly moving interfaces of our application, the numerical implementation of the interfacial forces needs careful consideration. To accurately resolve such interfaces, high spatial and temporal resolutions are required, and to maintain a sharp interface, we use the PLIC interface reconstruction method that estimates the location and orientation of the interface within the computational cells at each computational time step [51]. This method avoids smearing of the interface that may occur in other numerically diffusive volume fraction advection schemes. The interfacial forces are implemented using the method proposed by Brackbill et al. [52] that depends on an accurate representation of the interface to predict the correct forces.

The phase change (evaporation or condensation) occurs at the interface and governs the evolution of the bubble in the laser-induced thermocavitation case. This is a complex process that involves the transport of both heat and mass across the interface and the absorption or release of thermal energy due to latent heat. To include these phenomena in the VOF method, we implement the approach proposed by Hardt & Wondra [53] and extend it to increase accuracy and reduce numerical instabilities at the interface (that may arise in the extreme case of laser-induced thermocavitation). In this approach, the effects of phase change are included by a phase change model that determines mass and energy source terms in the computational cells at the vicinity of the interface. The source terms model the effects of the phase change and ensure that the correct amount of mass and energy that is added at one side of the interface is removed on the other side. The implementation of the phase change model is explained in detail in Papers A and B and the choice of model is further discussed in Section 3.1.2.

In this numerical framework, we consider both phases as compressible and solve for the entire system of continuity, volume fraction, momentum and energy governing equations together with the phase change model. Apart from the need for a high spatial resolution to resolve the interface and thin boundary layers, the phase change model introduces additional constraints on the temporal resolution required for solving the governing equations. These constraints are typically limiting the time step size during periods of high phase change rate. To reduce the total computational cost of a simulation, we use a variable time step size that is always less than or equal to the minimum of all constraints.

The phase change model introduces mass source terms  $S_{Cq}$  proportional to the phase change rate in computational cells close to the interface. With a given time step size and sufficiently high phase change rate, a cell could potentially be emptied during the computational time step. To limit the reduction of the density in the cells during a time step, we, therefore, define the constraint

$$\Delta t_\rho \leq \min_{\Omega} \left( \frac{\rho}{|S_C|} \right) \beta, \quad \forall S_C < 0, \quad (3.1)$$

where  $\rho$  is the density of the cell and  $\beta = 0.1$  is a maximum allowable reduction ratio. Since the phase change is dependent on the temperature at the interface, we also need to ensure that the temperature does not change too much during one time step. The temperature is influenced by the energy source terms  $S_h$  determined by the phase change

model. Here, we found that limiting the change to  $\Delta T_{max} = 3 \text{ K}$  gave reasonable numerical stability. This constraint is defined by

$$\Delta t_T \leq \min_{\Omega} \left( \frac{\Delta T_{max} c_p \rho}{S_h} \right), \quad (3.2)$$

where  $c_p$  is the fluid specific heat capacity. Apart from the standard CFL-criterion, the time step size is also restricted by the capillary time step constraint [54]

$$\Delta t_{\sigma} \leq \sqrt{\frac{(\rho_l + \rho_g) \Delta x^3}{2\pi\sigma}}, \quad (3.3)$$

where  $\rho_l$ ,  $\rho_g$ ,  $\Delta x$  and  $\sigma$  are the liquid and gas densities, cell size and the surface tension coefficient, respectively. This constraint ensures the resolution of the shortest numerically represented capillary wave and is typically limiting the time step size during periods of less intense phase change. In our simulations of laser-induced thermocavitation events, we use cell sizes of  $50 \text{ nm}$  that give a capillary time step constraint of about  $\Delta t_{\sigma} = 5.8 \times 10^{-10} \text{ s}$  while  $\Delta t_{\rho}$  and  $\Delta t_T$  vary in the ranges of about  $1 \times 10^{-10}$  to  $1 \times 10^{-11} \text{ s}$  during the periods of evaporation or condensation. The thermocavitation event is typically  $O(10 \mu\text{s})$  indicating  $O(1 \times 10^5)$  time steps are required. These limiting constraints, in conjunction with a spatial grid of  $O(1 \times 10^6)$  cells, result in a very large computational cost and thus limit the practical applicability of this DNS framework for studying a wide range of parameters. The high computational cost was indeed the main incentive for developing the 1D numerical framework outlined in the next section.

The DNS numerical framework is developed, validated and described in detail in Paper A and in Paper B, we further develop it to improve the accuracy of the interfacial energy transfer. We also simulate an experimentally observed laser-induced thermocavitation event and predict bubble growth rates in reasonable agreement with the experimental measurements. In Paper B, we further study the laser-induced thermocavitation event and assess the evolution of solute supersaturation on the liquid side of the interface.

### 3.1.2 1D Numerical framework for vapour bubble evolution

As discussed in the section above, there is a very large computational cost associated with the multiphase DNS and phase change model that makes extensive parameter investigations practically impossible. However, the small size of the laser-induced cavities makes them approximately spherical (discussed in Section 2.2), and by assuming that the bubble evolution occurs far from an external boundary, the entire process can be approximated as spherical-symmetric. This approximation allows us to formulate the entire problem in a 1D framework, in the radial direction  $r$ , taking into account thermal effects, surface tension, interfacial phase change and vapour compressibility effects. This approach reduces the computational cost to an almost negligible fraction of the DNS framework. The 1D framework is described in detail in Paper B, but we provide here an outline and expand on a few numerical aspects not covered in that paper.

The 1D problem is divided into a vapour region  $0 \leq r < R(t)$  and a liquid region  $R(t) \leq r < \infty$  separated by the time-dependent bubble interface at  $r = R(t)$ . The evolution of  $R(t)$  is computed from the generalised Rayleigh-Plesset Equation 2.2 where we also have included the effects of phase change on the liquid velocity as

$$2\dot{R}(\dot{R} - j/\rho_l) + R(\ddot{R} - \dot{j}/\rho_l) - \frac{1}{2}(\dot{R} - j/\rho_l)^2 + \frac{2\sigma}{R\rho_l} + \frac{4\mu_l}{R\rho_l}(\dot{R} - j/\rho_l) = \frac{p_v|_{r=R} - p_\infty}{\rho_l}, \quad (3.4)$$

where  $p_\infty$  is the liquid pressure far from the bubble and  $j$  is the phase change mass flux. This equation is derived by substituting the incompressible liquid continuity equation into the incompressible momentum equation in the radial direction and then integrating from the bubble interface to far away in the liquid with the interface jump condition  $p_v|_{r=R} = p_l|_{r=R} + \frac{2\sigma}{R} + \frac{4\mu_l u_l|_{r=R}}{R}$ .

The effects of the phase change rate  $j$  on  $R(t)$  are often negligible in boiling and cavitation events since typically the interface velocity  $\dot{R} \gg j/\rho_l$ , where  $\rho_l \approx 1000 \text{ kg/m}^3$  for water. However, in certain laser-induced thermocavitation events, the evaporation rate can reach values of  $O(1000) \text{ kg/(m}^2\text{s)}$  shortly after the laser pulse that gives  $O(\dot{R}) = O(j/\rho_l)$  indicating that the phase change rate should be taken into account in Equation 3.4.

Equation 3.4 also shows that it is the pressure in the vapour at the interface  $p_v|_{r=R}$  that governs the evolution of  $R(t)$ . It is thus important that the vapour pressure is predicted accurately. This pressure is dominated by the evaporation rate  $j$  across the interface during the initial bubble growth period. The evaporation rate is consequently also important to predict correctly. However, models for estimating the phase change rate are currently not universal and generally unable to predict accurately the correct physics of the mass and energy transfer at the gas-liquid interface [55].

Two common approaches for estimating the local mass transfer rate at the interface are the energy (or Rankine-Hugoniot) jump condition and the Schrage model [55]. The former determines  $j$  from the energy balance at the interface

$$j\mathcal{L} = \lambda_l \frac{\partial T_l}{\partial \mathbf{n}} \Big|_l - \lambda_v \frac{\partial T_v}{\partial \mathbf{n}} \Big|_v \quad (3.5)$$

where  $\mathcal{L}$  is the latent heat of phase change and  $\partial/\partial \mathbf{n}$  indicates the gradient on the either side of the interface in the normal direction. However, to evaluate the temperature gradients in the interface normal direction, non-trivial discretisation schemes are required and typically, the information about the interface temperature that is often assumed at saturation conditions  $T_{sat}(p_l)$ . Mass transfer models based on the energy jump conditions and appropriate discretisation schemes are successfully implemented in, for example, [56, 57] to simulate vapour bubble growth in a liquid superheated by a few Kelvin.

The Schrage model is instead derived from the kinetic theory of gases and relates the flux of molecules across the interface to the pressure and temperature of the two phases

at the interface. The phase change rate  $j$  is determined by [58]

$$j = \frac{\chi}{\sqrt{2\pi B_v}} \left( \frac{p_{sat}(T_l|_{r=R})}{\sqrt{T_l|_{r=R}}} - \frac{\Gamma_v p_v|_{r=R}}{\sqrt{T_v|_{r=R}}} \right) \quad (3.6)$$

where  $\chi$  is the accommodation coefficient,  $T_l$  is the liquid temperature,  $p_v$  is the vapour pressure,  $p_{sat}$  is the saturation pressure,  $B_v$  is a material parameter and  $\Gamma_v$  is a correction factor. This model is derived by assuming saturation states of the phases but allows for a jump of temperature and pressure across the interface.

The available phase change models are typically based on simplifying assumptions such as maintained saturation temperature at the interface. This makes the applicability of these models uncertain in the case of laser-induced thermocavitation where the rapid heating by the laser pulse may lead to deviations from saturation states. However, the Schrage model has successfully been used to simulate laser-induced vapour bubbles in Akhatov et al. [59], and the model inherently allows for departure from saturation conditions. Instead of specifying constant saturation conditions at the interface, the Schrage model rather maintain approximately saturation conditions by predicting higher phase change rate as the conditions depart from saturation. This model does not require special discretisation schemes and is simpler to implement in the multiphase DNS framework than the energy jump condition. In the multiphase DNS framework, we use the model by Tanasawa [60] that is a simplified form of the Schrage model and only dependent on the local temperature at the interface. This further simplifies its implementation in the VOF framework. In the present 1D framework, we use the Schrage model as presented in Equation 3.6. The major drawback of the Schrage model is, however, the unknown accommodation (or phase change) coefficient  $\chi$  that, in general, requires experimental data or, in certain cases, can be specified high enough to attain sufficiently small deviation from saturation conditions at the interface [55]. In our simulations, we use values of  $\chi$  that give bubble growth rates in reasonable agreement with experimental data.

Equation 3.6 indicates that  $p_v$  is not only implicitly dependent on itself but also on the temperatures of the two phases at the interface. Therefore, it is important also that the temperatures are predicted accurately at the interface. Since the vapour conditions vary rapidly during the thermocavitation event, we model the vapour as a compressible gas. This approach ensures that we accurately resolve the spatial and temporal variations of the vapour conditions that influence the entire problem.

A key region to resolve spatially is the variation of the fluid conditions close to the interface where the intense phase change rate induces high gradients and mass transfer boundary layers of  $O(1 \times 10^{-8}m)$ . Here, the phase change produces high recoil pressures (that consecutively influence  $j$  according to Equation 3.6), and the latent heat of phase change gives a boundary condition for the heat flux at the interface according to Equation 3.5. According to Equation 3.5, a high value of  $j$  induces a high temperature gradient at the interface that needs to be sufficiently resolved. Since typically we have  $\lambda_v \ll \lambda_l$ , it is the heat flux on the liquid side of the interface that governs the heat available for evaporation.

Equation 3.5 indicates that high spatial resolution is required at the interface during periods of high rates of phase change. In the laser-induced thermocavitation events, the phase-change rate  $j$  typically reaches a maximum just after the laser pulse and then approaches zero in  $O(1\mu s)$ . Since the entire event is  $O(10\mu s)$ - $O(100\mu s)$ , the finest temporal and spatial resolution is only required during the initial growth period of the bubble (and during the collapse that we do not focus on).

To reduce the total simulation time, we implemented both a variable time step and an adaptive grid refinement technique. We use the standard CFL criterion with a Courant number of  $Co = 0.75$  in both phases as  $\Delta t_v \leq Co\Delta r/(u + a)$  in the vapour phase and  $\Delta t_l \leq Co\Delta r/u$  in the liquid phase, where  $\Delta r$  is the grid spacing,  $u$  is the fluid velocity, and  $a$  is the speed of sound in the vapor. Since we do not resolve any capillary waves in the 1D framework, the capillary time step constraint of Equation 3.3 is not necessary here. The time steps are further constrained analogously with Equation 3.1 and Equation 3.2 but here modified as

$$\Delta t_\rho \leq \frac{\rho_v V_{cv}}{j A_B \beta}, \quad (3.7)$$

where  $V_{cv}$  is the volume of the first computational cell on the vapour side of the interface,  $A_B$  is the bubble interface area and  $\beta = 0.1$ . This formulation limits both the increase and decrease of mass in the first computational cell on the vapour side of the interface during a single time step. The liquid side of the interface is assumed incompressible, which allows the continuity and momentum equations to be integrated in the radial direction to provide analytical relations for the velocity and pressure in the entire liquid region. Therefore, no time step constraint like Equation 3.7 is needed on the liquid side of the interface. Still, the energy equation for the liquid is not easily integrated because of the energy source term that represents the energy absorbed from a laser pulse. Instead, we use the finite volume method to discretise the energy equation in the liquid region. As discussed above, it is mainly the heat flux in the liquid phase that limits the phase change rate, and therefore we need to limit the maximum change of the liquid temperature during a time step in order to get stable solutions. This is achieved by the constraint

$$\Delta t_T \leq \frac{\Delta T_{max} c_{p,l} V_{cv} \rho_l}{\Delta j \mathcal{L} A_B}, \quad (3.8)$$

where  $\Delta T_{max} = 0.1 K$  and  $\Delta j$  is the change of phase change rate between two consecutive time steps. This formulation ensures that the time step size is sufficiently small when the phase change rate varies rapidly but allows larger time steps during periods of a more steady phase change. The use of  $\Delta j$  rather than  $j$  in Equation 3.8 can be explained with Equation 3.5 that shows that the heat flux from the liquid phase towards the interface balances the latent heat of evaporation. At a quasi-steady state, the heat flux through the liquid thermal boundary layer (at the bubble interface) is uniform, and the heat required for evaporation is supplied by the surrounding liquid outside the thermal boundary layer. Thus, the interface temperature  $T_l|_{r=R}$  does not change proportionally to  $j$  during periods of steady evaporation. It is rather during rapid changes of  $j$  (large  $\Delta j$ ) that the  $T_l|_{r=R}$  changes significantly until a quasi-steady state is reached again.

In a typical laser-induced thermocavitation simulation, the variable time step method results in time step sizes ranging from  $O(1 \times 10^{-13} \text{ s})$  during the laser pulse to  $O(1 \times 10^{-7} \text{ s})$  when the bubble is near its maximum radius, and the phase change is negligible. This method consequently reduces the simulation time by  $O(1000)$  times compared to a fixed time step of  $O(1 \times 10^{-13} \text{ s})$  and facilitates extensive parameter investigations.

The adaptive grid refinement technique is used both in the vapour and liquid regions and has two main advantages. Firstly, as the bubble grows or shrinks, the grid in the vapour phase is scaled proportionally to  $R(t)$ . With a fixed number of grid points, the grid would be either too coarse at large  $R$  or excessively fine at small  $R$ . By adapting the grid, an appropriate grid spacing can be maintained throughout the bubble lifetime. Secondly, large local gradients of the flow conditions are present, especially during the bubble growth and collapse phases. The adaptive grid then ensures that a sufficient grid resolution is used in those regions that vary both spatially and temporally during the simulation.

The grid point positions  $r_{v,i}$  in the vapour phase ( $0 \leq r < R(t)$ ) are defined in a coordinate system with the origin in the bubble centre  $r = 0$  and scaled with the evolving size of the vapour region as  $r_{v,i}(t) = r_{v,i}(0)R(t)/R(0)$ . The liquid region ( $R(t) \leq r \leq R(t) + R_\infty$ ) is defined with a large constant but a finite radial thickness  $R_\infty$  making it convenient to use a coordinate system that follows the bubble interface  $\hat{r} = r - R(t)$ . The liquid grid point positions  $\hat{r}_{l,i}$  in ( $0 \leq \hat{r} \leq R_\infty$ ) do therefore not require any scaling with  $R(t)$ .

The grid is adapted based on the first and second spatial derivatives of the temperature and density fields. To avoid too large changes of the conditions within a single computational cell, we define a cell cost function  $\epsilon$  for an arbitrary fluid variable  $X$  as

$$\epsilon_i(X) = \frac{\partial X}{\partial r} \Delta r_i \psi + \frac{\partial^2 X}{\partial r^2} (\Delta r_i)^2 (1 - \psi) , \quad (3.9)$$

where  $\Delta r_i$  is the cell thickness at the grid point  $i$  and  $\psi = 0.2$  is a weighting factor used to promote high resolution in regions with high curvatures. In the vapour region, the grid is refined if  $\epsilon_{v,i} = (\epsilon_i(T_v) + \epsilon_i(\rho_v))/2 > 0.025$  and coarsened if  $\epsilon_{v,i} < 0.004$ . In the liquid, the corresponding conditions are  $\epsilon_i(T_l) > 0.01$  and  $\epsilon_i(T_l) < 0.003$ . These values gave a sufficient resolution in our simulation cases. An example of the grid generated by the adaptive technique is shown in Figure 3.1 in the region close to the bubble interface. Here, the temperature in the liquid region is finely resolved close to the interface where the evaporation induces a thermal boundary layer of  $O(1 \times 10^{-7} \text{ m})$ . The first cell on the liquid side of the interface is only  $5 \text{ nm}$  in width. Further away from the interface, the liquid temperature is more uniform, and the adaptive grid method produces a significantly coarser grid.

The 1D framework is developed, validated and used for an extensive parameter study in Paper B. The validation cases consist of experimentally observed laser-induced thermocavitation bubbles, and the 1D framework predicts the bubbles radius evolution in good agreement with the experiments.

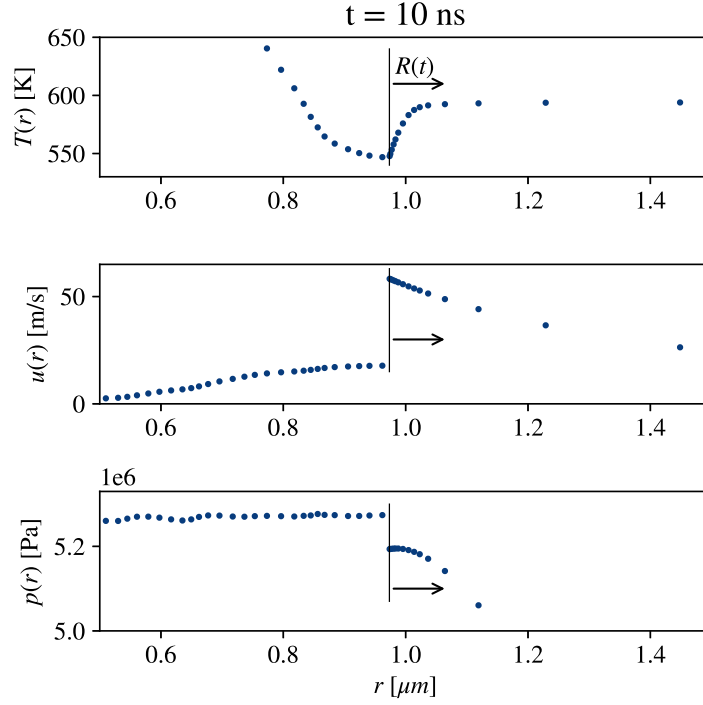


Figure 3.1: *Illustration of the adaptive computational grid used in the 1D numerical framework during the simulation of a laser-induced thermocavitation bubble at an instant 4 ns after a laser pulse of 6 ns has been applied. The vertical black line represents the bubble interface, and the arrow indicates the interface velocity direction. The flow conditions in both phases are shown in the region close to the interface, where typically, the first and second spatial derivatives are the largest. The blue dots represent the grid points  $r_i$  in the vapour and liquid regions. Here, it is clear that the adaptive grid method refines the grid in the regions with the highest changes in the fluid conditions. In the liquid phase, the grid is only used for the temperature, and here, the grid becomes coarse in the regions away from the interface where the temperature is more uniform.*

## 3.2 Numerical frameworks for small-scale rising bubbles

Here, we outline our numerical frameworks that focus on rising bubble dynamics at small scales. As discussed in Section 2, there is still a need for improved closures for, for example, interfacial forces, breakup, coalescence and bubble-induced turbulence effects. These closures can be developed or improved by detailed numerical investigations of the bubble dynamics using multiphase DNS methods in systems with few bubbles.

Many closures consider the quasi-steady bubble dynamics. A challenge with studying such dynamics is that the small-scale bubble process may occur at an a priori unknown location (such as breakup) or develop over relatively large spatial and temporal scales (such as unsteady trajectories) until a quasi-steady state is reached. Therefore, it is

difficult to a priori select a sufficient domain size, and the DNS simulations may require both large computational domains and long simulation times. These issues cause large computational costs and prohibit detailed numerical investigations across the relevant parameter ranges.

To facilitate more efficient DNS simulations of the small-scale bubble dynamics, we develop a numerical framework with a moving reference frame (MRF) technique that follows the motion of the bubble. The MRF technique significantly reduces the required size of the computational domain and avoids the problem of a priori determining the required size of the domain to capture the bubble dynamic process. This framework is described in the next section and in detail in Paper C. The framework is also used in Paper D to study the small-scale phenomena of the lift force acting on bubbles rising in a linear shear flow.

As discussed at the end of Section 2.3, a turbulent liquid field influences the small-scale bubble dynamics. The closures for the latter dynamics should therefore take turbulence into account. This is, however, a challenging topic to investigate numerically since the largest length scales of the turbulent field may be orders of magnitudes larger than a single bubble. To solve this problem, we couple an Eulerian-Lagrangian solver for the liquid turbulence with our multiphase DNS framework using the MRF technique that resolves the detailed bubble dynamics in response to the liquid fluctuations predicted by the EL solver. This framework is outlined in Section 3.2.2 and described in detail in Paper C.

### 3.2.1 Multiphase DNS with non-inertial moving reference frame

It is the flow field in the vicinity of the bubbles that governs the bubble dynamics. To reduce the required size of the computational domain, it is convenient to make a change of coordinates to a reference system moving with the bubble. By following the bubble, the computational domain only needs to encompass the near flow field, while the flow field far from the bubble is disregarded. Furthermore, a moving reference frame (MRF) technique removes the need to a priori estimate a sufficient domain size to capture bubble dynamics that may develop over relatively large spatiotemporal scales. For example, in Cano-Lozano et al. [19], a computational domain of  $128D$  in the vertical direction was required to observe the transition to path instability for a rising bubble and the development of different types of trajectories. The required vertical cross-section of the domain was, however, only  $8D \times 8D$ . Moreover, the MRF technique ensures that the distance between the bubble and the boundaries of the computational domain is constant during a simulation. It is thus sufficient to select an appropriate distance at the simulation initialisation/setup to avoid unwanted boundary effects.

In Paper C we develop, validate and demonstrate a multiphase DNS framework using the VOF approach and with a reference frame moving with the bubbles. The numerical framework is implemented in the open-source code Basilisk (basilisk.fr) [61]. Since the

framework is described in detail in Paper C we only provide a brief outline here and expand on some details not included in the paper.

The change of a coordinate system gives the following change of variables:  $\hat{\mathbf{x}} = \mathbf{x} - \mathbf{r}_{mrf}$ ,  $\hat{\mathbf{u}} = \mathbf{u} - \mathbf{V}_{mrf}$  and  $\hat{t} = t$ , where  $\mathbf{r}_{mrf}$  and  $\mathbf{V}_{mrf}$  are the position and velocity of the MRF in a laboratory reference frame. Since rising bubbles generally accelerate (especially at unsteady trajectories), the moving reference frame becomes non-inertial. In such reference frames, the acceleration of the reference frame should be included in the momentum equation for the flow in the MRF [24] according to

$$\rho \frac{D\hat{\mathbf{u}}}{D\hat{t}} = \rho(\mathbf{g} - \mathbf{a}_{mrf}) - \nabla p + \frac{1}{Ga} \nabla \cdot (\mu(\nabla \hat{\mathbf{u}} + \nabla \hat{\mathbf{u}}^T)) + \frac{\hat{\kappa} \delta_S \hat{\mathbf{n}}}{Eo}, \quad (3.10)$$

where the equation is made non-dimensional according to Section 3.2 and  $\mathbf{a}_{mrf}$  is the acceleration of the MRF. In our method, the reference frame acceleration is continuously adjusted to maintain the bubble at its initial position of the computational domain. Formally, the aim is to maintain  $\mathbf{a}_{mrf}(t) = \mathbf{a}_B(t)$  where  $\mathbf{a}_B$  is the bubble acceleration in the laboratory reference frame. Since  $\mathbf{a}_B = \frac{\partial}{\partial t} \left( \frac{1}{\Omega_g} \int_{\Omega_g} \mathbf{u} d\Omega \right)$ , where  $\Omega_g$  is the volume occupied by the gas phase, is determined by the solution of the governing flow equations (including  $\mathbf{a}_{mrf}(t)$ ), it is not trivial to exactly secure that  $\mathbf{a}_{mrf}(t) = \mathbf{a}_B(t)$ . The  $\mathbf{a}_{mrf}(t)$  can be estimated in many ways, and in Paper C, we have chosen to determine  $\mathbf{a}_{mrf}(t)$  using a Proportional-Integral-Derivative (PID)-controller approach. Other methods such as a simple explicit extrapolation of the acceleration to the next time step  $n+1$  as  $\mathbf{a}_{mrf}^{n+1} = \mathbf{a}_{mrf}^n + \frac{\mathbf{a}_{mrf}^n - \mathbf{a}_{mrf}^{n-1}}{\Delta t^n} \Delta t^{n+1}$  (where  $\Delta t^{n+1} = t^{n+1} - t^n$ ) introduces small errors that, when integrated over long simulation times, were found to give considerable deviations of the bubble position to its initial position in the MRF. The PID-controller approach solves this problem by instead minimising the deviation  $\mathbf{e}$  of the bubble position from its initial position  $\mathbf{e} = \hat{\mathbf{r}}_B(t) - \hat{\mathbf{r}}_B(t=0)$  in the MRF by continuously adjusting  $\mathbf{a}_{mrf}(t)$ . With appropriately chosen PID-coefficients, we thus get  $\mathbf{a}_{mrf}(t) \approx \mathbf{a}_B(t)$  without accumulating deviations of the bubble position over time. This approach also gives a general implementation that can handle both single and multiple bubble systems since we consider the centre of mass of the entire gas phase.

A DNS example of using the PID-controlled MRF with a domain size of  $(25D)^3$  is shown in Figure 3.2. Here, a bubble is rising in a linear shear flow ( $U_y = -0.1x$ ) with a helical trajectory. In panel (a), the trajectory is shown in the lab reference frame, and in panel (b) the total deviation  $|\mathbf{e}|$  of the bubble centre of mass from its initial position in the MRF is less than  $0.004D$  throughout the simulation. This illustrates that the PID-control approach maintains  $\mathbf{a}_{mrf}(t) \approx \mathbf{a}_B(t)$  without introducing small displacements that accumulate over time.

Since the flow field in the MRF is accelerated, the boundary conditions in the MRF domain must be updated correspondingly. Considering a bubble rising in an undisturbed liquid flow field  $\mathbf{U}(\mathbf{x}, t)$ , the velocity at an inlet boundary at a current time  $t^n$  and the

later time  $t^{n+1}$  is

$$\hat{\mathbf{u}}_{BC}^n(\hat{\mathbf{x}}) = \mathbf{U}^n(\hat{\mathbf{x}} + \mathbf{r}_{mrf}^n) - \mathbf{u}_{mrf}^n, \quad (3.11)$$

$$\hat{\mathbf{u}}_{BC}^{n+1}(\hat{\mathbf{x}}) = \mathbf{U}^{n+1}(\hat{\mathbf{x}} + \mathbf{r}_{mrf}^{n+1}) - \mathbf{u}_{mrf}^{n+1}, \quad (3.12)$$

where we define  $\mathbf{r}_{mrf}^{n+1} = \mathbf{r}_{mrf}^n + 0.5(\mathbf{u}_{mrf}^{n+1} + \mathbf{u}_{mrf}^n)\Delta t^{n+1}$  and  $\mathbf{u}_{mrf}^{n+1} = \mathbf{u}_{mrf}^n + \mathbf{a}_{mrf}^{n+1}\Delta t^{n+1}$ . Here,  $\mathbf{a}_{mrf}^{n+1}$  is determined by the PID-controller and defined as the constant MRF acceleration between  $t^n$  and  $t^{n+1}$ . A linear variation of  $\hat{\mathbf{u}}_{BC}$  from  $t^n$  to  $t^{n+1}$  can thus be defined as

$$\hat{\mathbf{u}}_{BC}^{n \rightarrow n+1}(\hat{\mathbf{x}}, t) = \mathbf{U}^n + \frac{\mathbf{U}^{n+1} - \mathbf{U}^n}{\Delta t^{n+1}}(t - t^n) - \mathbf{u}_{mrf}^n - \mathbf{a}_{mrf}^{n+1}(t - t^n). \quad (3.13)$$

This formulation provides a consistent velocity boundary condition also for fields defined at fractional time steps such as  $t^{n+1/2}$ .

With this framework, the computational cost of the DNS simulations can be significantly reduced, and setting up the simulations, e.g. specifying the domain size, is simplified. This framework, therefore, facilitates more efficient numerical investigations of the small-scale bubble dynamics that can be used to develop new or improve existing closures. Indeed, this framework is used in Paper D to qualitatively explain the mechanisms behind the shear-induced lift force and to examine the role of the liquid shear rate on the lift force.

### 3.2.2 Coupled Eulerian-Lagrangian and multiphase DNS frameworks for small-scale bubble dynamics in turbulence

Here, we aim to study the dynamics of an individual bubble rising in a turbulent liquid flow. The turbulent flow influences the small-scale bubble dynamics (such as interfacial forces, breakup and coalescence), and for this reason, the closures for those dynamics should take turbulence into account. To develop improved closures, we need detailed studies of the dynamics under a wide range of the governing parameters. Using conventional numerical tools is challenging since DNS of the turbulent flow generally requires accurate resolution in domains and length scales much larger than the bubble. We solve this problem by coupling the Eulerian-Lagrangian (EL) numerical method (to resolve the turbulent liquid flow) with the multiphase DNS method (to resolve the small-scale bubble dynamics). The framework is described in detail in Paper C, but here we provide a short outline and discuss some numerical implementations not mentioned in the paper.

The EL solver simulates a turbulent liquid field and tracks a Lagrangian bubble rising in that field. The liquid phase fluctuations experienced by the bubble  $\mathbf{u}_B^{EL}(t)$  are sampled throughout the simulation and used to define a fluctuating undisturbed flow field  $\mathbf{U}(\hat{\mathbf{x}}, t)$  on the multiphase DNS framework with a moving reference frame (MRF). By assuming the size of the bubble comparable to the Kolmogorov length scales, the fluctuating undisturbed flow field in the MRF can be approximated as  $\mathbf{U}(\hat{\mathbf{x}}, t) = \mathbf{u}_B^{EL}(t) + \nabla \mathbf{u}_B^{EL}(t)(\hat{\mathbf{x}} - \hat{\mathbf{r}}_B)$ . This approach is illustrated in Figure 3.3.

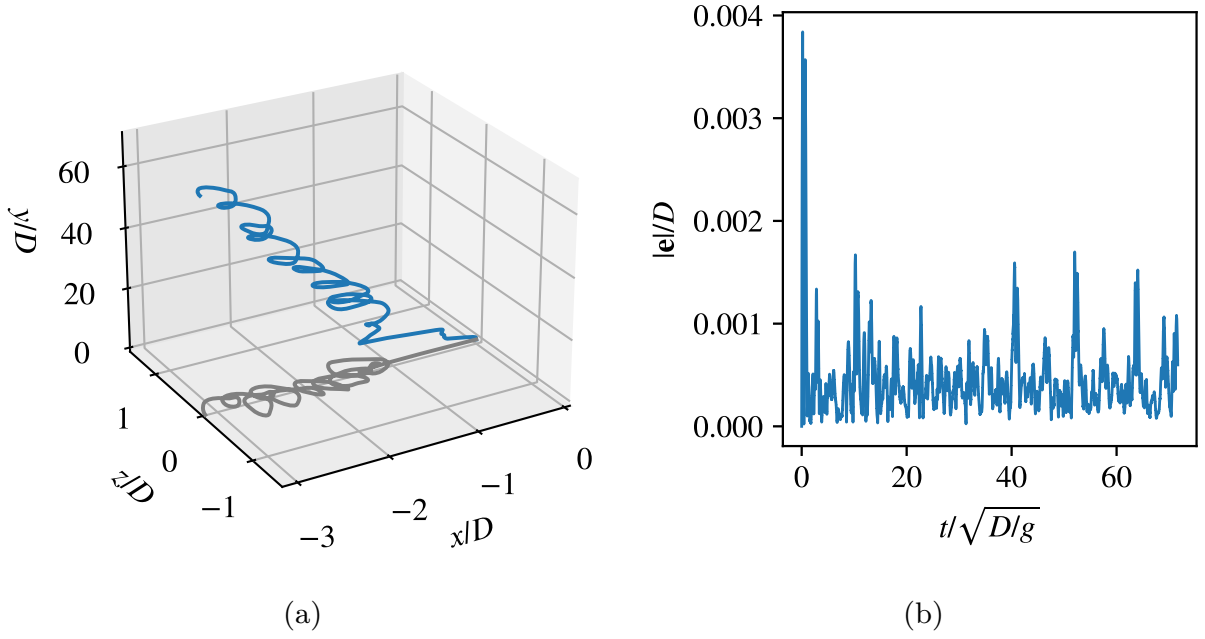


Figure 3.2: (a): Helical trajectory for a bubble with the governing parameters ( $Ga = 320$ ,  $Eu = 10$ ,  $Sr = 0.1$ ) rising in a linear shear flow with the shear in the  $xy$ -plane and gravity acting in the  $y$ -direction. This case is described in detail in Paper D. The blue line is the 3D trajectory in a laboratory reference frame, and the grey line is a projection onto the  $xz$ -plane. (b): Magnitude of the bubble displacement vector  $\mathbf{e}(t) = \hat{\mathbf{r}}_B(t) - \hat{\mathbf{r}}_B(t=0)$  showing that the bubble is kept within  $0.004D$  from its initial position in the MRF throughout the simulation despite the unsteady trajectory and a relatively long simulation time. This shows that the PID-controlled MRF achieves approximately  $\mathbf{a}_{mrf}(t) = \mathbf{a}_B(t)$  without introducing a drift of the bubble over time.

To impose the unsteady flow field in the MRF we introduce an additional acceleration term  $\mathbf{a}_U(\hat{\mathbf{x}}, t)$  (in the same term as  $\mathbf{a}_{mrf}(t)$  in Equation 3.10) as  $\mathbf{a}_U(\hat{\mathbf{x}}, t) = d\mathbf{U}/dt = d/dt(\mathbf{u}_B^{EL}) + d/dt(\nabla \mathbf{u}_B^{EL})(\hat{\mathbf{x}} - \hat{\mathbf{r}}_B)$ . We define  $\mathbf{a}_U^{n+1}(\hat{\mathbf{x}})$  as the spatially dependent but steady acceleration of the external flow field between a current time  $t^n$  and a later time  $t^{n+1}$  according to

$$\mathbf{a}_U^{n+1}(\hat{\mathbf{x}}) = \frac{\mathbf{U}^{n+1}(\hat{\mathbf{x}}) - \mathbf{U}^n(\hat{\mathbf{x}})}{\Delta t^{n+1}}, \quad (3.14)$$

where we use that  $\mathbf{U}$  is already known at  $t^{n+1}$  from the EL simulation. The linear variation of  $\mathbf{U}(\hat{\mathbf{x}}, t)$  gives the spatially dependent inlet Dirichlet velocity boundary conditions similar to Equation 3.13 on the MRF domain according to

$$\hat{\mathbf{u}}_{BC}^{n \rightarrow n+1}(\hat{\mathbf{x}}, t) = \mathbf{U}^n(\hat{\mathbf{x}}) + \mathbf{a}_U^{n+1}(\hat{\mathbf{x}})(t - t^n) - \mathbf{u}_{mrf}^n - \mathbf{a}_{mrf}^{n+1}(t - t^n), \quad (3.15)$$

and Neumann outlet velocity boundary conditions (that are not spatially dependent) on a boundary with the normal unit vector  $\hat{\mathbf{n}}$  as

$$\nabla \hat{\mathbf{u}}_{BC}^{n \rightarrow n+1}(t) \cdot \hat{\mathbf{n}} = \nabla (\mathbf{U}^n(\hat{\mathbf{x}}) + \mathbf{a}_U^{n+1}(\hat{\mathbf{x}})(t - t^n)) \cdot \hat{\mathbf{n}} \Rightarrow \quad (3.16)$$

$$\nabla \hat{\mathbf{u}}_{BC}^{n \rightarrow n+1}(t) \cdot \hat{\mathbf{n}} = \left( \nabla \mathbf{u}_B^{EL, n} + \frac{\nabla \mathbf{u}_B^{EL, n+1} - \nabla \mathbf{u}_B^{EL, n}}{\Delta t^{n+1}}(t - t^n) \right) \cdot \hat{\mathbf{n}}. \quad (3.17)$$

The imposition of the unsteady external flow field  $\mathbf{U}(\hat{\mathbf{x}}, t)$  allows us to study the detailed small-scale bubble dynamics in response to the turbulent liquid phase fluctuations predicted by the EL solver. In addition, the coupling provides a more realistic flow around the bubble in the MRF since bubbles preferentially move to regions of high vorticity in the turbulent liquid phase (due to the density difference of the phases and the local liquid phase pressure gradient). The Lagrangian bubble does, therefore, not in general experience the same statistical fluctuations as would be sampled in the EL solver by, for example, a fixed point or a heavy particle. The more realistic flow thus provides more realistic small-scale bubble dynamics and facilitates more accurate closures.

It should also be noted that the general formulation of the coupled framework makes it suitable to study the small-scale dynamics of any type of sub-Kolmogorov body, such as droplets or particles using any multiphase DNS technique to handle the two-phase flow (VOF, Front-tracking, level-set, lattice-Boltzmann, diffuse interface approach).

Still, the present framework can be improved by implementing a two-way coupling of the two fluid dynamics solvers. Then, the solvers would be run in parallel and the bubble trajectory predicted by the multiphase DNS framework is used directly in the EL solver (instead of modelling the bubble motion using an equation of motion similar to Equation 2.3). Such a two-way coupling would provide a more direct multiscale simulation technique (coupling the two lower boxes in Figure 2.1) for studying the small-scale dynamics of deformable bodies subjected to turbulent flows with large length scales.

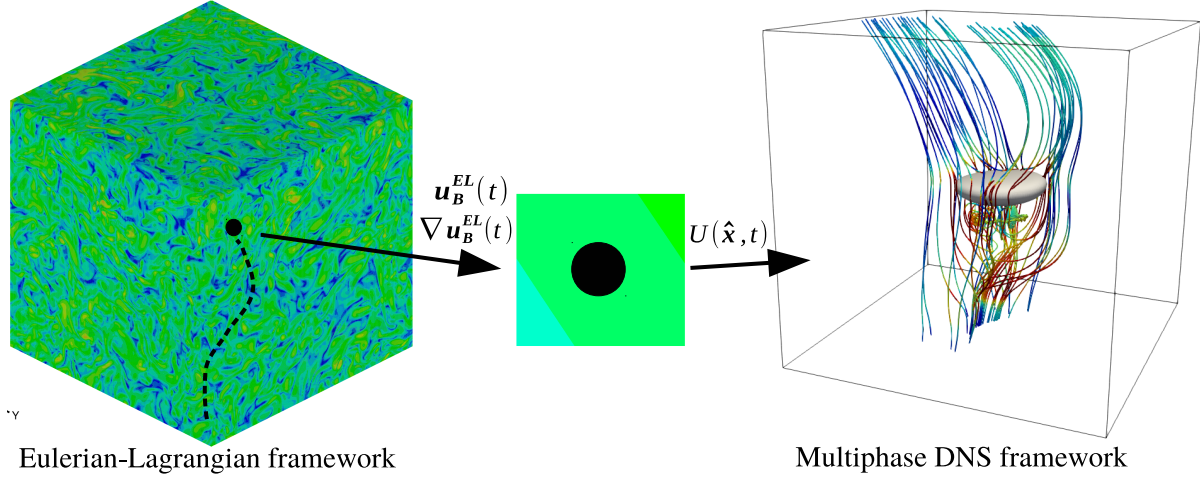


Figure 3.3: *Illustration of the coupled multiscale framework. Turbulent liquid fluctuations and shear rates experienced by a Lagrangian bubble are sampled in the EL simulation. These signals are used to determine the linearised unsteady flow field that is imposed in the multiphase DNS framework. The DNS thus predicts the detailed bubble dynamics in response to the turbulent liquid fluctuations. The colours represent the liquid-phase vorticity magnitude.*

### 3.3 Numerical frameworks for large-scale scalar dynamics in bubbly flows

In this section, we provide an overview of the last part of our work related to studying properties of bubbly flows across large scales. As discussed in Section 2.4, bubbly flows are an efficient means to enhance scalar transfer such as heat or chemical species (in, for example, bubble columns and heat exchangers) without the need for moving parts. This reduces the operating and maintenance costs [1]. The enhanced transfer is attributed to the mixing induced by the bubbles-induced turbulence. To design efficient processes, it is therefore crucial to predict the correct mixing characteristics induced by the bubbles.

The dynamics of scalars in bubbly flows have only recently received scientific attention in experimental [45, 46, 48, 62–64] and numerical [47, 65] works. These works have shown that the dynamics and statistics of the scalar transport are modified in bubble-induced turbulence compared to single-phase turbulence. However, the mechanisms behind the different characteristics and the influence of the governing parameters on the scalar dynamics are not yet entirely clear.

Multiphase DNS is a suitable tool for studying the dynamics and statistics of a passive scalar in bubbly flows since all relevant scales are resolved (down to the viscous dissipation scales), and reliable statistics can be readily extracted. In Paper E, we present such a numerical framework, and in the next section, we provide some additional details not included in Paper E.

### 3.3.1 Multiphase DNS framework for passive scalar transport in bubbly flows

The numerical framework is intended for studying the effects of monodisperse rising bubbles on the dynamics and statistics of a scalar field with an imposed constant gradient in a cubic and fully periodic domain.

We again use the VOF multiphase DNS approach implemented in the open-source code Basilisk (basilisk.fr) [61]. The scalar fields that we study have Schmidt-numbers  $Sc = \nu/D_{mol} = O(1)$  (where  $D_{mol}$  is the diffusivity of the scalar in the fluid) suggesting that the smallest scales of the scalar fluctuations are comparable to the smallest scales of the bubble-induced turbulence. This indicates that a fine resolution is required in the major part of the computational domain at a fully developed turbulence. The adaptive grid refinement technique in Basilisk is, therefore, not particularly efficient in these types of simulations. Instead, we use a constant and uniform grid (of  $(512)^3$  grid points in Paper E) and make use of the cell-centred Cartesian multigrid solver that accelerates the solution of the Helmholtz-Poisson type problems for the velocity components and Poisson equation for the pressure correction [66]. This allows us to perform high-resolution 3D simulations with a uniform grid at a feasible computational cost.

We use a cubic and fully periodic domain with gravity acting in the downward vertical direction. Because of the periodicity, an additional body force is needed to avoid the entire system from accelerating in the gravitational direction. This force is defined as  $-\langle\rho\rangle\mathbf{g}$  where  $\langle\rho\rangle$  is the volume average density of the bubble suspension. The force represents the hydrostatic pressure gradient that would be induced by a wall at the bottom of the domain [67]. The VOF approach uses a single-fluid formulation of the momentum equation valid for both phases that, in nondimensional form, becomes

$$\rho \frac{D\mathbf{u}}{Dt} = (\rho - \langle\rho\rangle)\mathbf{g} - \nabla p + \frac{1}{Ga} \nabla \cdot (\mu(\nabla\mathbf{u} + \nabla\mathbf{u}^T)) + \frac{\kappa\delta_S\hat{\mathbf{n}}}{Eo}. \quad (3.18)$$

The single-fluid formulation significantly simplifies the numerical solution of the governing equations. However, a drawback of the VOF method in the present study is that the coalescence of the bubbles is a grid-dependent process where the bubbles inherently coalesce when the distance between the bubble interfaces is smaller than the grid spacing. The coalescence process also involves the formation of thin liquid films between the interfaces that require very fine grid resolutions [44].

In the present study, we simplify the problem by focusing on the scalar dynamics in a monodisperse bubbly flow where coalescence is not allowed. This is a fair assumption in bubbly flows at low gas volume fractions where bubble collisions are relatively rare [68]. In addition, we are interested in the statistically steady-state properties of the bubbly flow that would be difficult to obtain if the bubble number and sizes change during the simulation.

To avoid coalescence, we implement a repulsive force between bubbles when they are in

close proximity to each other. The repulsive force is achieved by locally increasing the surface tension at the part of the bubble interfaces that is less than one bubble diameter  $D$  away from another bubble's centre of mass. Since the surface tension force acts normally to the interface and towards the bubble interior, the local increase of the surface tension induces a net force on the bubble in a direction away from the neighbouring bubble. The method is similar to the one described in [69] but with a different implementation method as described below. This approach effectively prevents coalescence in all our simulations without introducing excessive external forcing in the liquid between the bubbles that may affect the flow and scalar dynamics.

The implementation comprises (at each computational time step) the identification of each individual bubble, computing the bubble positions in the periodic domain, identifying interfacial cells that are within one  $D$  from another bubble's centre of mass and finally, increasing the surface tension in those cells. Each bubble is identified by using the tag functionality in Basilisk ([basilisk.fr/src/tag.h](http://basilisk.fr/src/tag.h)) that provides a unique integer value  $q \in [1, N_b]$  to all the cells in the field  $\mathcal{T}(x_i)$  that belong to the same discrete bubble. Computing the centre of mass for a bubble in a periodic domain requires additional considerations since the bubbles may partly cross one or more periodic boundaries at a given instant. This problem can be solved by transforming each spatial coordinate  $x_i \in [0, L)$  of the cubic domain (with the volume  $\Omega = L^3$ ) to angles on a circle according to [70]:

$$\theta_i = \frac{x_i}{L} 2\pi . \quad (3.19)$$

The centre of mass for a bubble  $q$  with a constant density is determined by first computing the volume averaged quantities

$$\xi_i^q = \frac{1}{\Omega_q} \int_{\Omega_q} \cos \theta_i d\Omega , \quad (3.20)$$

$$\zeta_i^q = \frac{1}{\Omega_q} \int_{\Omega_q} \sin \theta_i d\Omega , \quad (3.21)$$

where  $\Omega_q$  is the volume of the bubble  $q$  defined by the region satisfying  $\mathcal{T} = q$ . The average angles  $\theta_i^q$  for bubble  $q$  on the circles are then computed by

$$\theta_i^q = \text{atan2}(-\xi_i^q, -\zeta_i^q) + \pi , \quad (3.22)$$

and the corresponding centre of mass for the bubble is determined using Equation 3.19 as

$$x_i^q = \theta_i^q L / 2\pi , \quad (3.23)$$

that provides a consistent centre of mass for each bubble across the periodic domain boundaries.

We identify interfacial cells that are closer than one  $D$  away from another bubble's centre of mass by first defining the initial proximity field  $\mathcal{P}(x_i) = 0$  in  $\Omega$ . For each bubble  $q$ , we then add a positive value  $b$  to  $\mathcal{P}(S^q) += b$  inside the region  $S^q$  defined by a sphere centred at  $x_i^q$  and with radius  $D$ . To take the periodicity into account, the sphere centre

is shifted by  $-L$  and  $L$  in all spatial directions. The resulting proximity spheres enclose all the bubbles in our simulations (with the spherical-equivalent bubble radius  $D/2$ ), although the bubbles are typically non-spherical. All regions in  $\Omega$  where  $\mathcal{P} > b$  identify the regions where two or more proximity spheres overlap and  $b$  has been added more than once to  $\mathcal{P}$ .

To avoid coalescence, we locally increase the surface tension to  $\sigma_{rep} = 2.1\sigma$  in any part of the bubble interfaces where  $\mathcal{P} > b$ . This procedure ensures that repulsive forces act on the bubbles before they are close enough to coalesce. Figure 3.4 illustrates the implementation procedure and confirms that the method works also across periodic boundaries. It should be noted that the somewhat arbitrary model parameters (the radius  $D$  of  $S^q$  and  $\sigma_{rep}$ ) are found to give satisfactory results for the governing parameters used in Paper E (and Figure 3.4) of  $Ga = 390$ ,  $Eu = 0.85$  and volume fraction up to  $\phi = 5.2\%$  that correspond to 2.5 mm air bubbles in water. For other governing parameters or system setups, the model parameters may need tuning.

This numerical framework is a useful tool for studying the properties of bubbly flows at large scales by simulating representative volumes with about  $O(100)$  bubbles. Such studies can facilitate the development of improved closures for processes in bubbly flows up to industrial scales. In Paper E, we study the dynamics and statistics of a passive scalar in bubbly flows. Still, the framework could be used to study many other relevant processes, such as bubble-induced turbulence itself, other types of mass transfer or extended to study heat transport and reacting flows. Selected results from our studies using this framework are presented in Section 4.3.

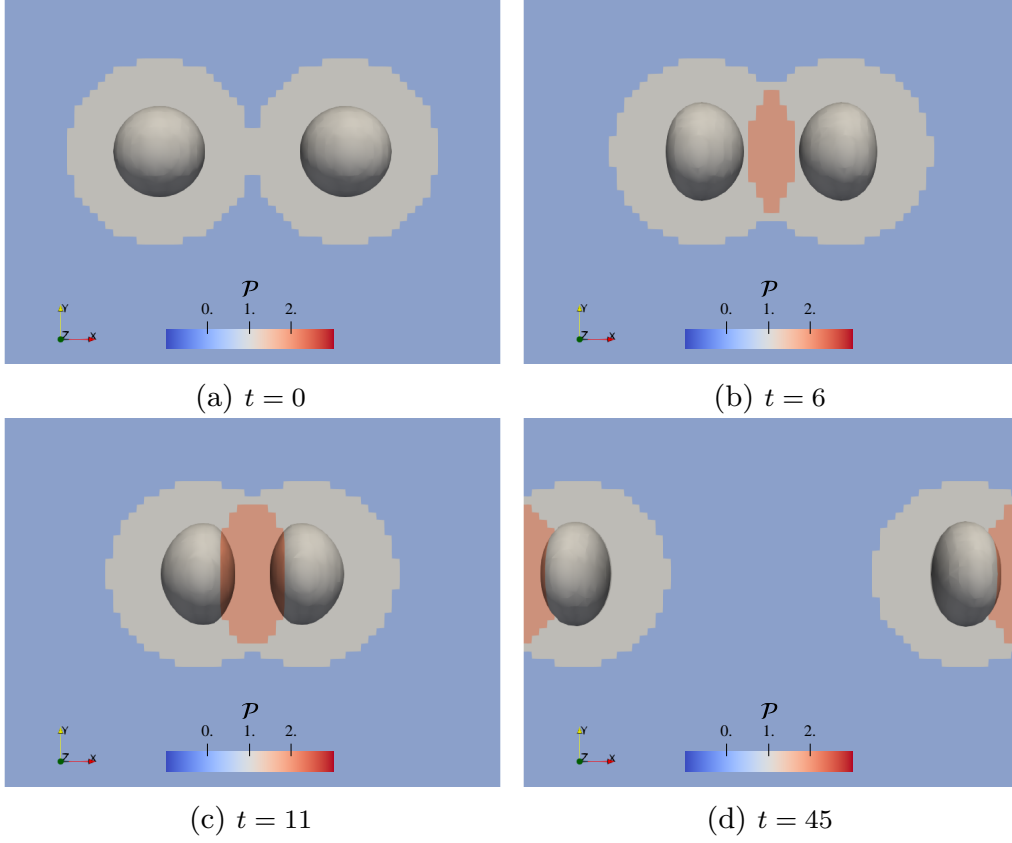


Figure 3.4: *Illustration of the repulsive force model used for preventing coalescence of bubbles in the DNS framework of Section 3.3.1. A proximity field  $\mathcal{P}$  is used to identify the regions in the domain where the force should be applied. For each bubble, a positive value  $b$  (equal to unity in this case) is added to  $\mathcal{P}$  in a sphere of radius  $D$  around the bubble centre of mass. In the regions where  $\mathcal{P} > b$ , the repulsive force is applied by increasing the surface tension at the part of the bubbles interfaces that occupy  $\mathcal{P} > b$ . Here, the bubbles are forced to collide at the relative velocity of  $V_{\text{rel}}/\sqrt{gD} \approx 2$  (at about the nondimensional time  $t/\sqrt{D/g} = 6$ ) that represents a strong collision in a bubbly flow where bubbles mainly rise in parallel with the characteristic velocity  $\sqrt{gD}$  due to buoyancy. At  $t = 11$ , part of the bubble interfaces occupy  $\mathcal{P} > b$ , and the surface tension is locally increased to  $\sigma_{\text{rep}}$  that induces a repulsive force on the bubble. Coalescence is prevented, and the bubbles bounce back to collide again at  $t = 45$  across the periodic boundary. This illustrates that the implementation also handles the periodicity correctly. Note that this illustration case is performed at a lower spatial resolution than in the DNS simulations of the bubble suspensions.*



## 4 Selected results and discussion

In this section, we show selected results from our studies using the above described numerical frameworks. The results illustrate the findings from our studies of specific bubbly flow phenomena and show the capabilities of the numerical frameworks. We further discuss the usefulness of the frameworks in a more general context.

### 4.1 Numerical investigations of laser-induced thermocavitation

The laser-induced cavities are increasingly studied as a part of a promising new technology to achieve good spatiotemporal control in the process of crystallisation [71]. Crystallisation has been observed in experiments around the laser-induced cavities in saturated solutions, but the mechanisms behind the crystallisation are not entirely clear [72–75]. One crystal nucleation hypothesis is that the evaporation of the solvent at the bubble interface produces a high solution supersaturation around the bubble [76]. The evaporation increases the concentration of solute in the solution around the bubble and, at the same time, cools the solution. These effects lead to an increase of the solution supersaturation, and with sufficient duration and degree of supersaturation, crystals may nucleate within the solution around the bubble. In general, the supersaturation level is dependent on the concentration of the dissolved solute and the saturation concentration at the solution temperature and pressure.

Because of the small spatiotemporal scales and fast dynamics of the cavitation event, it is very difficult to measure the degree of supersaturation experimentally. With fully resolved DNS simulations it is, however, possible to obtain such estimates.

In Paper B, our DNS framework is extended by considering the solute transport in the liquid around the vapour bubble and with an improved formulation of the interfacial energy transfer. In this study, we test if the crystal nucleation hypothesis about high supersaturation in the solution around the bubble is plausible by simulating a thermocavitation event with an experimentally observed crystallisation. In Figure 4.1, we show the temperature contours from three instants during this simulation. Here, a solution at  $293\text{ K}$  is placed between an upper and lower wall,  $50\text{ }\mu\text{m}$  apart, and with outlets to the sides. Initially, a  $2\text{ }\mu\text{m}$  vapour bubble is placed in the centre of the domain, and during the  $9\text{ ns}$  laser pulse, a cylinder of liquid with the radius  $10\text{ }\mu\text{m}$  is heated to almost  $500\text{ K}$ . The superheated liquid evaporates into the vapour bubble that rapidly expands between the walls and reaches a diameter of over  $130\text{ }\mu\text{m}$  in only  $6\text{ }\mu\text{s}$ . Figure 4.2 shows that the predicted bubble growth rates of the DNS simulation (2D axisymmetric) and the 1D framework are in fair agreement with the experimental measurements of Soare et al. [75]. A major difference in the 1D simulation is that the liquid is heated uniformly in a

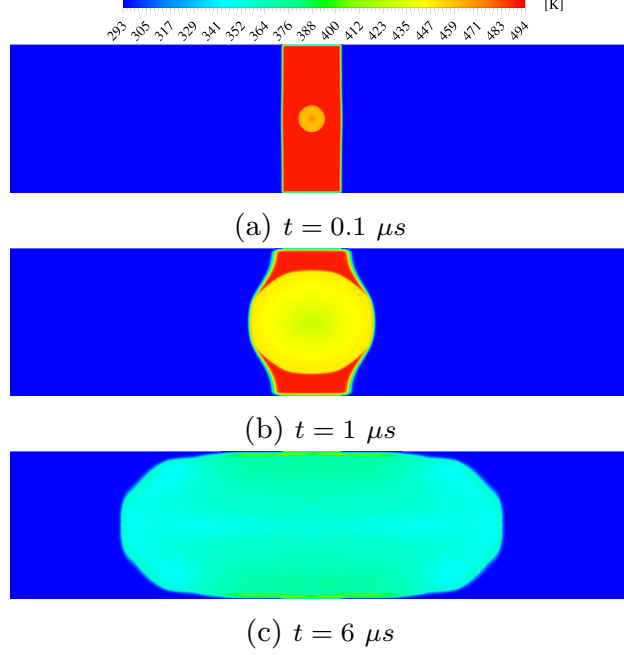


Figure 4.1: *Temperature contours at three instants from the 2D-axisymmetric DNS of a laser-induced thermocavitation bubble performed in Paper B. A 9 ns laser pulse superheats a cylinder of liquid with the radius  $10\ \mu\text{m}$  to almost  $500\ \text{K}$ . The superheated liquid evaporates into the vapour bubble that rapidly expands between the walls and reaches a diameter of over  $130\ \mu\text{m}$  in only  $6\ \mu\text{s}$ .*

sphere of radius  $10\ \mu\text{m}$  around the bubble rather than a cylinder, as in the DNS. The 1D setup also assumes an unbounded domain, while the 2D-axisymmetric setup is bounded by walls that significantly influence the bubble dynamics after an initially almost spherical growth period. The results do, therefore, not agree after the initial growth period. The fair agreement with the experiment does nonetheless indicate that the predicted evaporation rates are reasonable since they govern the bubble growth rates.

During the simulations, we extract the temperature and pressure of the liquid phase at the bubble interface and compute the evolution of the solute concentration in this liquid. These properties provide an estimate of the solution supersaturation in the liquid at the bubble interface. Figure 4.3 shows the evolution of the average interfacial properties during the first five microseconds of the DNS (2D) and the 1D framework. Both frameworks predict similar mass flux (evaporation) across the bubble interface, which implies that the flow conditions close to the interface are sufficiently resolved in both simulations. The interface average temperature of the liquid is, however, higher in the 2D simulation due to the larger volume of superheated liquid in the cylinder (2D) than in the sphere (1D) that influences the average interface cooling rate. The solute concentrations at the bubble interface are similar in both frameworks because the evaporation rates that govern the concentration evolution are similar. Consequently, similar supersaturation levels  $S_\sigma = c/c_{\text{sat}}(T_l) - 1$  are obtained in the liquid at the bubble interface, where  $c$  is the solute concentration, and  $c_{\text{sat}}(T_l)$  is the saturation concentration at the liquid interface temperature  $T_l$ . Both simulations show a significant peak of supersaturation ( $> 0.13$ ) that is

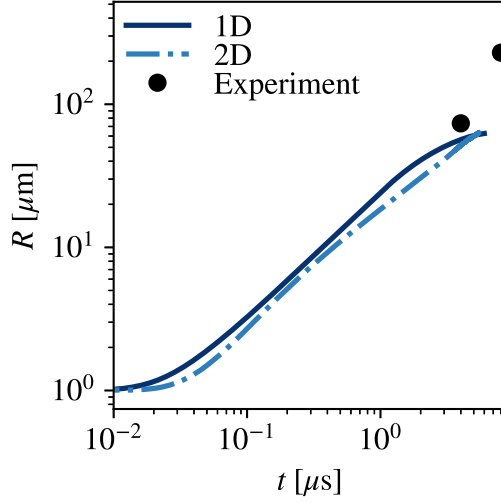


Figure 4.2: Comparison of the bubble radius evolution predicted by the 2D-axisymmetric DNS, the 1D framework and the experiments by Soare et al. [75] of a laser-induced thermocavitation bubble. The 1D simulation is performed in an unbounded domain and does therefore not predict the same growth rate as the experiment and corresponding 2D setup after an initially almost spherical growth period in both setups.

not possible to achieve in evaporative or cooling crystallisation under normal conditions [76]. These results thus indicate that the crystal nucleation hypothesis is plausible and deserves to be investigated further.

From experimental studies, it has been observed that crystallisation is only obtained under certain conditions and laser pulse parameters [72, 73]. If the high supersaturation in the solution around the bubble is indeed the mechanism behind the observed crystal nucleation, it raises questions about the conditions that are necessary for obtaining the high supersaturation.

To investigate these conditions, we first identify the important parameters that influence the supersaturation level and then investigate those parameters using numerical simulations. We reason in Paper B that it is the evaporation of the solvent that produces the increase of the solute concentration in the solution around the bubble. The laser pulse energy and the spatial distribution of that energy govern the rate and duration of the evaporation, and the diffusivity and solubility of the solute influence the solute concentration and supersaturation level in the solution. This gives us at least four important parameters to investigate under a range of relevant values.

In Paper B, we perform an extensive parameter study using the 1D numerical framework. The results indicate that the high supersaturation is only possible under specific ranges of the investigated parameters. This conclusion is in line with the aforementioned experimental observations, and the presented parameter studies can be used as guidelines for any user to find appropriate setups to reach conditions favourable for crystallisation.

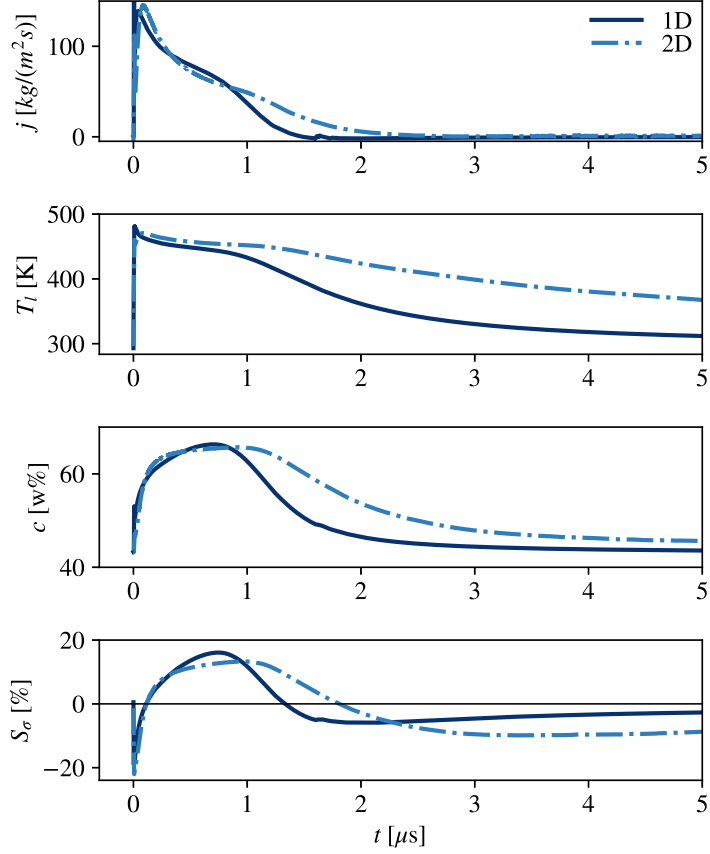


Figure 4.3: *Evolution of the average bubble interface properties predicted by the 1D and 2D DNS frameworks for a laser-induced thermocavitation bubble. The top panel shows the mass flux across the interface due to phase change. The second panel is the temperature of the liquid at the bubble interface, and the third panel shows the evolution of the solute concentration at the same position. The last panel shows the resulting supersaturation level of the solution at the bubble interface and predicts a significant peak during the first microsecond. Such high supersaturation is not possible using conventional crystallisation techniques under normal conditions and thus indicates that the proposed crystal nucleation hypothesis is indeed plausible.*

Our results show that the multiphase DNS framework and the 1D framework can capture the relevant phenomena in the extreme case of a laser-induced thermocavitation events although more validation is needed to assess the accuracy. The numerical frameworks are formulated in a general way and, therefore, constitute useful tools for studying many types of bubble evolution processes. The DNS framework can be used to study the detailed flow conditions in specific cases with one or more bubbles and possibly complex geometries while the 1D framework is suitable for extensive parameter investigations in simpler configurations.

## 4.2 Small-scale rising bubble dynamics

Here, we give a few example results and illustrations from our multiphase DNS framework with a PID-controlled non-inertial Moving Reference Frame (MRF). We start by illustrating the advantage of the PID-controlled MRF in combination with the adaptive grid refinement technique of Basilisk. We examine the simple case of a planar 2D bubble rising in a quiescent liquid with the governing parameters  $Ga = 100$  and  $Eu = 1$  that give a zigzagging bubble motion. In an absolute reference frame, a domain height of about  $160D$  would be needed to capture the last ten oscillation periods and obtain relatively steady velocity statistics. However, a domain of about  $(20D)^2$  is sufficient in the PID-controlled MRF technique since it keeps the bubble at its initial position in the MRF, and the simulation can be continued indefinitely (or until the statistics are sufficiently steady). This avoids the need for a priori determining a sufficient domain size to capture the dynamics.

In this case, a resolution of more than 50 cells/ $D$  is required for DNS [44] that would result in more than 64 million grid points in a domain of  $(160D)^2$  using a uniform grid. By using the adaptive grid technique in the MRF simulation, approximately 45 000 grid points suffice for DNS. This technique ensures high grid resolution in the regions with large variations of the volume fraction and velocity fields and lower resolution in more uniform regions. Here, an absolute error tolerance for the velocity field is specified as  $\eta_u = 0.003$ , and  $\eta_f = 0.01$  is selected for the volume fraction field [44]. An illustration of the adaptive grid refinement levels and the resulting computational grid are shown in Figure 4.4 for the MRF simulation. The computational cell size is always divided by a factor of 2 for each refinement level.

In Figure 4.5, we show a similar example from a 3D DNS with the PID-controlled MRF and the adaptive grid technique. The governing parameters are  $Ga = 320$  and  $Eu = 10$ , and the bubble is rising in a linear shear flow with the nondimensional shear rate  $Sr = \omega_\infty D / (\sqrt{gD}) = -0.5$  in the  $xy$ -plane. Because of the high shear, the bubble moves almost  $150D$  in the vertical direction in the first  $t / (\sqrt{D/g}) = 50$  time units. With the MRF, a domain of  $(25D)^3$  is sufficient for any time period. Here, we use a base grid size of approximately 2.5 cells/ $D$  and a maximum grid resolution of 164 cells/ $D$ . As illustrated in Figure 4.5, the highest grid resolution is only used close to the bubble and

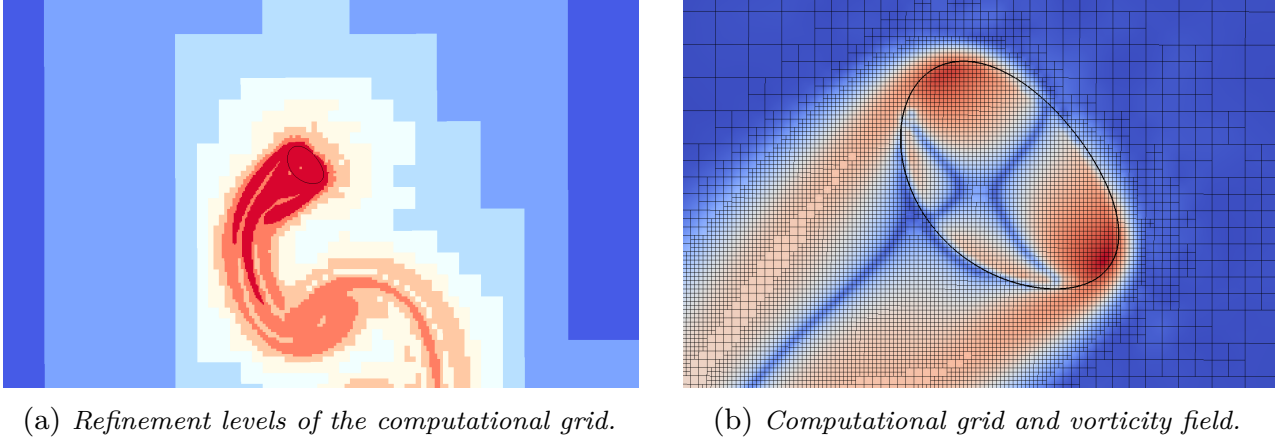


Figure 4.4: *Illustration of the computational grid using the adaptive grid refinement technique in a 2D multiphase DNS with the MRF of a zigzagging bubble. The thick black lines indicate the bubble interface. The governing parameters are  $Ga = 100$  and  $Eo = 1$ . (a): Refinement levels used in the computational grid where warmer colours represent higher grid refinement levels. Dark red represents the maximum level of 50 cells/D, and dark blue the minimum level of 0.4 cells/D. (b): The computational grid close to the bubble where the colours represent the logarithmic absolute value of the vorticity. Panel (b) illustrates that the velocity gradients are well resolved in the entire flow field using the adaptive grid technique.*

in the bubble wake. With the MRF, the length of the resolved wake can be selected by adjusting the domain size and the bubble position within the MRF. The MRF approach therefore avoids resolving unnecessarily long wakes.

Another advantage of the MRF technique is that it is straightforward to compute and study time-averaged fields induced by the bubble since the bubble position is fixed. This is illustrated in Figure 4.5b with the time-average streamwise vorticity field  $\overline{\omega_y}$ . The time-averaged field shows that the periodic wake of Figure 4.5a on average produces a pair of counter-rotating vortices in the bubble wake. These vortices induce a lift force in the negative  $x$ -direction (according to the theoretical framework of Paper D) and can explain the average bubble motion in that direction.

Next, we show selected results from the coupling of the MRF framework with the EL-solver to study bubble dynamics in turbulent flows.

#### 4.2.1 Dynamics of individual bubbles in turbulent flows

In this section, we present an example study of individual sub-Kolmogorov bubbles rising in a turbulent flow. The simulations are performed with the coupled Eulerian-Lagrangian and DNS solver with the MRF technique outlined in Section 3.2.2 and described in detail in Paper C. The simulation setup is described in Sections 3.1 and 3.5 of Paper C where a bubble rises in a homogeneous isotropic turbulent flow with the Kolmogorov length scale comparable to the bubble diameter and a Taylor Reynolds number of  $Re_\lambda = 180$ .

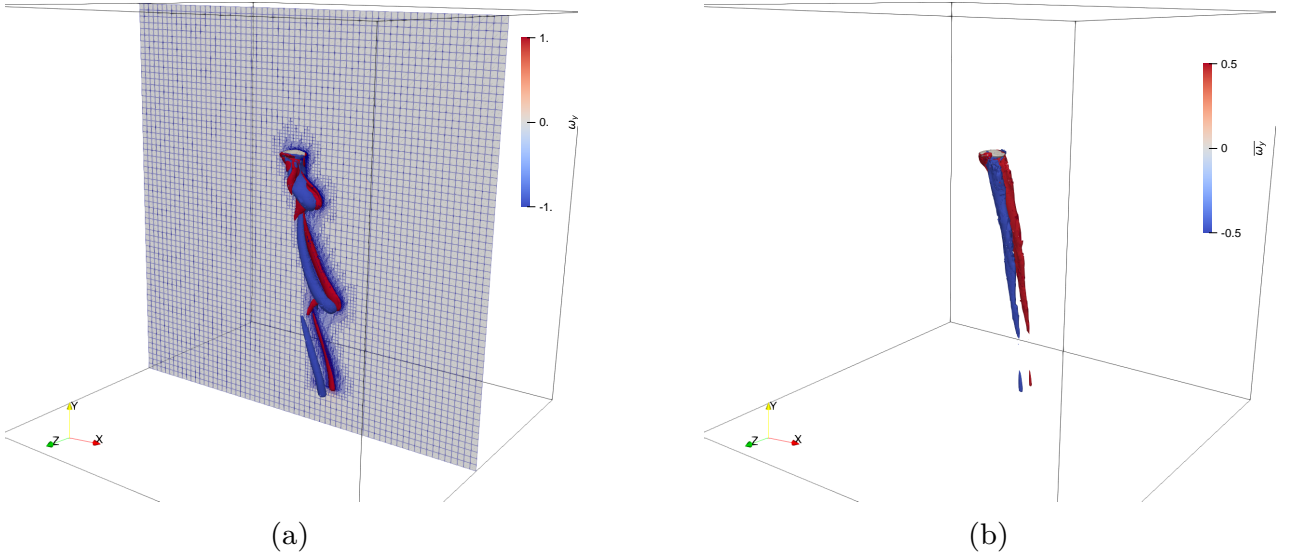


Figure 4.5: (a): Snapshot from the 3D DNS with the MRF technique of a bubble rising in a linear shear flow. The governing parameters are  $Ga = 320$ ,  $Eo = 10$  and the nondimensional shear rate  $Sr = -0.5$  in the  $xy$ -plane. The iso-surfaces represent the streamwise vorticity  $\omega_y$  generated by the bubble motion, and the cross-section illustrates the adaptive grid. (b): Iso-surfaces of the time-averaged  $\overline{\omega_y}$ -field in the same simulation and instant as (a). The time-averaged field is straightforward to compute since the MRF technique keeps the bubble fixed in the domain.

Unlike in Paper C, we illustrate here the potential of the coupled numerical frameworks by showing the influence of the  $Eo$ -number on the small-scale bubble dynamics.

In the EL-solver, we use a cubic and fully periodic domain and track the rising bubble for  $t/\tau_\eta = 4$  where  $\tau_\eta = (\nu/\varepsilon)^{1/2}$  is the Kolmogorov time scale. This allows us to assess the influence of the smallest turbulent scales on the bubble dynamics. We test the values  $Eo = (10, 30, 50, 120)$  at a fixed  $Ga = 65$  that corresponds to a 0.76 mm air bubble in water but with a reduced surface tension. In the DNS solver with the MRF, we use a domain size of  $(10D)^3$  with the bubble fixed in the centre and a maximum grid resolution of more than 50 cells/ $D$ .

Characteristic bubble shapes for each  $Eo$ -number are shown in Figure 4.6. Three different shape regimes are obtained with an approximately an oblate spheroid at  $Eo = 10$ , spherical caps at  $Eo = 30$  and  $Eo = 50$ , and peripheral breakup at  $Eo = 120$ . Because of the breakup, we do not include quantitative values for the  $Eo = 120$  case. The different shapes induce different small-scale bubble dynamics as illustrated in Figure 4.7 that shows the bubble trajectories predicted by the DNS solver. Here, it is clear that the bubble motion is influenced by both the turbulent flow and the small-scale bubble dynamics. The imposed turbulent flow causes significant bubble motion in the horizontal  $x$ - and  $z$ -directions, and the different  $Eo$ -numbers give different rising motions. The case  $Eo = 10$  is approximately an oblate spheroid with a lower  $C_D$  and higher rise velocity than the spherical cap bubbles. While the latter cases ( $Eo = 30$  and  $Eo = 50$ ) show similar trajectories and bubble shapes, the case  $Eo = 30$  is spiralling, and the case  $Eo = 50$

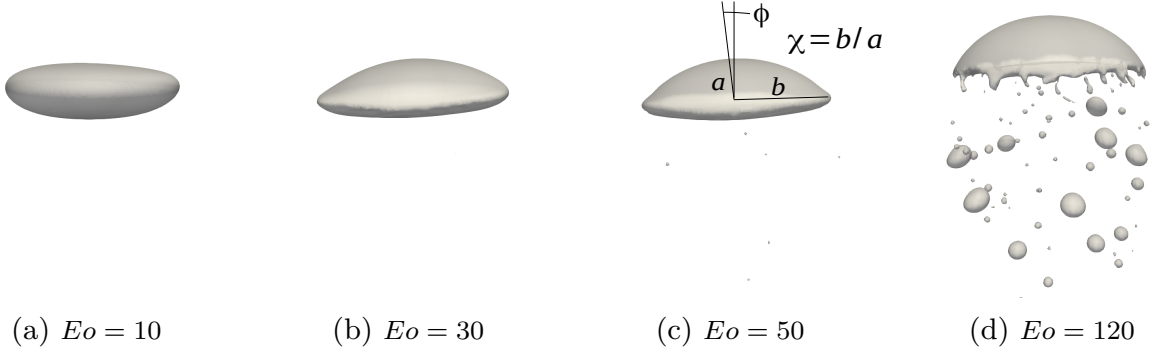


Figure 4.6: *Typical bubble shapes in cases of a bubble rising in homogeneous isotropic turbulence. The bubbles rise in the same turbulent field but with increasing  $Eo$ -numbers that give lower surface tension forces. The bubbles are increasingly deformed at higher  $Eo$ , and at  $Eo = 120$ , there is a peripheral breakup. Panel (c) illustrates the definitions of the bubble aspect ratio  $\chi = b/a$ , that is, the ratio of the major  $b$  to minor  $a$  semi-axes of the bubble and  $\phi$  is the orientation angle between the minor axis and the vertical axis.*

is not.

To quantify the observed differences, we compute the bubble aspect ratio  $\chi$  and orientation angle  $\phi$  (illustrated in Figure 4.6c), the relative velocity magnitude  $|\mathbf{V}_{rel}|$  between the bubble and the imposed turbulent flow and the instantaneous drag force coefficient  $C_D$ . These properties are shown in Figure 4.8, where the top panel illustrates the magnitude of the imposed turbulent velocity fluctuations. The case  $Eo = 30$  shows the highest bubble aspect ratio and the largest orientation angle due to the spiralling motion, while the case  $Eo = 50$  has a lower aspect ratio but a similar orientation angle as  $Eo = 10$ . Interestingly, despite the different aspect ratios and trajectories, the cases  $Eo = 30$  and  $Eo = 50$  obtain almost the same average relative velocity that is significantly lower than for  $Eo = 10$ . This is because the drag force coefficient  $C_D$  is higher for the two former cases (spherical caps) than the latter (oblate spheroid), as shown in the last panel of Figure 4.8.

We can also assess how the instantaneous  $C_D$  is influenced by the turbulent flow by performing a time-lagged cross correlation between the  $|\mathbf{u}_B^{EL}|(t)$  and  $C_D(t)$ . Here, we obtain a peak Pearson's correlation coefficient when  $C_D$  lags  $t/\tau_\eta \approx 0.5$  for all cases ( $C_D(t)$  is shifted back  $t/\tau_\eta \approx 0.5$ ). With this lag, the correlation coefficient is approximately 0.7 for the cases  $Eo = 10$  and  $Eo = 50$ , and 0.3 for  $Eo = 30$ . The lower correlation for the latter case is most probably due to the spiralling motion that influences  $C_D$ . Nonetheless, the obtained correlation coefficients show that  $C_D$  is correlated with the imposed turbulent velocity field but with a response time of  $t/\tau_\eta \approx 0.5$ . This response time indicates that the response dynamics occur at time scales below the Kolmogorov scales.

This example study illustrates the ability of the proposed multiscale framework to resolve both the bubble deformations induced by turbulent fluctuations and the small-scale bub-

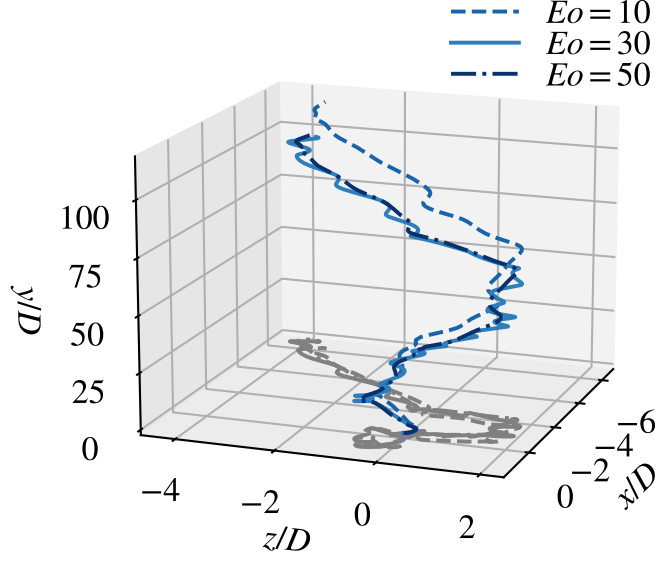


Figure 4.7: *Absolute trajectories of bubbles rising in homogeneous isotropic turbulence. The trajectories are predicted by the DNS framework with the imposed liquid-phase fluctuations given by the EL-solver. The same fluctuations are imposed in all three cases, but the various  $Eo$  numbers give different small-scale bubble dynamics and trajectories.*

ble dynamics associated with spatiotemporal scales below the Kolmogorov scales. The presented results represent only a few relevant small-scale bubble phenomena and many other phenomena, such as bubble breakup, dispersion and interfacial forces discussed in Section 2.3 and Section 2.4 could be investigated as well. Such studies can elucidate the effects of the turbulent flow on the small-scale bubble dynamics and facilitate the development of improved small-scale models.

Next, we use the DNS solver with the MRF technique to study the specific phenomena of the lift force acting on single bubbles rising in shear flows.

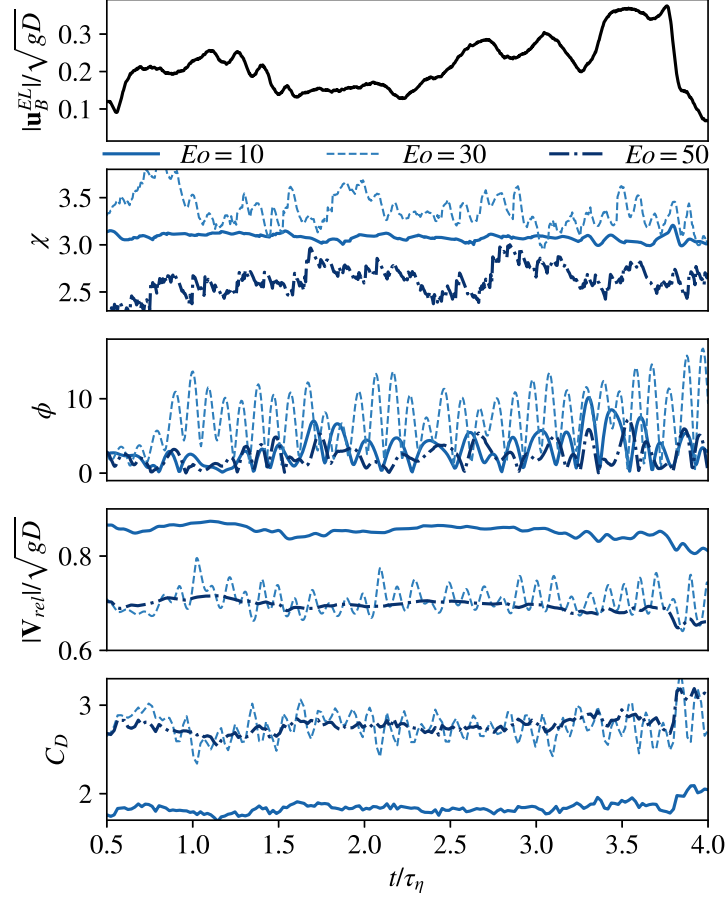


Figure 4.8: (top panel): Magnitude of the imposed turbulent liquid velocity fluctuations. (second panel): bubble aspect ratio  $\chi$ . (third panel): bubble orientation angle  $\phi$  from the vertical axis. (forth panel): Relative velocity magnitude experienced by the bubbles in the DNS. (fifth panel): Drag force coefficient predicted in the DNS. The legend below the first panel applies to all four bottom panels.

## 4.2.2 Shear-induced lift force acting on deformable bubbles

In this section, we present a number of example results and our main findings from Paper D where we study the mechanisms behind the shear-induced lift for acting on deformable bubbles rising in linear shear flows. The relevant governing parameters for this problem are the  $Ga$  and  $Eo$ -numbers together with the nondimensional shear rate  $Sr$ .

Based on previous studies, four distinct mechanisms are identified that induce a lift force on bubbles in linear shear flows. The lift force acting on spherical bubbles (low  $Eo$ ) in inviscid flows (high  $Ga$ ) is dominated by the Lighthill-, or L-mechanism [77]. This mechanism is a consequence of a pair of counter-rotating streamwise vortices in the bubble wake that induce a positive lift force (towards the pipe wall in upward pipe flows). Spherical bubbles in low-Reynolds-number (low  $Ga$ ) shear flows experience a positive lift force due to the Saffman-mechanism that is a consequence of the vorticity generated at the bubble surface [78]. Non-spherical bubbles (high  $Eo$ ) in low-Reynolds-number shear flows are instead dominated by the A-mechanism that induces a negative lift force (bubbles migrate towards the pipe centre in upward pipe flows) [79]. Finally, the lift force acting on deformed bubbles at higher Reynolds numbers (high  $Ga$ ) is dominated by the S-mechanism that is also a consequence of a pair of counter-rotating streamwise vortices in the bubble wake but with the opposite signs of the L-mechanism [30]. The S-mechanism, therefore, induces a lift force in the negative direction.

Because of the apparent connection with the vorticity dynamics, we aim for a comprehensive explanation of all four mechanisms in terms of the bubble-induced vorticity. We provide in Paper D a derivation for the expression

$$\mathbf{D} = -\frac{d}{dt} \left( \frac{1}{2} \rho_l \int_{\Omega_l + \Omega_g} \hat{\mathbf{x}} \times \tilde{\boldsymbol{\omega}} d\Omega \right) + \rho_l \Omega_g \frac{d\mathbf{V}_{rel}}{dt}, \quad (4.1)$$

that relates the bubble-induced vorticity field  $\tilde{\boldsymbol{\omega}}$  in a reference frame  $\hat{\mathbf{x}}$  following the bubble to the force  $\mathbf{D}$  acting on the bubble by the disturbed liquid.

We consider the case of an undisturbed linear shear flow  $U_y = -x\omega_\infty$  and gravity acting in the negative  $y$ -direction. A bubble rises due to buoyancy in the opposite gravitational direction, and, because of the shear flow in the  $xy$ -plane, a lift force acts on the bubble mainly in the  $x$ -direction. The total force  $D_x$  acting on the bubble by the liquid in the  $x$ -direction can, according to Equation 4.1, be divided into:

$$D_x = D_{x,\omega_z} + D_{x,\omega_y} = 0, \quad (4.2)$$

$$D_{x,\omega_z} = -\frac{d}{dt} \left( \frac{1}{2} \rho_l \int_{\Omega_l + \Omega_g} \tilde{\omega}_z \hat{y} d\Omega \right), \quad (4.3)$$

$$D_{x,\omega_y} = \frac{d}{dt} \left( \frac{1}{2} \rho_l \int_{\Omega_l + \Omega_g} \tilde{\omega}_y \hat{z} d\Omega \right), \quad (4.4)$$

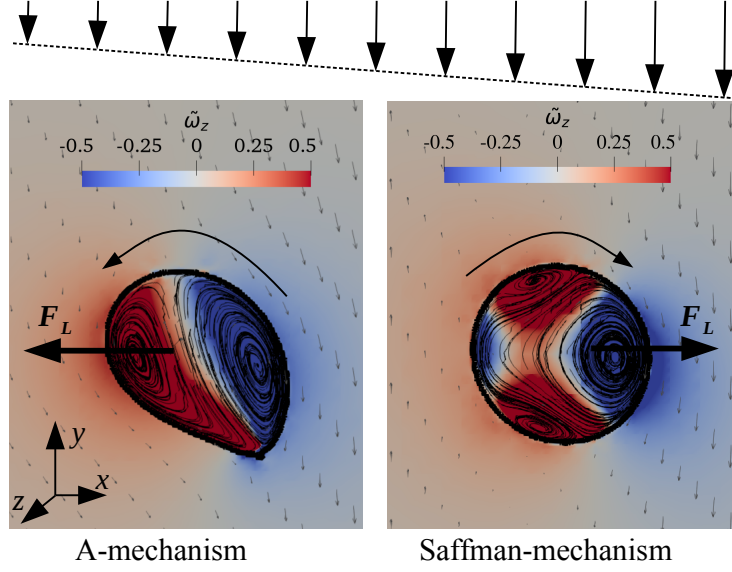


Figure 4.9: *Illustration of the A- and Saffman-mechanisms behind the lift force on a bubble rising in a linear shear flow. The contours represent the disturbance vorticity field  $\tilde{\omega}_z$  at a cross-section of the flow in the  $xy$ -plane, the arrows are the liquid velocity vectors, and the streamlines inside the bubble illustrate the gas recirculation zones. The Saffman-dominated case ( $Ga = 3.18, Eo = 0.4, Sr = 0.5$ ) is a spherical bubble that generates a net negative amount of  $\tilde{\omega}_z$  in the bubble near vortical system. The case ( $Ga = 3.18, Eo = 20, Sr = 0.1$ ) is dominated by the A-mechanism and instead generates a net positive amount of  $\tilde{\omega}_z$ . At this cross-section, these  $\tilde{\omega}_z$ -fields correspond to fluid circulations of opposite sign.*

at a steady bubble motion ( $dV_{rel,x}/dt = 0$ ). The shear-induced lift force must thus induce either a non-zero rate of change of the  $\hat{y}$ -moment of  $\tilde{\omega}_z$  or the  $\hat{z}$ -moment of  $\tilde{\omega}_y$ . Using theoretical analysis supported by our multiphase DNS with the MRF technique, we illustrate in Paper D how the four lift force mechanisms are related to the  $D_{x,\omega_z}$  and  $D_{x,\omega_y}$  terms.

In viscous flows (low  $Ga$ ), the lift force is governed by the term  $D_{x,\omega_z}$  of Equation 4.3 and the  $\tilde{\omega}_z$ -field generated at the bubble surface. Figure 4.9 shows the  $\tilde{\omega}_z$ -field at a steady state in the  $xy$ -plane of the bubble for (right panel) a spherical bubble (low  $Eo$ ) and (left panel) a bubble deformed by the shear flow (high  $Eo$  and relatively low surface tension). The spherical bubble induces a  $\tilde{\omega}_z$ -field with a net negative amount of  $\tilde{\omega}_z$  in the bubble near vortical system. As described in Section 5.3 of Paper D, Equation 4.3 predicts that such fields give a positive lift force, in accordance with the Saffman-mechanism. The shear-deformed bubble at high  $Eo$  instead generates a net positive amount of  $\tilde{\omega}_z$  in the bubble near vortical system. This field induces a negative lift force related to the A-mechanism.

In weakly viscous flows (high  $Ga$ ), it is the bubble-induced streamwise  $\tilde{\omega}_y$  vorticity that governs the lift force by the term  $D_{x,\omega_y}$  of Equation 4.4. Figure 4.10 shows streamwise vorticity iso-surfaces and cross-section contours in the wake of (right panel) a spherical bubble (low  $Eo$ ) and (left panel) an approximately oblate spheroid (high  $Eo$ ). Here, the

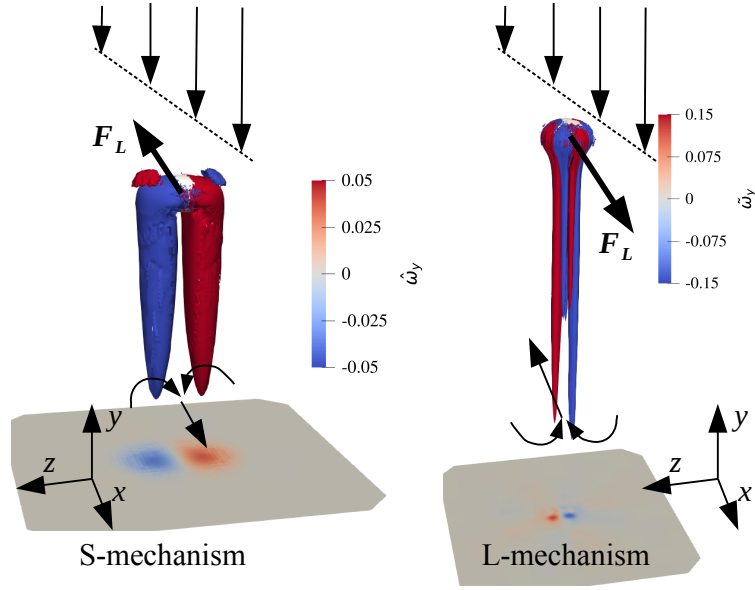


Figure 4.10: *Illustration of the S- and L-mechanisms behind the lift force on a bubble rising in a linear shear flow. Iso-surfaces of the streamwise vorticity  $\tilde{\omega}_z$  are shown in the bubble wakes, and contours of  $\tilde{\omega}_y$  are shown in the cross-sectional plane below the bubble. The S-mechanism case ( $Ga = 60, Eo = 5, Sr = 0.1$ ) generates a pair of counter-rotating streamwise vortices that induce a liquid flow in the positive  $x$ -direction and consequently generate a lift force in the opposite direction. The L-mechanism case ( $Ga = 240, Eo = 0.1, Sr = 0.05$ ) induces a pair of counter-rotating streamwise vortices with the opposite signs as the S-mechanism and thus generates a lift force in the positive  $x$ -direction.*

bubbles generate a pair of counter-rotating vortices in their wakes with the opposite signs in the two cases. The streamwise vortices induce a liquid flow in the  $x$ -direction that pushes the bubbles in the opposite direction due to Newton's third law. As described in [30] and Section 5.4 in Paper D, the L-mechanism generates streamwise vorticity by stretching and tilting the upstream vorticity of the shear flow with the signs corresponding to the right panel of Figure 4.10. Conversely, the S-mechanism generates the streamwise vorticity by stretching and tilting the vorticity generated at the bubble surface with the signs corresponding to the left panel of Figure 4.10. The surface vorticity generation increases with the bubble curvature and therefore the S-mechanism dominates the net amount of streamwise vorticity at a sufficient bubble deformation (higher interface curvature). Equation 4.4 shows that (discussed in Section 5.4 of Paper D) the opposite signs of the streamwise vorticity indeed give a lift force in the opposite  $x$ -directions in accordance with the L- and S-mechanisms.

Based on the above explanation for the four lift force mechanisms, it is not surprising that the net lift force acting on a bubble is a complex function of the governing parameters  $Ga$  and  $Eo$ . The lift force is most commonly modelled as in Equation 2.3 of this thesis [80]:

$$\mathbf{F}_L = -C_L \Omega_g \rho_l \mathbf{V}_{rel} \times \boldsymbol{\omega}_U, \quad (4.5)$$

where  $C_L$  is the lift force coefficient,  $\Omega_g$  is the bubble volume,  $\rho_l$  is the liquid density,

$\mathbf{V}_{rel} = \mathbf{V} - \mathbf{U}$  is the bubble relative velocity and  $\omega_U = \nabla \times \mathbf{U}$  is the undisturbed liquid-phase vorticity. This model formulation is appropriate for almost spherical bubbles at moderate to high  $Ga$  where the L-mechanism dominates. The lift force coefficient  $C_L$  thus need to account for any influence of non-spherical bubble shapes and viscous effects on the lift force.

Figure 4.11a shows the  $C_L$  values (dots) obtained using Equation 4.5 in our simulations and in experimental [81–83] and numerical [84, 85] studies in a wide range of the relevant  $Ga - Eo$  phase space. The contours represent a surface fitted to the points (described in Paper D) and to the analytical solution of  $C_{L,s,\infty} = 0.5$  [32] valid for a spherical bubble (low  $Eo$ ) in a weakly-sheared inviscid (high  $Ga$ ) flow. Here, the  $C_L$  contours show relatively small variations in the ranges of approximately  $Eo < 1$  and  $Ga > 10$  that indicate that the L-mechanism dominates the net lift force. However, outside these ranges,  $C_L$  varies significantly because of the other lift force mechanisms.

Figure 4.11 shows the approximate regions of the phase space  $Ga - Eo$  where the four mechanisms dominate the net lift force. These regions correspond both to the physical explanations behind the four mechanisms described above and to the observed values for  $C_L$  in experimental and numerical studies. These results thus provide a qualitative and comprehensive explanation for the behaviour of the lift force in the relevant ranges of the governing parameters  $Ga$  and  $Eo$ . In Paper D, we also present an extensive investigation on the role of the shear rate  $Sr$  on  $C_L$  and show that  $Sr$  may significantly influence  $C_L$  in the cases governed by the Saffman-, A- and S-mechanisms.

In summary, our theoretical framework provides a comprehensive explanation for the four mechanisms and makes it possible to estimate the induced lift forces in terms of moments of the bubble-induced vorticity. Our theoretical and numerical results qualitatively explain how the different mechanisms influence the lift force in a wide range of the relevant governing parameters. The study also shows how the lift force scales with the shear rate in regions of the phase space governed by the different mechanisms. The findings motivate further studies on determining the relative importance of the different lift force mechanisms under relevant flow conditions. Such studies and the results presented in Paper D can be used to develop improved lift force models that take all the mechanisms into account, including their complex dependence on the shear rate  $Sr$ .

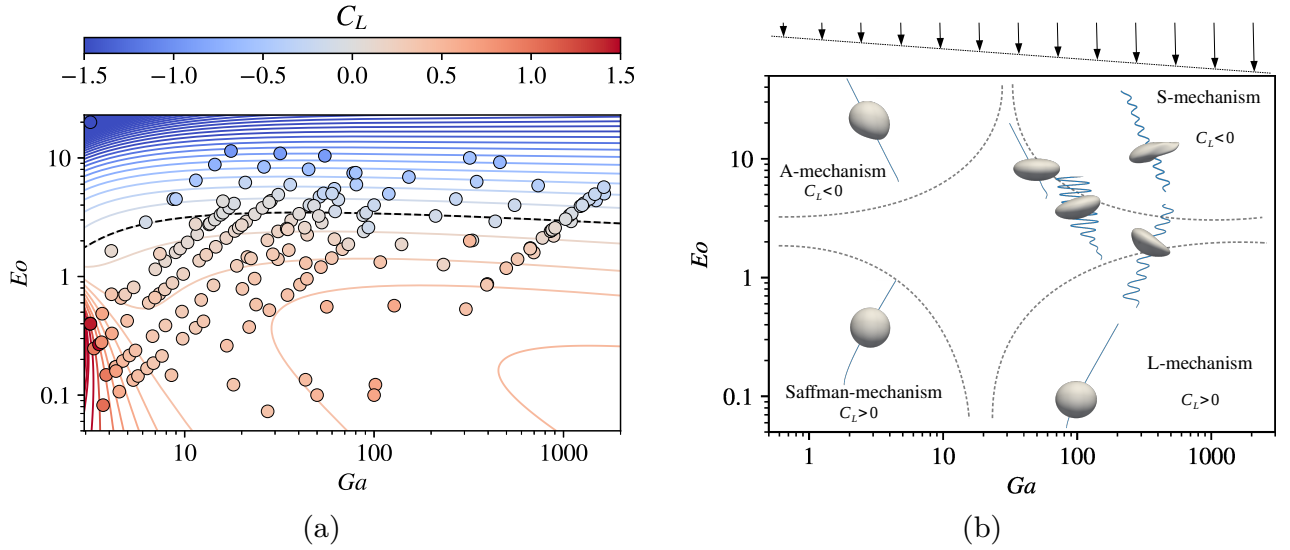


Figure 4.11: (a):  $(Ga, Eo)$ -phase plot with the  $C_L$  values (dots) obtained from experimental and numerical studies with moderate to high  $Sr$ . The contours illustrate a surface fitted to these points and the analytical solution of  $C_L = 0.5$  at high  $Ga$  and low  $Eo$ . The colour scale of the data points and contours is limited to the range  $[-1.5, 1.5]$  for visualisation purposes. The dashed black line indicates the contour line  $C_{L,fit} = 0$ . (b):  $(Ga, Eo)$ -phase plot illustrating the different behaviours of the lift force. The dashed lines represent qualitative indications of the regions where the four lift force mechanisms dominate the net lift force. Typical bubble shapes and trajectories (blue lines behind the bubbles) are shown for the case where the liquid velocity relative to the bubble is higher on the right side of the bubble (representation of the relative velocity field above the plot). The bubble positions in the phase plot indicate the parameters used in their respective simulations. The bubble trajectories are scaled to more clearly show the direction of the lateral motion. Note also that in some regions,  $Sr$  influences which mechanism dominates the net lift force and this dependence is investigated in Paper D.

### 4.3 Passive scalar transport in large-scale bubbly flows

Here, we present our main findings and example results from Paper E using the numerical framework outlined in Section 3.3.1. We study the dynamics and statistics of a passive scalar field with an imposed mean constant gradient in a monodisperse bubbly flow solved in a cubic and fully periodic domain.

We use  $O(10)$  to  $O(100)$  bubbles ( $N_b$ ) to get statistics not significantly dependent of their number [47]. The statistics are extracted by averaging over the domain volume and simulation time after an initial transient period. For this statistically stationary and homogeneous system, the time and volume averaging are identical to ensemble averaging (represented here by  $\langle \rangle$ ) due to ergodicity. The extracted statistics thus represent properties of the bubbly flow across large scales.

The scalar field is decomposed in  $c = \nabla \langle c \rangle \cdot \mathbf{x} + c'$ , where  $\langle c \rangle$  is the imposed mean linear scalar field with a constant gradient, and  $c'$  is the scalar disturbance due to the bubble agitation. We impose the constant mean scalar gradient in either the vertical ( $\nabla \langle c \rangle^v = 1$ ) or horizontal direction ( $\nabla \langle c \rangle^h = 1$ ) of the computational domain to assess the influence of the gradient direction on the scalar statistics. The scalar fluctuation transport equation that we solve numerically reads

$$\frac{\partial c'}{\partial t} + \mathbf{u} \cdot \nabla c' = \nabla \cdot (D_{mol} \nabla c') + \nabla D_{mol} \cdot \nabla \langle c \rangle - \mathbf{u} \cdot \nabla \langle c \rangle, \quad (4.6)$$

where  $D_{mol}$  is the molecular diffusivity of the scalar in the fluid.

The governing parameters  $Ga = 390$  and  $Eu = 0.85$  are used for all simulations and correspond to 2.5 mm air bubbles in water. We study the gas volume fractions  $\phi = 1.7\%$  and 5.2% and liquid-phase Schmidt numbers  $Sc_l = \nu_l / D_{mol,l} = (0.7, 1.5, 3, 7)$ , where  $\nu_l$  is the kinematic viscosity of the liquid and  $D_{mol,l}$  is the molecular diffusivity of the scalar in the liquid. The gas Schmidt number is  $Sc_g = \nu_g / D_{mol,g} = 0.7$  for all cases except for the cases shown in grey colour in Figure 4.15 where  $Sc_g = 7$ .

Figure 4.12 shows snapshots from the simulation of  $\phi = 5.2\%$  and  $Sc_l = 7$  for an imposed mean gradient in the horizontal (Figure 4.12a) and vertical (Figure 4.12b) directions. Here, the colours represent the total scalar field  $c$  and warmer (red) colours indicate higher scalar values. We analyse the statistics of the bubble-induced velocity and scalar fluctuations by computing their spectra and Probability Density Functions (PDFs). The spectra of the velocity  $E_u(k)$  and scalar variance  $E_c(k)$  for the suspension (gas and liquid phases) are defined as

$$E_u = \frac{1}{2} \langle \mathbf{u}^2 \rangle = \int_0^\infty E_u(k) dk \quad (4.7)$$

$$E_c = \frac{1}{2} \langle c'^2 \rangle = \int_0^\infty E_c(k) dk \quad (4.8)$$

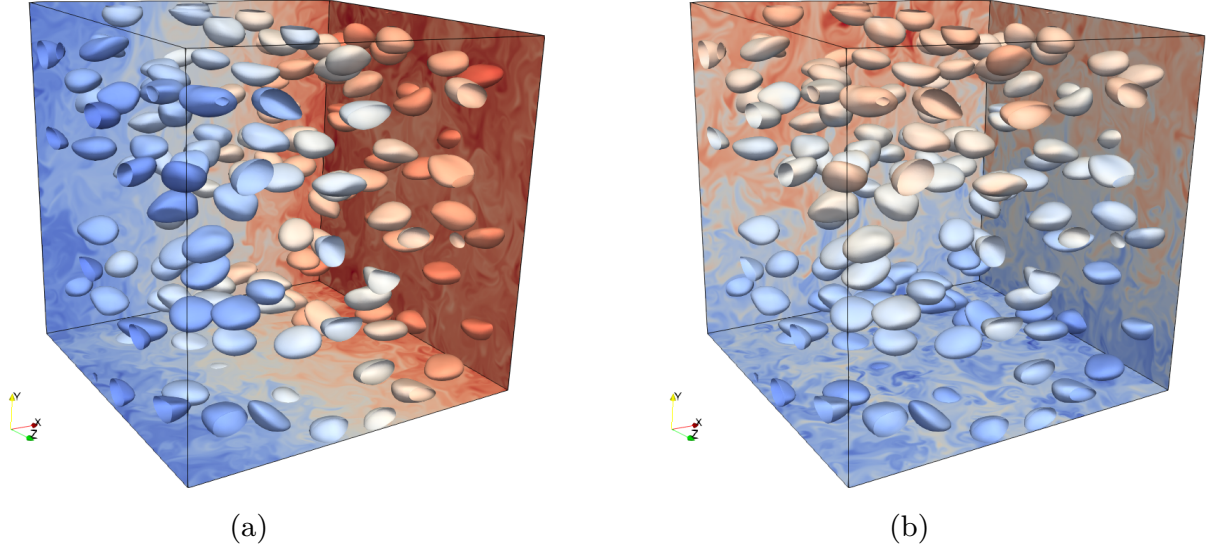


Figure 4.12: Snapshots from our DNS with  $\phi = 5.2\%$ ,  $Sc_l = 7$  and an imposed mean scalar gradient (a) in the horizontal direction  $\nabla\langle c\rangle^h = 1$  and (b) in the vertical direction  $\nabla\langle c\rangle^v = 1$ . The colours represent the total scalar fields  $c$ , where warmer colours indicate higher values.

where  $k = |\mathbf{k}|$  is the wavenumber. To compute these spectra in the liquid phase, we use the same definitions but regularise the fields according to  $\mathbf{u}_l = \mathbf{u}f$  and  $c'_l = c'f$  where  $f$  is the volume fraction field that is 1 in the liquid phase and 0 in the gas phase.

Figure 4.13 shows the normalised velocity spectra of the liquid phase and the suspension for our cases that are in excellent agreement with previous DNS by Pandey et al. [43] for a suspension at similar governing parameters (case R7 in that study with  $\phi = 1.7\%$ ). The latter study used a front-tracking technique that does not require the repulsive force model described in Section 3.3.1. The agreement of the velocity spectra thus both confirm that we capture the correct dynamics and that the implemented repulsive force model does not influence the statistical properties of the bubbly flow.

We observe a peak of the velocity spectra at length scales comparable to the bubble diameter  $d_b$  ( $k/k_{d_b} \approx 1$  with  $k_{d_b} = 2\pi/d_b$ ), which is a reasonable result since in this system it is the bubble motion that generates the velocity fluctuations. However, at  $k/k_{d_b} > 1$ , the velocity spectra scale approximately as  $k^{-3}$  that is characteristic of bubble-induced turbulence and in agreement with previous studies [38–44].

The scalar spectra for the case  $\phi = 5.2\%$  at different  $Sc_l$ -numbers are shown in Figure 4.13b. The spectra for  $\phi = 1.7\%$  are similar and not shown here for brevity. We find that the scalar spectra transition from the  $k^{-5/3}$  scaling observed in single-phase isotropic turbulence to the same  $k^{-3}$  scaling observed in the bubble-induced turbulence velocity spectrum. The transition occurs at length scales comparable to or below the bubble diameter ( $k \geq k_{d_b}$ ), and the transition length scale decreases with the liquid scalar diffusivity (increasing  $Sc_l$ ). This transition clearly shows that the scalar dynamics are influenced by the bubble-induced turbulence also at the scales below the bubble

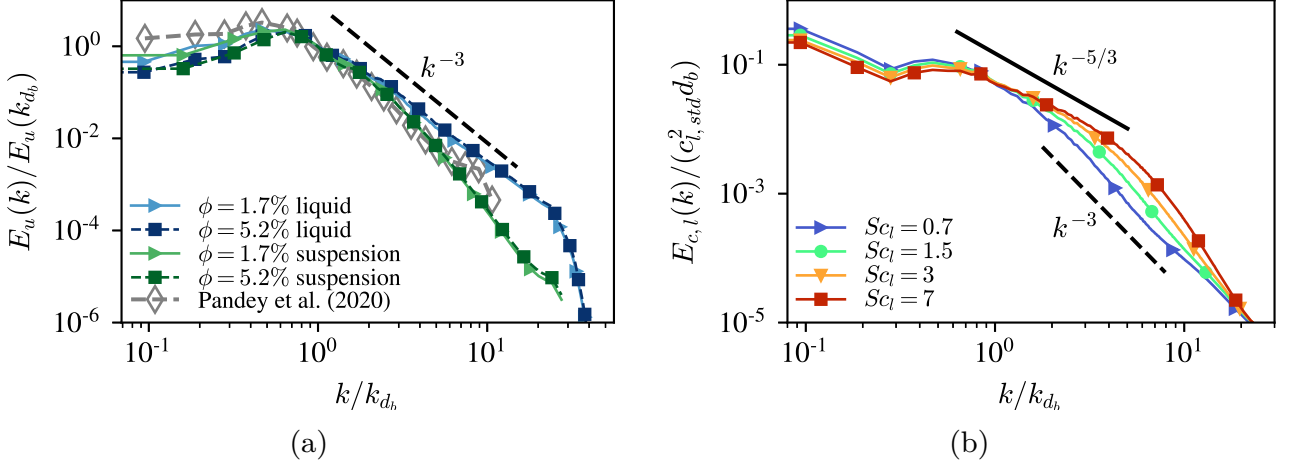


Figure 4.13: (a) velocity spectra from our DNS computed in the liquid phase and the suspension (both phases). We note a transition to a  $k^{-3}$  scaling at the scales comparable to the bubble diameter that is in good agreement with previous DNS studies [43]. (b) scalar fluctuation spectra in the case of  $\phi = 5.2\%$  and  $Sc_g = 0.7$  at various  $Sc_l$ -values. Also here we observe a transition to an approximately  $k^{-3}$  scaling at the scales comparable to or below the bubble diameter.

diameter. In Paper E, we compute the scalar spectra budget and find that, at the scales where  $k/k_{db} > 1$ , the scalar transfer term scales as  $k^{-1}$  and balances with the diffusive dissipation term to induce the  $k^{-3}$  scaling of the scalar spectra. This is in line with the hypothesis proposed in the experimental work of Dung et al. [48] about the mechanisms behind the  $k^{-3}$  scaling. This is, however, in contrast with the velocity fluctuations that are continuously produced and directly dissipated in the bubble wakes at scales  $k > k_{db}$  [38].

We find further differences between the velocity and scalar fluctuations by comparing their normalised PDFs. The liquid horizontal and vertical velocity fluctuation PDFs are shown in Figure 4.14, where the velocities are normalised by the standard deviation in the corresponding case. Here, we note that our cases are in good agreement with experimental (Riboux et al. [40]) and numerical (Pandey et al. [43]) studies at similar governing parameters. The vertical PDFs are clearly asymmetric with large upward (positive) fluctuations more probable than large downward fluctuations because of the preferential upward motion of the bubbles. The horizontal velocity PDFs are also non-Gaussian with a high exponential decay at small fluctuations but a slower decay at more pronounced fluctuations. The horizontal velocity PDFs are symmetric because the average bubble-induced liquid agitation is axisymmetric and the horizontal bubble distribution is statistically homogeneous.

Contrary to the velocity, we find that the scalar fluctuation PDFs are approximately Gaussian for all our cases. Figure 4.15a and Figure 4.15b show the liquid scalar fluctuation PDFs for the cases with an imposed mean gradient in the horizontal  $c_l^h$  and vertical  $c_l^v$  directions. The scalar fluctuations are normalised by their standard deviation in the corresponding case and become self-similar. All the cases have  $Sc_g = 0.7$  except for the cases shown with grey colour where we assess the influence on the scalar dynamics of

increasing  $Sc_g$  to 7. The black dash-dotted line represents a Gaussian distribution that describes well the scalar PDFs. The corresponding PDFs for the bubble suspension (both phases) are shown in Figure 4.15c and Figure 4.15d and display the same behaviour as for the liquid except in the cases with  $Sc_g = 7$  and the imposed mean gradient in the vertical direction (shown in grey in Figure 4.15d). In the latter cases, large negative fluctuations are more probable than the Gaussian distribution. Such an influence of the  $Sc_g$  on the suspension statistics is observed also in Paper E for the effective scalar diffusivity and can be explained by the same following mechanism.

When a bubble moves in the direction of the imposed scalar gradient, the scalar disturbance in the bubble change proportional to the last term on the r.h.s of Equation 4.6. The time it takes for the scalar in the bubble to reach an equilibrium with the surrounding liquid is proportional to the characteristic equalisation time  $t_e = R^2/D_{mol,g}$  where  $R$  is the bubble radius. A higher  $Sc_g$ -number thus implies a longer  $t_e$  and, therefore, a higher average absolute value of  $c'$  in the gas phase. For a  $\nabla\langle c \rangle^v = 1$ , the gas phase average velocity is aligned with the mean scalar gradient, and Equation 4.6 then predicts on average negative fluctuations in the gas phase. These negative scalar fluctuations cause the observed deviation from a Gaussian distribution in the suspension (gas and liquid phases). Because of the influence of  $D_{mol,g}$ , these deviations are more pronounced at higher  $Sc_g$ -numbers.

This study shows how the passive scalar dynamics are influenced by the bubble-induced turbulence and assesses the influence of several governing parameters on the scalar statistics. The findings increase our understanding of the scalar transport in bubbly flows and can contribute to the development of improved models to predict the scalar dynamics at large-scale industrial systems. Further studies are, however, needed to investigate the influence of other governing parameters, such as the  $Ga$ ,  $Eu$ ,  $\phi$  and  $Sc$ , on the results. It would also be interesting to study how other scalar injection mechanisms, such as chemical reactions or dissolution processes at the bubble interface, would modify the findings. The present numerical framework could also be used to investigate other relevant processes, such as the bubble-induced turbulence, other types of mass transfer setups or be extended to study heat transport and reacting flows.

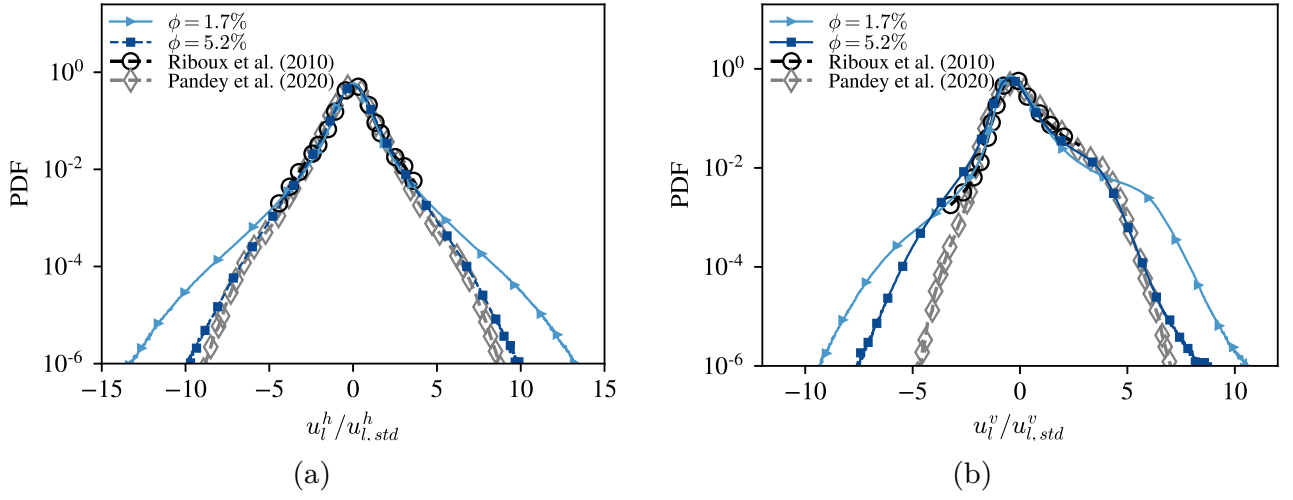


Figure 4.14: The probability density functions of (a) the horizontal velocity fluctuations and (b) the vertical velocity fluctuations in our bubbly flow DNS are in good agreement with previous experimental [40] and numerical [43] studies.

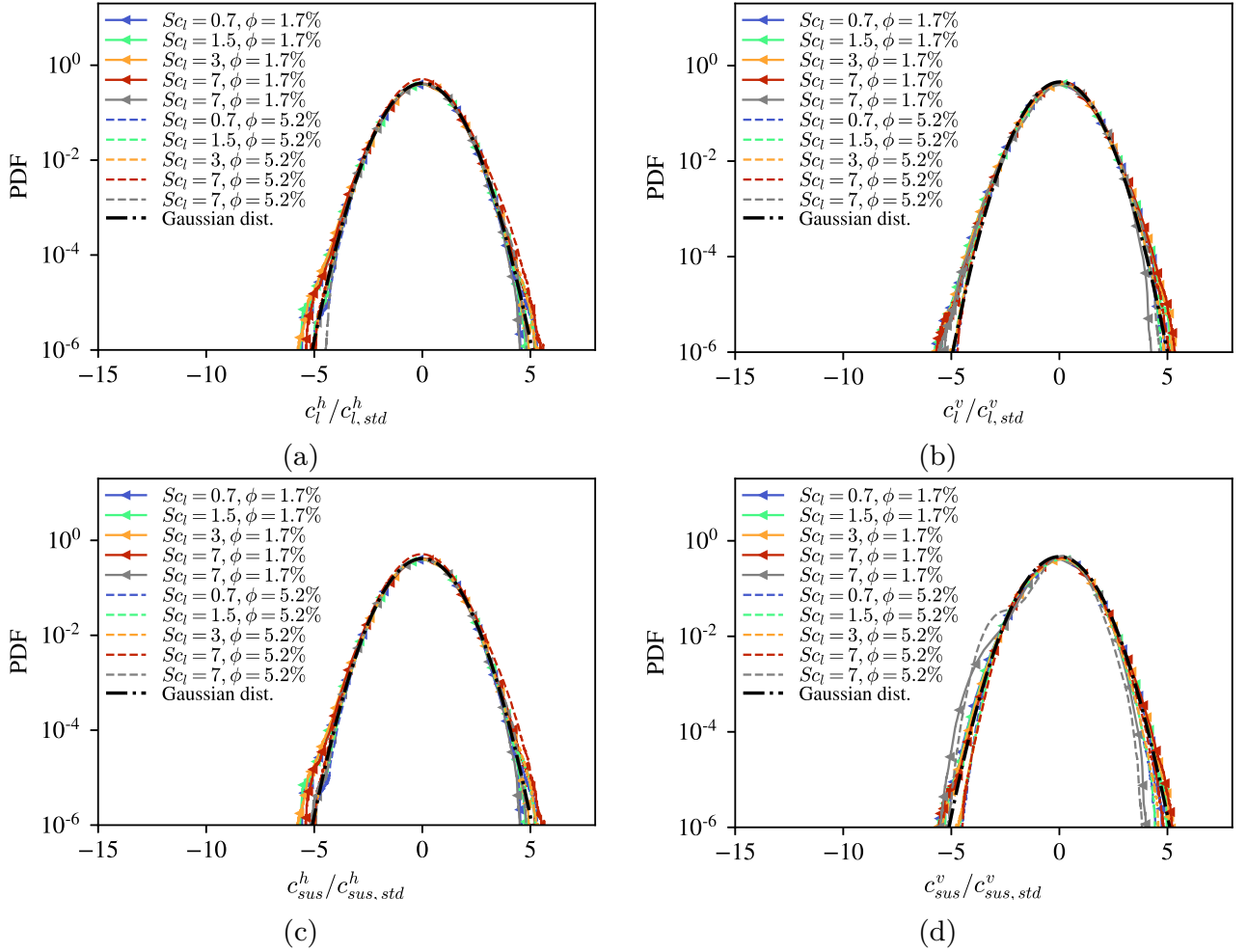


Figure 4.15: The probability density functions of the scalar fluctuations in the liquid phase (panels (a) and (b)) and in the suspension (panels (c) and (d)) with a mean scalar gradient in the horizontal direction (a,c) and vertical direction (b,d) from our bubbly flow DNS.

# 5 Conclusions and recommendations for future work

The aim of this PhD project was to increase our understanding of bubbly flows and to facilitate improved numerical predictions over a wide range of spatiotemporal scales. The work was split into three parts related to the characteristic length scales of the specific problems. Summaries of these parts are presented below in relation to their research objectives. Here, we discuss contributions to the research field, limitations and propose recommendations for future work.

## 5.1 Evolution of small-scale vapour bubbles

This part of the work aimed at first developing a numerical framework for resolving all relevant phenomena in laser-induced thermocavitation events. These events exemplify the challenges and complexities encountered in both boiling and cavitation processes. The second aim was to determine the detailed flow conditions in the vicinity of specific laser-induced thermocavitation events and examine the influence of relevant governing parameters on those conditions.

We developed a multiphase Direct Numerical Simulation (DNS) framework in Paper A and further improved it in Paper B. This framework takes into account a comprehensive list of relevant phenomena in both cavitation and boiling vapour bubble evolution processes. In Paper B, we simulate the fast and complex dynamics of a laser-induced thermocavitation bubble with growth rates governed by a rapid phase change and thermal effects at the bubble interface. The predicted growth rates are in fair agreement with experimental results and show that the framework captures the relevant phenomena of the vapour bubble evolution process. The results showed that the rapid solvent evaporation during the early bubble growth phase produces a peak of solution supersaturation at the bubble interface that is not possible to obtain using conventional crystallisation techniques under normal conditions. Since crystals have a higher probability of nucleating at increased supersaturation levels, our results indicate that the predicted peak due to rapid solvent evaporation may be the mechanism behind the observed crystallisation.

We also developed a 1D numerical framework in Paper B with an almost negligible computational cost compared to the DNS. This framework allowed us to perform an extensive parameter investigation where we examined the effects of the laser pulse energy, the spatial distribution of that energy, the solute diffusivity and the solute solubility on the maximum supersaturation level that is obtained during the bubble evolution process. The results showed that high supersaturation peaks are only obtained under specific ranges of the studied parameters. From our results, guidelines were provided to identify

suitable sets of parameters that produce conditions favourable for crystallisation.

Further validation of the numerical frameworks should be performed to assess their accuracy under a wide range of relevant conditions. Additional phenomena such as plasma formation and liquid shock wave emissions are not considered but are significant at high laser pulse energies. The inclusion of these phenomena would expand the applicability of the frameworks to cases with optical breakdown. It would also be interesting to model the phase change with the energy jump condition (similar to [56, 57]) and examine possible differences on the results compared with the present Schrage model. The crystal nucleation process occurs at molecular scales and is not considered in the current numerical framework. To better understand the conditions that are favourable for nucleation, it would be interesting to use the numerical frameworks (to study the detailed fluid conditions) in combination with experiments (that show what governing parameters that induce crystallisation). Such combined studies could help determine more accurately the parameters that are favourable for crystallisation and to develop predictive models.

## 5.2 Small-scale rising bubble dynamics

Here, we shifted our focus to the small-scale rising bubble dynamics. We aimed first at developing a numerical framework without a need for a priori knowledge about the spatiotemporal scales over which the bubble dynamics may develop. Secondly, we wanted to develop a general methodology for studying the small-scale rising bubble dynamics in response to a realistic turbulent flow with length scales larger than the bubble size.

For these purposes, we developed in Paper C a multiscale methodology for studying the small-scale bubble dynamics in laminar and turbulent flows. The multiscale methodology predicts the motion of a sub-Kolmogorov bubble in fully resolved turbulence using an Eulerian-Lagrangian solver. The turbulent fluctuations experienced by the bubble are imposed on a multiphase DNS solver with a Moving Reference Frame (MRF) technique that follows the rising bubble. The DNS solver thus resolves the detailed small-scale bubble dynamics in response to the realistic turbulent fluctuations. The motion of the MRF is determined using a PID-control approach that inherently handles both single and multiple bubble systems. With the MRF approach, the size of the computational domain and the cost of performing DNS can be significantly reduced, and the setup of the DNS simulations is simplified by eliminating the need for a priori estimations of sufficient domain sizes to capture the bubble dynamic process.

The presented results from the multiscale methodology represent a relatively limited number of relevant small-scale bubble phenomena, and many other phenomena such as bubble breakup, dispersion and interfacial forces discussed in Section 2.3 and Section 2.4 could be investigated as well. The general formulation of the multiscale methodology allows for a relatively straightforward implementation of any DNS technique for multiphase flows such as the VOF, level-set, lattice-Boltzmann or diffuse interface approaches. The

methodology can hence be used to study many small-scale processes for bubbles, drops or solid particles. Such studies can elucidate the effects of turbulent or laminar flows on the small-scale dynamics and facilitate the development of improved small-scale models.

The coupling between the two fluid dynamics solvers could be further improved by directly using the bubble trajectory predicted by the DNS solver in the EL-solver. This would allow for a full two-way multiscale coupling between the bubble and the turbulent flow. The multiscale methodology is currently limited to approximately linear velocity fields at the scale of the bubble (Kolmogorov scales comparable to or larger than the bubble size). To study the bubble dynamics in turbulent flows with scales smaller than the bubble size, the EL-solver is not appropriate, and the turbulent flow could instead be imposed on the DNS framework using a technique such as described in Feng and Bolotnov [86].

### 5.2.1 Shear-induced lift force acting on individual bubbles

In this part, we studied the lift force acting on deformable and freely moving bubbles rising in a linear shear flow. We aimed at providing a general description of the four mechanisms behind the lift force and qualitatively explaining how the different mechanisms cause the complex lift force behaviour in the relevant phase-space of the governing parameters. We also wanted to elucidate the role of the shear rate on the lift force induced by the different mechanisms.

In Paper D, we provide a theoretical framework that relates the lift force acting on the bubble to moments of the bubble-induced vorticity. Theoretical considerations are supported by the DNS framework with the MRF developed in Paper C and provide a comprehensive explanation for all mechanisms in terms of their characteristic bubble-induced vorticity fields. The study shows qualitatively the regions of the phase-space that are dominated by the different mechanisms and provides a qualitative explanation for the complex lift force behaviour within the phase-space. The numerical results show that the shear rate significantly influences the lift force coefficient in highly viscous flows or at significant bubble deformations and should thus be accounted for when formulating closures for the lift force. Our findings improve our understanding of the physical mechanisms behind the lift force and extend our knowledge about how the lift force scales with the shear rate under relevant conditions.

The results are limited to single clean bubbles rising in unbounded linear shear flows. The influence of other non-ideal conditions, such as surfactants, walls, phase change, turbulence and interaction with other bubbles, is not considered. These conditions are all practically relevant and should be investigated further. In particular, the effects of surfactants could be investigated numerically by extending the numerical framework to consider a varying surfactant concentration at the bubble interface by, for example, the method proposed in Muradoglu and Tryggvason [87]. As future research, it would also be interesting to explore the transition between the regions of the phase-space governed by the different mechanisms. By more precisely determining this transition border, it would

be possible to identify the dominating lift force mechanism in the entire phase-space.

### 5.3 Large-scale scalar dynamics in bubbly flows

Lastly, we explored the passive scalar dynamics in bubble-induced turbulence across large scales. The main aims were to first develop a numerical framework for studying passive scalar dynamics in monodisperse turbulent bubbly flows. Then, we aimed at determining how the bubble-induced turbulence and relevant governing parameters influence the passive scalar dynamics. We developed a multiphase DNS framework with a repulsive force model (Paper E and Section 3.3) to prevent bubble coalescence and preserve the monodisperse bubble size distribution over long simulation times. Using the DNS framework, we resolve all relevant scales and can extract statistically steady quantities of the velocity and scalar fields.

The results show that the bubble-induced turbulence induces a transition of the scalar spectra from the  $k^{-5/3}$  scaling (observed in single phase isotropic turbulence) to the  $k^{-3}$  scaling, with the wavenumber  $k$ , characteristic for the velocity spectrum of bubble-induced turbulence. The transition length scale is comparable to or smaller than the bubble diameter and decreases with the molecular diffusivity of the scalar in the liquid. By using the DNS method, we resolve the scalar fluctuations at all scales down to the diffusive dissipation scales. This allows us to analyse the scalar transfer term in the scalar budget equation and show that this term scales as approximately  $k^{-1}$  at the scales below the bubble diameter and induces the  $k^{-3}$  scaling of the scalar spectra.

We show in Section 4.3 that while the Probability Density Functions (PDFs) of the velocity fluctuations are non-Gaussian, the scalar fluctuation PDFs are Gaussian (except for the bubble suspension in cases with an imposed mean scalar gradient in the vertical direction and low diffusivity of the scalar in the gas). In the latter cases, we found that the gas scalar diffusivity significantly influence the gas scalar fluctuations. This effect also influences the convective scalar diffusivity, and in Paper E, we propose approximate scalings for this quantity based on a priori known governing parameters. These scalings can guide the development of improved closures for the convective scalar diffusivity and indicate that the scalar molecular diffusivity should be considered in such closures.

Our findings extend our knowledge about the passive scalar dynamics in turbulent bubbly flows and elucidate the influence of the scalar molecular diffusivity, gas volume fraction and mean scalar gradient direction on the scalar dynamics and statistics. The study motivates further studies of the influence of other governing parameters such as  $Ga$ ,  $Eo$ , gas volume fraction, and molecular diffusivities on the scalar dynamics. The results are relevant in the presence of a mean scalar gradient but are probably modified in systems where the scalar in the liquid is injected/consumed at the bubble surfaces due to, for example, chemical reaction or dissolution processes at the gas-liquid interface. Future investigations are needed to assess how the scalar dynamics are modified in such systems.

## 6 Summaries of appended papers and division of work

In Papers A and B we study the evolution of micrometer-sized vapour bubbles, where we identified a need for a better understanding of the flow conditions in and around the bubble. We develop a multiphase DNS framework with phase change modelling presented in Paper A and a corresponding 1D numerical framework in Paper B, that both predict the relevant flow conditions. In these papers, we investigate the fast and complex dynamics of laser-induced thermocavitation events that are currently studied as a promising tool for controlling the process of crystallisation.

We then shift the focus to the dynamics of individual rising bubbles in Papers C and D. Such bubble dynamics may develop over a large range of spatiotemporal scales. To facilitate efficient simulations, we have developed a multiphase DNS framework with a Moving Reference Frame (MRF) technique that follows the motion of a bubble. We couple the DNS framework with an Eulerian-Lagrangian solver to provide an efficient multiscale methodology for studying small-scale bubble dynamics in laminar or turbulent flows. These frameworks are developed in Paper C.

In Paper D, we study the mechanisms behind the lift force acting on deformable bubbles in linear shear flows. We provide a qualitative explanation for different lift-force mechanisms using a theoretical framework that relates the bubble-induced vorticity moments to the lift force. Theoretical considerations are supported with the DNS framework with the MRF developed in Paper C. This framework is also used to investigate the role of the shear rate on the lift force.

Finally, in Paper E, we investigate the large-scale dynamics and statistics of passive scalars in bubbly flows using multiphase DNS. We examine how the bubble-induced turbulence modifies the scalar spectra and study the scalar spectra energy budget to elucidate the mechanisms behind the observed scalar spectra behaviour. We also assess the influence of the governing parameters on the scalar spectra and look into the effective scalar diffusivity of the bubble suspension.

All papers were written by N. Hidman with valuable support, input and contributions by all co-authors. S. Sasic contributed considerably in the preparation of the manuscripts to Papers A and B, and G. Sardina contributed greatly in the preparation of the manuscripts to Papers C and E. All implementations into the flow solvers, the simulations and analysis were performed by N. Hidman with support from the co-authors. The numerical frameworks of Papers A and B were formulated by N. Hidman. The moving reference frame technique in Paper C was developed by N. Hidman together with G. Sardina who also conceptualised the multiscale methodology and performed the EL-simulations. The theoretical framework in Paper D was formulated by N. Hidman. G. Sardina conceptualised the study of Paper E and developed the post-processing routines.



# References

- [1] R. F. Mudde. Gravity-driven bubbly flows. *Annu. Rev. Fluid Mech.* **37** (2005), 393–423.
- [2] V. Mathai, D. Lohse, and C. Sun. Bubbly and buoyant particle-laden turbulent flows. *Annual Review of Condensed Matter Physics* **11** (2020), 529–559.
- [3] R. O. Fox. Large-Eddy-Simulation Tools for Multiphase Flows. *Annual Review of Fluid Mechanics* **44.1** (2012), 47–76. DOI: 10.1146/annurev-fluid-120710-101118.
- [4] D. Lohse. Bubble puzzles: From fundamentals to applications. *Physical review fluids* **3.11** (2018), 110504.
- [5] L. Van Wijngaarden. On pseudo turbulence. *Theoretical and computational fluid dynamics* **10.1-4** (1998), 449–458.
- [6] J. Carlton. “Chapter 9 - Cavitation”. *Marine Propellers and Propulsion (Fourth Edition)*. Ed. by J. Carlton. Fourth Edition. Butterworth-Heinemann, 2019, pp. 217–260. ISBN: 978-0-08-100366-4.
- [7] C. E. Brennen. *Cavitation and bubble dynamics*. Cambridge University Press, 2014.
- [8] T. Young. III. An essay on the cohesion of fluids. *Philosophical transactions of the royal society of London* **95** (1805), 65–87.
- [9] P. S. Marquis de Laplace. Supplément au dixième livre du Traité de Mécanique Céleste. *Traité Mécanique Céleste* **4** (1805), 1–79.
- [10] L. Rayleigh. VIII. On the pressure developed in a liquid during the collapse of a spherical cavity. *The London, Edinburgh, and Dublin Philosophical Magazine and Journal of Science* **34.200** (1917), 94–98.
- [11] M. S. Plesset and S. A. Zwick. The growth of vapor bubbles in superheated liquids. *Journal of applied physics* **25.4** (1954), 493–500.
- [12] A. Prosperetti. A generalization of the RayleighPlesset equation of bubble dynamics. *Phys. Fluids* **25.3** (1982), 409–410. DOI: 10.1063/1.863775.
- [13] M. P. Brenner, S. Hilgenfeldt, and D. Lohse. Single-bubble sonoluminescence. *Reviews of modern physics* **74.2** (2002), 425.
- [14] L. E. Scriven. On the dynamics of phase growth. *Chemical Engineering Science* **10** (1959), 1–13.
- [15] B. Mikic, W. Rohsenow, and P. Griffith. On bubble growth rates. *International Journal of Heat and Mass Transfer* **13.4** (1970), 657–666.
- [16] M. Dalle Donne and M. Ferranti. The growth of vapor bubbles in superheated sodium. *International Journal of Heat and Mass Transfer* **18.4** (1975), 477–493.
- [17] A. Prosperetti and M. S. Plesset. Vapour-bubble growth in a superheated liquid. *Journal of Fluid Mechanics* **85.2** (1978), 349–368.
- [18] H. S. Lee. “Vapor bubble dynamics in microgravity”. PhD thesis. University of Michigan, 1993.
- [19] J. C. Cano-Lozano, C. Martinez-Bazan, J. Magnaudet, and J. Tchoufag. Paths and wakes of deformable nearly spheroidal rising bubbles close to the transition to path instability. *Physical Review Fluids* **1.5** (2016), 053604.

- [20] M. K. Tripathi, K. C. Sahu, and R. Govindarajan. Dynamics of an initially spherical bubble rising in quiescent liquid. *Nature communications* **6** (2015), 6268.
- [21] J. Magnaudet and G. Mougin. Wake instability of a fixed spheroidal bubble. *Journal of Fluid Mechanics* **572** (2007), 311.
- [22] J. Cano-Lozano, P. Bohorquez, and C. Martnez-Bazán. Wake instability of a fixed axisymmetric bubble of realistic shape. *International Journal of Multiphase Flow* **51** (2013), 11–21.
- [23] M. K. Tripathi, K. C. Sahu, and R. Govindarajan. Why a falling drop does not in general behave like a rising bubble. *Scientific reports* **4** (2014), 4771.
- [24] M. R. Maxey and J. J. Riley. Equation of motion for a small rigid sphere in a nonuniform flow. *The Physics of Fluids* **26.4** (1983), 883–889.
- [25] D. Legendre, C. Colin, and T. Coquard. Lift, drag and added mass of a hemispherical bubble sliding and growing on a wall in a viscous linear shear flow. *Philosophical Transactions of the Royal Society A: Mathematical, Physical and Engineering Sciences* **366.1873** (2008), 2233–2248.
- [26] J. Magnaudet and I. Eames. The Motion of High-Reynolds-Number Bubbles in Inhomogeneous Flows. *Annual Review of Fluid Mechanics* **32.1** (2000), 659–708. DOI:10.1146/annurev.fluid.32.1.659.
- [27] M. J. Pang and J. J. Wei. Analysis of drag and lift coefficient expressions of bubbly flow system for low to medium Reynolds number. *Nuclear engineering and design* **241.6** (2011), 2204–2213.
- [28] D. Lucas, E. Krepper, and H.-M. Prasser. Prediction of radial gas profiles in vertical pipe flow on the basis of bubble size distribution. *International Journal of Thermal Sciences* **40.3** (2001), 217–225.
- [29] I. M. Mazzitelli and D. Lohse. Evolution of energy in flow driven by rising bubbles. *Physical Review E* **79.6** (2009), 066317.
- [30] R. Adoua, D. Legendre, and J. Magnaudet. Reversal of the lift force on an oblate bubble in a weakly viscous linear shear flow. *Journal of Fluid Mechanics* **628** (2009), 23–41.
- [31] D. Legendre and J. Magnaudet. A note on the lift force on a spherical bubble or drop in a low-Reynolds-number shear flow. *Physics of Fluids* **9.11** (1997), 3572–3574.
- [32] T. Auton. The lift force on a spherical body in a rotational flow. *Journal of fluid Mechanics* **183** (1987), 199–218.
- [33] Y. Liao and D. Lucas. A literature review on mechanisms and models for the coalescence process of fluid particles. *Chemical Engineering Science* **65.10** (2010), 2851–2864.
- [34] A. Acrivos. THE BREAKUP OF SMALL DROPS AND BUBBLES IN SHEAR FLOWS\*. *Annals of the New York Academy of Sciences* **404.1** (1983), 1–11.
- [35] A. Loisy and A. Naso. Interaction between a large buoyant bubble and turbulence. *Phys. Rev. Fluids* **2** (1 2017), 014606.
- [36] S. Balachandar and J. K. Eaton. Turbulent dispersed multiphase flow. *Annual review of fluid mechanics* **42** (2010), 111–133.
- [37] D. Lucas, E. Krepper, and H.-M. Prasser. Use of models for lift, wall and turbulent dispersion forces acting on bubbles for poly-disperse flows. *Chemical Engineering*

- Science* **62.15** (2007), 4146–4157. ISSN: 0009-2509. DOI: <https://doi.org/10.1016/j.ces.2007.04.035>. URL: <https://www.sciencedirect.com/science/article/pii/S0009250907003661>.
- [38] M. Lance and J. Bataille. Turbulence in the liquid phase of a uniform bubbly airwater flow. *Journal of Fluid Mechanics* **222** (1991), 95–118. DOI: 10.1017/S0022112091001015.
  - [39] J. M. Mercado, D. C. Gomez, D. Van Gils, C. Sun, and D. Lohse. On bubble clustering and energy spectra in pseudo-turbulence. *Journal of fluid mechanics* **650** (2010), 287–306.
  - [40] G. Riboux, F. Risso, and D. Legendre. Experimental characterization of the agitation generated by bubbles rising at high Reynolds number. *Journal of Fluid Mechanics* **643** (2010), 509–539.
  - [41] S. Mendez-Diaz, J. Serrano-Garcia, R. Zenit, and J. Hernandez-Cordero. Power spectral distributions of pseudo-turbulent bubbly flows. *Physics of Fluids* **25.4** (2013), 043303.
  - [42] F. Risso. Agitation, mixing, and transfers induced by bubbles. *Annual Review of Fluid Mechanics* **50** (2018), 25–48.
  - [43] V. Pandey, R. Ramadugu, and P. Perlekar. Liquid velocity fluctuations and energy spectra in three-dimensional buoyancy-driven bubbly flows. *Journal of Fluid Mechanics* **884** (2020).
  - [44] A. Innocenti, A. Jaccod, S. Popinet, and S. Chibbaro. Direct numerical simulation of bubble-induced turbulence. *Journal of Fluid Mechanics* **918** (2021).
  - [45] E. Alm  ras, F. Risso, V. Roig, S. Cazin, C. Plais, and F. Augier. Mixing by bubble-induced turbulence. *Journal of Fluid Mechanics* **776** (2015), 458–474.
  - [46] B. Gvozdi, E. Alm  ras, V. Mathai, X. Zhu, D. P. van Gils, R. Verzicco, S. G. Huisman, C. Sun, and D. Lohse. Experimental investigation of heat transport in homogeneous bubbly flow. *Journal of fluid mechanics* **845** (2018), 226–244.
  - [47] A. Loisy, A. Naso, and P. D. Spelt. The effective diffusivity of ordered and freely evolving bubbly suspensions. *Journal of Fluid Mechanics* **840** (2018), 215–237.
  - [48] O.-Y. Dung, P. Waasdorp, C. Sun, D. Lohse, and S. G. Huisman. *The emergence of bubble-induced scaling in thermal spectra in turbulence*. 2022. DOI: 10.48550/ARXIV.2207.05175. URL: <https://arxiv.org/abs/2207.05175>.
  - [49] N. G. Deen, M. van Sint Annaland, and J. Kuipers. Multi-scale modeling of dispersed gas–liquid two-phase flow. *Chemical engineering science* **59.8-9** (2004), 1853–1861.
  - [50] C. W. Hirt and B. D. Nichols. Volume of fluid (VOF) method for the dynamics of free boundaries. *Journal of Computational Physics* **39** (1981), 201–225.
  - [51] R. Scardovelli and S. Zaleski. Direct numerical simulation of free-surface and interfacial flow. *Annual review of fluid mechanics* **31.1** (1999), 567–603.
  - [52] J. U. Brackbill et al. A continuum method for modelling surface tension. *Journal of Computational Physics* **100** (1992), 335–354.
  - [53] S. Hardt and F. Wondra. Evaporation model for interfacial flows based on a continuum-field representation of the source terms. *Journal of Computational Physics* **227** (2008), 5871–5895.

- [54] F. Denner and B. G. van Wachem. Numerical time-step restrictions as a result of capillary waves. *J. Comput. Phys.* **285** (2015), 24–40.
- [55] C. R. Kharangate and I. Mudawar. Review of computational studies on boiling and condensation. *International Journal of Heat and Mass Transfer* **108** (2017), 1164–1196.
- [56] C. Kunkelmann. *Numerical modeling and investigation of boiling phenomena*. Universitäts- und Landesbibliothek Darmstadt tprints, 2011.
- [57] L. Malan, A. Malan, S. Zaleski, and P. Rousseau. A geometric VOF method for interface resolved phase change and conservative thermal energy advection. *Journal of Computational Physics* **426** (2021), 109920. ISSN: 0021-9991.
- [58] R. W. Schrage. *A Theoretical Study of Interphase Mass Transfer*. New York: Columbia University Press, 1953. ISBN: 978-0-231-87736-7. URL: <https://www.degruyter.com/view/title/548363>.
- [59] I. Akhatov, N. Vakhitova, A. Topolnikov, K. Zakirov, B. Wolfrum, T. Kurz, O. Lindau, R. Mettin, and W. Lauterborn. Dynamics of laser-induced cavitation bubbles. *Exp. Therm Fluid Sci.* **26.6** (2002), 731–737. ISSN: 0894-1777. DOI: [https://doi.org/10.1016/S0894-1777\(02\)00182-6](https://doi.org/10.1016/S0894-1777(02)00182-6). URL: <http://www.sciencedirect.com/science/article/pii/S0894177702001826>.
- [60] I. Tanasawa. Advances in condensation heat transfer. *J.P. Hartnett, T.F. Irvine (Eds.), Advances in Heat Transfer, Academic Press, San Diego, 1991.* (1991).
- [61] S. Popinet. A quadtree-adaptive multigrid solver for the Serre-Green-Naghdi equations. *Journal of Computational Physics* **302** (2015), 336–358.
- [62] E. Alm  ras, S. Cazin, V. Roig, F. Risso, F. Augier, and C. Plais. Time-resolved measurement of concentration fluctuations in a confined bubbly flow by LIF. *International Journal of Multiphase Flow* **83** (2016), 153–161.
- [63] E. Alm  ras, V. Mathai, C. Sun, and D. Lohse. Mixing induced by a bubble swarm rising through incident turbulence. *International journal of multiphase flow* **114** (2019), 316–322.
- [64] O. Dung. “Scalars in bubbly turbulence”. English. PhD thesis. Netherlands: University of Twente, Apr. 2021. ISBN: 978-90-365-5146-5. DOI: 10.3990/1.9789036551465.
- [65] A. Loisy. “Direct numerical simulation of bubbly flows: coupling with scalar transport and turbulence”. Theses. Universit   de Lyon, Sept. 2016. URL: <https://tel.archives-ouvertes.fr/tel-01418076>.
- [66] S. Popinet. An accurate adaptive solver for surface-tension-driven interfacial flows. *Journal of Computational Physics* **228.16** (2009), 5838–5866. ISSN: 0021-9991. DOI: <https://doi.org/10.1016/j.jcp.2009.04.042>.
- [67] A. J. Ladd. Sedimentation of homogeneous suspensions of non-Brownian spheres. *Physics of Fluids* **9.3** (1997), 491–499.
- [68] B. Bunner and G. Tryggvason. Dynamics of homogeneous bubbly flows Part 1. Rise velocity and microstructure of the bubbles. *Journal of Fluid Mechanics* **466** (2002), 17–52.
- [69] M. L. Talley, M. D. Zimmer, and I. A. Bolotnov. Coalescence prevention algorithm for level set method. *Journal of Fluids Engineering* **139.8** (2017).

- [70] L. Bai and D. Breen. Calculating Center of Mass in an Unbounded 2D Environment. *Journal of Graphics Tools* **13.4** (2008), 53–60. DOI: 10.1080/2151237X.2008.10129266.
- [71] T. Sugiyama and H. Masuhara. Laser-Induced Crystallization and Crystal Growth. *Chemistry—An Asian Journal* **6.11** (2011), 2878–2889.
- [72] H. Y. Yoshikawa, Y. Hosokawa, and H. Masuhara. Explosive Crystallization of Urea Triggered by Focused Femtosecond Laser Irradiation. *Jpn. J. Appl. Phys.* **45.1** (2005), L23–L26. DOI: 10.1143/jjap.45.123.
- [73] H. Y. Yoshikawa, R. Murai, S. Maki, T. Kitatani, S. Sugiyama, G. Sazaki, H. Adachi, T. Inoue, H. Matsumura, K. Takano, S. Murakami, T. Sasaki, and Y. Mori. Laser energy dependence on femtosecond laser-induced nucleation of protein. *Appl. Phys. A* **93.4** (2008), 911–915. ISSN: 1432-0630. DOI: <https://doi.org/10.1007/s00339-008-4790-x>.
- [74] H. Y. Yoshikawa, R. Murai, S. Sugiyama, G. Sazaki, T. Kitatani, Y. Takahashi, H. Adachi, H. Matsumura, S. Murakami, T. Inoue, et al. Femtosecond laser-induced nucleation of protein in agarose gel. *Journal of crystal growth* **311.3** (2009), 956–959.
- [75] A. Soare, R. Dijkink, M. R. Pascual, C. Sun, P. W. Cains, D. Lohse, A. I. Stankiewicz, and J. Kramer. Crystal Nucleation by Laser-Induced Cavitation. *Cryst. Growth Des.* **11 (6)** (2011), 2311–2316.
- [76] A. Soare. “Technologies for Optimisation and Control of Nucleation and Growth for New Generations of Industrial Crystallizers”. PhD thesis. Delft University of Technology, 2014.
- [77] M. Lighthill. Drift. *Journal of Fluid Mechanics* **1.1** (1956), 31–53.
- [78] P. Saffman. The lift force on a small sphere in a slow shear flow. *J. Fluid Mech* **22** (1965), 385–400.
- [79] E. A. Ervin and G. Tryggvason. The Rise of Bubbles in a Vertical Shear Flow. *Journal of Fluids Engineering* **119.2** (June 1997), 443–449. ISSN: 0098-2202. DOI: 10.1115/1.2819153.
- [80] I. un. The transverse migration of bubbles influenced by walls in vertical bubbly flow. *International Journal of Multiphase Flow* **6.6** (1980), 583–588. ISSN: 0301-9322. DOI: [https://doi.org/10.1016/0301-9322\(80\)90053-1](https://doi.org/10.1016/0301-9322(80)90053-1). URL: <https://www.sciencedirect.com/science/article/pii/0301932280900531>.
- [81] S. Aoyama, K. Hayashi, S. Hosokawa, D. Lucas, and A. Tomiyama. Lift force acting on single bubbles in linear shear flows. *International Journal of Multiphase Flow* **96** (2017), 113–122.
- [82] T. Ziegenhein, A. Tomiyama, and D. Lucas. A new measuring concept to determine the lift force for distorted bubbles in low Morton number system: Results for air/water. *International Journal of Multiphase Flow* **108** (2018), 11–24.
- [83] H. Hessenkemper, T. Ziegenhein, R. Rzehak, D. Lucas, and A. Tomiyama. Lift force coefficient of ellipsoidal single bubbles in water. *International Journal of Multiphase Flow* **138** (2021), 103587.
- [84] W. Dijkhuizen, M. van Sint Annaland, and J. Kuipers. Numerical and experimental investigation of the lift force on single bubbles. *Chemical Engineering Science* **65.3** (2010), 1274–1287.

- [85] J. Feng and I. A. Bolotnov. Interfacial force study on a single bubble in laminar and turbulent flows. *Nuclear Engineering and Design* **313** (2017), 345–360.
- [86] J. Feng and I. A. Bolotnov. Evaluation of bubble-induced turbulence using direct numerical simulation. *International Journal of Multiphase Flow* **93** (2017), 92–107.
- [87] M. Muradoglu and G. Tryggvason. A front-tracking method for computation of interfacial flows with soluble surfactants. *Journal of Computational Physics* **227.4** (2008), 2238–2262.
- [88] N. Hidman, G. Sardina, D. Maggiolo, H. Ström, and S. Sasic. “Numerical simulation of a laser-induced vapour bubble for crystal nucleation at low supersaturation levels”. *Proceedings of the 10th International Conference on Multiphase Flow*, (ICMF19). Rio de Janeiro, Brazil, 2019.
- [89] N. Hidman, H. Ström, S. Sasic, and G. Sardina. “Resolving sub-kolmogorov bubble dynamics in turbulent flows: Formulation of a multiscale numerical framework”. *Proceedings of the 18th International Conference on Fluid Flow Technologies. Conference on Modelling Fluid Flow (CMFF22)*. Budapest, Hungary, 2022, pp. 318–325.
- [90] N. Hidman, H. Ström, S. Sasic, and G. Sardina. “The shear-induced lift force on freely moving and deformable bubbles”. *Proceedings of the 11th International Conference on Multiphase Flow*, (ICMF23). Kobe, Japan, 2023.
- [91] N. Hidman, H. Ström, S. Sasic, and G. Sardina. “The passive scalar spectrum of bubble-induced turbulence”. *Proceedings of the 11th International Conference on Multiphase Flow*, (ICMF23). Kobe, Japan, 2023.
- [92] N. Hidman, G. Sardina, D. Maggiolo, H. Ström, and S. Sasic. Laser-induced vapour bubble as a means for crystal nucleation in supersaturated solutions - Formulation of a numerical framework. *Experimental and Computational Multiphase Flow* **1.4** (2019), 242–254. DOI: 10.1007/s42757-019-0024-z.
- [93] N. Hidman, G. Sardina, D. Maggiolo, H. Ström, and S. Sasic. Numerical Frameworks for Laser-Induced Cavitation: Is Interface Supersaturation a Plausible Primary Nucleation Mechanism? *Crystal Growth & Design* **20.11** (2020), 7276–7290. DOI: 10.1021/acs.cgd.0c00942.
- [94] N. Hidman, H. Ström, S. Sasic, and G. Sardina. A multiscale methodology for small-scale bubble dynamics in turbulence. *International Journal of Multiphase Flow* **150** (2022), 103976. DOI: 10.1016/j.ijmultiphaseflow.2022.103976.
- [95] N. Hidman, H. Ström, S. Sasic, and G. Sardina. The lift force on deformable and freely moving bubbles in linear shear flows. *Journal of Fluid Mechanics* **952** (2022), A34. DOI: 10.1017/jfm.2022.917.
- [96] N. Hidman, H. Ström, S. Sasic, and G. Sardina. “Assessing passive scalar dynamics in bubble-induced turbulence using DNS”. Submitted to a scientific journal.